UNIVERSITY OF CALIFORNIA,
IRVINE

Nonlinear Optical Microscopy with Confined Optical Fields

DISSERTATION

submitted in partial satisfaction of the requirements
for the degree of

DOCTOR OF PHILOSOPHY

in Chemical and Biomolecular Engineering

by

Shamsul Abedin

Dissertation Committee:
Professor Eric O. Potma, Co-Chair
Professor Regina Ragan, Co-Chair
Professor Matthew D. Law

2022

DEDICATION

Dedicated to my parents, M Zainal Abedin and Sultana Shaheda Abedin, for their unconditional love and support

TABLE OF CONTENTS

LIST OF FIGURES

LIST OF TABLES

ACKNOWLEDGMENTS

I would like to express my sincerest gratitude towards my PhD advisor Professor Eric Olaf Potma for his constant support, guidance and mentorship. You have always been a source of motivation and inspiration for me. I honestly could not have hoped for a better advisor during these crucial years of my life. Thank you!

I would also like to thank my dissertation committee members Professor Regina Ragan and Professor Matthew D. Law for their support, guidance and suggestions.

I would like to thank my amazing friends and labmates at the Potma group for all your support, fun times, serious discussions and motivation that led me to grow as a better person and a better engineer. Yong Li, Dave Knez, Abid Anjum Sifat, Dr. Khokan Roy and Dr. Richard Prince - thanks for all your support and shared positive moments.

And last but not least, I would like to thank my family. Without the constant support and love from my parents - Zainal and Shaheda Abedin, and my brother - Quamrul Abedin, I could never have become the person I am today.

VITA

Shamsul Abedin

EDUCATION

Doctor of Philosophy in Chemical and Biomolecular Engineering **2022**
University of California, Irvine *Irvine, CA*

Master of Science in Chemical and Biomolecular Engineering **2019**
University of California, Irvine *Irvine, CA*

Bachelor of Science in Chemical Engineering **2017**
Bangladesh University of Engineering and Technology *Dhaka, Bangladesh*

RESEARCH EXPERIENCE

Graduate Student Researcher **2017–2022**
University of California, Irvine *Irvine, California*

TEACHING EXPERIENCE

Teaching Assistant **2021–2022**
University of California, Irvine *Irvine, California*

REFEREED JOURNAL PUBLICATIONS

Enhancement of molecular coherent Raman scattering with silicon nano-antennas **2022**
Nano Letters (Submitted)

Surface-enhanced Coherent Anti-Stokes Raman Scattering of Molecules near Metal-dielectric Nanojunctions **2022**
Journal of Physical Chemistry C

Sensing biomolecular interactions by the luminescence of a planar gold film **2019**
Analytical Chemistry

REFEREED CONFERENCE PUBLICATIONS

Particle sensing with confined optical field enhanced fluorescence emission **Feb 2020**
SPIE Photonics West 2020, San Francisco

Surface-enhanced coherent anti-Stokes Raman scattering at metal-metal and metal-dielectric nanojunctions **Jan 2022**
SPIE Photonics West 2022, San Francisco

ABSTRACT OF THE DISSERTATION

Nonlinear Optical Microscopy with Confined Optical Fields

By

Shamsul Abedin

Doctor of Philosophy in Chemical and Biomolecular Engineering

University of California, Irvine, 2022

Professor Eric O. Potma, Co-Chair and Professor Regina Ragan, Co-Chair

Nonlinear optical techniques are promising tools in changing the landscape of label-free optical imaging and sensing. Well-designed optical nanoantennas with exquisite light confinement capabilities can significantly enhance the inherently weak nonlinear light-matter interactions that can only be accessed through strong optical fields. This dissertation discusses how the third-order optical response of materials can be exploited to design and optimize chemical sensors with exceptional stability and reproducibility. Conventional nonlinear nanophotonic systems utilize localized surface plasmon resonance (LSPR) based nanoantennas to amplify light-matter interactions due to their extraordinary ability to confine incident electromagnetic fields to nanoscopic regions. These antennas, however, suffer from ohmic losses and subsequent photothermal effects adversely affect the stability and reproducibility of the signal obtained through these sensors. In this dissertation, we move away from traditional LSPR-based two-particle metallic nanojunctions and shift towards metal-free optical nanoantennas for robust chemical sensing. The first part of this dissertation investigates two-photon absorption of planar gold films to reliably sense biomolecular interactions on the level of single-nanoparticles and interrogates the mechanism of signal generation. This sensor takes advantage of more stable and controllable surface plasmon polariton (SPP)-based nanoantennas for sensing with enhanced stability. The second sensor discussed in this work probes the vibrational response of molecules through surface-enhanced coherent

anti-Stokes Raman scattering (SE-CARS). This sensor reimagines the experimental configuration through incorporation of dielectric particles on top of a precisely controllable metallic thin film to generate molecular signal from thermally stable metal-dielectric heterojunctions. Finally, a metal-free antenna system is used to report the first experimental observation of SE-CARS without the involvement of surface plasmons with unprecedented stability and reproducibility.

Chapter 1

Introduction

1.1 Enhancing nonlinear light-matter interaction through nanophotonics

Experimental investigation into nonlinear optical phenomena began in the early 1960's with the advent of the laser [9]. Over the past six decades, nonlinear optics (NLO) has grown into an exciting field affecting most modern photonic technology platforms, including (but not limited to) ultrafast optics, spectroscopy, microscopy, optical signal processing and chemical sensing [10].

Optical nonlinearities depend strongly on the amplitude of incident electromagnetic fields and can be enhanced further by orders of magnitude through nanophotonic amplification. The most common route to achieve nanophotonic enhancement of light-matter interaction utilizes surface plasmon resonances supported by metallic nanostructures. These plasmonic effects arise from the coherent oscillation of conduction electrons near the surfaces of these structures [11, 12]. Enhancement through plasmonic nanoantennas can be mediated by

propagating surface electromagnetic waves on continuous metal surfaces, known as surface plasmon polaritons (SPP) or by localised surface plasmons (LSP) on metallic nanoparticles. Coupling of incident optical fields to surface plasmons can result in strong electromagnetic fields that are confined to the metallic surfaces [12]. The exquisite sensitivity of these surface fields to the changes in the local environment serves as the basis for a number of chemical sensors [13]. The enhanced optical fields, in turn, can also enhance nonlinear optical effects near the surface. This plasmonic enhancement can boost the signal derived from the optical nonlinearity of metal itself (intrinsic response), as well as from the optical nonlinearity of a material located near the metal surface (extrinsic response)[14]. Apart from these metallic nanostructures, dielectric materials with high refractive indices are also being studied as a new class of optical antenna materials that can provide improved control and reliability in surface-enhanced nonlinear optical sensors. This dissertation investigates the application of SPP, LSPR and dielectric-based nanoantennas in stable and reproducible *nonlinear* nanophotonic spectroscopy systems for chemical and biomolecular sensing.

1.2 Nanoantennas for enhanced chemical sensing

Optical nanoantennas are nanoscale physical structures that can efficiently capture and confine incident electromagnetic radiation in order to considerably enhance light-matter interaction. By this definition, a simple plano-convex lens can be considered an antenna, albeit a poor one as its ability to localize light is limited by diffraction. To realize highly sensitive nonlinear optical sensors, more advanced antennas are needed. SPP and LSP based metallic structures are two of the most commonly studied types of optical antennas.

In SPP based sensors, surface-bound uniform electromagnetic fields probe small changes in local refractive-indices near the sensor surface [15]. These sensors provide a plethora of qualitative and quantitative information including the binding/dissociation kinetics, chemi-

cal specificity and concentration of the target molecule. A large number of targets such as nanoparticles, cellular organism, extracellular vesicles, proteins and nucleic acids have been studied using SPP based spectroscopy and microscopy systems. Apart from refractive-index sensing, other chemical signature reporters such as fluorescence and Raman scattering have also been utilized to build SPP-nanoantenna based sensing platforms [8].

While SPP-based sensors are useful and provide a treasure trove of crucial information regarding the chemical species of interest, significantly more surface-enhanced spectroscopy systems have been investigated over the last five decades that utilize localized surface plasmon resonance (LSPR) based nanoantennas to enhance light-matter interaction[8]. LSPR-based nanoantenna systems have been studied extensively for spectroscopic modalities such as surface-enhanced Raman scattering (SERS), surface-enhanced fluorescence (SEF) and surface-enhanced infrared absorption. However, no other spectroscopic technique has been explored as much as SERS in which LSPR-based optical antennas are used to amplify the chemical signal of the target molecule. This is due to the fact that the enhancement achievable through LSPR-based nanoantennas far exceed the capabilities of SPP-based ones. Field enhancement factors of $\sim$350 are regularly achieved using nanoantennas composed of metallic aggregates such as dimers, trimers, tetramers or larger clusters[11]. The enhancement for SPP, on the other hand, are rather modest - hovering around 6-8 in most cases. In a typical LSPR-based plasmonic nanoantenna, coupling between the incident optical field and the metallic substrate causes concentration of the electromagnetic field in the vicinity of the nanoantenna. These confinement intensifies the fields that interact with the target molecule, resulting in strong amplification of the signal. The extent of amplification of the field rely strongly on the morphology of the antenna. Generally, highest enhancement factors are observed at the nanoscopic junctions of multiple metallic particles or at sharp features of independent nanostructures. These sub-wavelength sized systems have been successfully implemented to acquire signal from single molecules. Advances in the field of nanofabrication has allowed experimentation with the size and shape of the nanoantenna as well as spectral

tuning of the structures to allow more efficient performance at particular wavelengths. Individual structures and arrays of nanodisks, pillars, holes, sharp tips, core-and-shell particles and metal-insulator-metal (MIM) structures have been broadly studied as SERS substrates with considerable success[16].

Although metallic nanoantennas, particularly LSPR-based ones, are the current gold standard in the field of surface-enhanced optical spectroscopy, they intrinsically suffer from large ohmic losses and the accompanying undesirable thermal effects can result in morphological changes to the nanoantennas[17, 5, 4, 8]. This inherent drawback of metal-based nanoantennas is well-known and has demanded the exploration of other class of antenna materials that are not subject to the same deleterious thermal effects that plague metallic nanoantennas. Dielectric materials with high-refractive indices in the visible and near-infrared (NIR) regime are promising candidates as nanoantenna materials because of their innate low ohmic losses, strong extinction efficiencies and strong electric and magnetic responses in this spectral range[4, 17]. The mechanism behind field localization and enhancement in dielectrics are markedly different compared to metals. High-index dielectric particles such as Si, Ge and GaP have strong magnetic response in the visible and NIR regime, in addition to electric ones that are not present in metals. This magnetic response grants an additional means of field localization[8]. As expected, the enhancement of the incident fields are relatively weak compared to what can be found in metallic nanoantennas due to the absence of surface plasmons. But these dielectric antennas are less prone to adverse thermal effects and can provide more stable and reproducible signals over longer periods of time that metals cannot match. Before choosing an antenna system, one must take a deep look into the requirements and understand the acceptable trade-offs. If lower field enhancements are acceptable and uniform confined field is the primary requirement, one can choose SPP-based antennas. When heat-induced morphological changes are tolerable and highest possible local fields are of paramount importance, LSPR-based nanoantennas are the most feasible option. However, in cases where continued and stable signal strength are expected along with moderately

strong locally enhanced fields, dielectrics are a reasonable choice. The case for LSPR-based antennas becomes particularly weak when ultrafast nonlinear optical effects are being considered. In such cases, the local fields are extraordinarily intense and LSPR-based antennas can no longer provide the stability the sensing system demands.

1.3 Towards stable and reproducible surface-enhanced coherent Raman sensing with dielectric nanoantennas

Surface enhanced Raman scattering (SERS) is an excellent tool for chemical and biomolecular analysis of molecules and allows probing of molecular vibrations at minute concentrations. However, at the single or few molecule limit, it struggles to acquire signal at rates faster than one to few tens of Hz[18, 19]. In applications where faster acquisition rates are necessary, SERS does not provide acceptable performance and additional means of signal amplification becomes essential. Nanophotonic enhancement of coherent Raman scattering can provide a solution to this problem. In coherent Raman scattering (CRS), vibrational motions of the analyte are driving in stimulated fashion and signal levels enhanced by orders of magnitude can be observed. Enhancing this coherently amplified Raman scattered signal with the use of optical nanoantennas can offer detection of molecular signals at single-molecule levels while enabling microsecond acquisition rates. The nanoantennas so far used in SE-CARS studies have relied exclusively on metallic nanojunctions[20]. Significant advances have been made in experimental configurations and single-molecule sensitivity has been reported. However, the detrimental photo-thermal heating effects discussed in the previous section becomes even more alarming as multiple ultrafast excitation fields are involved. Under such intense irradiation levels, the electron temperature can reach thousands of Kelvin and subsequent

increase in the lattice temperature causes irreversible damage to the antenna junction[6]. This, in turn, causes significant issues with the reliability and reproducibility of the SE-CARS signal.

In this dissertation, we aim to provide a novel solution to this issue of reproducibility of SE-CARS experiments. We take a systematic approach in order to overcome these innate limitations of the nanoantennas typically used in these measurements. We gently move away from two-particle metallic nanojunctions and towards all-dielectric optical antennas for improved reproducibility. Using a particle-on-a-film geometry, we probe molecules sandwiched between a planar gold film and a gold nanoparticle. Replacing one of the particles with a precisely controllable thin film adds to the reprodcibility of the experimental geometry and the reduced local fields help with the heating of the junction. Subsequently, we further improve the local heating of the nanojunction by replacing the gold nanoparticles with dielectric silicon nanoparticles. This unique geometry significantly improves the reliability, repeatability and control of the SE-CARS system. Finally, we move away from metals altogether and use all-dielectric nanoantennas based on silicon nanoparticles and present the first experimental demonstration of SE-CARS of molecules without the involvement of surface plasmons. This metal-free nanoantenna system provides a unique solution to a longstanding issue of thermal stability in traditional SE-CARS sensors.

1.4 Scope of this dissertation

In this dissertation, nanophotonic amplification of nonlinear optical response of materials are presented in order to uncover their electronic and vibrational properties. Ultrafast optical fields are confined to nanoscopic regions with the help of optical nanoantennas. The nanoantennas discussed in this dissertation provide improved thermal stability and reproducibility of the detected signal compared to traditional all-metal, localized surface plasmon resonance

based systems.

In Chapter 2, we present a summary of theoretical concepts that are relevant to the studies in this dissertation. This discussion starts with the electromagnetic response of metals in optical frequencies. Then the mechanisms of electromagnetic field confinement in the cases of SPPs and LSPRs are discussed. Commonly used chemical sensing applications using both SPP and LSPR-based nanoantennas are summarized. Then the concept of dielectric nanoantennas for chemical sensing is introduced. Electromagnetic and chemical enhancement routes of signal amplification are examined here. Finally, the basic principles of nonlinear optical processes and their nanophotonic enhancements are discussed. Particularly, third-order nonlinear processes and the intricacies of the thermal responses of different classes of nanoantennas to amplify these phenomena are discussed.

In Chapter 3, a novel wide-field nonlinear optical microscope is presented. We discuss the operating principle and performance of the surface plasmon-enhanced optical sensor that utilizes two-photon excited luminescence of a planar gold film as the reporter signal. The sensor enables direct visualization of nanoscopic binding events near a sensing surface. Light is coupled to the Au/sample interface in an objective-based Kretschmann configuration to excite surface plasmon polariton (SPP) modes at a metal–dielectric interface. The gold luminescence induced by the confined optical field between the particle and the film is detected in the epi-direction by a far-field camera where individual binding events show up as diffraction limited bright spots against a dark background. We study the sensor's emission spectrum and the distance dependence between the target and substrate, which both suggest that the optical signal of the sensor originates from electron–hole pair excitations in the planar Au film. In addition, we show that the well-behaved pointspread function of the sensor enables a straightforward implementation of super-resolution techniques. Finally, we demonstrate the utility of the sensor for detecting DNA binding events, underlining the sensor's usefulness for label-free imaging of nanoscopic particles and biomolecular interactions.

In Chapter 4, we discuss an experimental configuration consisting of {Au film}-molecule-{Au particle} or {Au film}-molecule-{Si particle} nanojunctions for performing wide-field surface-enhanced CARS (SE-CARS) measurements in a reproducible and controllable manner. While the allowable illumination dosage in the {Au film}-molecule-{Au particle} case is limited by the strong two-photon background from the gold, we successfully generate a detectable coherent Raman response from a molecular monolayer using the lowest reported average power densities to-date. With a vision to minimize the two-photon background and the intrinsic losses observed in all-metal plasmonic systems, we examine the possibility of using high-index dielectric particles on top of a thin metal film to generate strong nanoscopic hotspots. We demonstrate repeatable SE-CARS measurements at the {Au film}-molecule-{Si particle} heterojunction, underlining the usability of this experimental geometry. This work paves the way for the development of next-generation of chemical and biomolecular sensing assays that can minimize some of the major drawbacks encountered in fragile and lossy all-metal plasmonic systems.

In Chapter 5, we present the first experimental demonstration of surface-enhanced coherent anti-Stokes Raman scattering (SE-CARS) of molecules with a dielectric Si nanoantenna. We also study the thermal stability of the signal and compare that with SE-CARS signals ontained from a Au nano-dumbell antenna. This work shows that the inclusion of a dielectric nanoantenna can overcome the longstanding limitation of traditional metallic SE-CARS systems where unfavorable thermal properties adversely affect the stability and reproducibility of the measurements.

In the last chapter, the reader will find a summary of the results presented in this dissertation and their potential implications in advancing the field of nonlinear nanophotonics.

Chapter 2

Background

2.1 Interaction of metals with visible light

2.1.1 Optical response of metals

Noble metals exhibit exquisite properties in response to electromagnetic radiation in the optical regime. These properties are dictated by the free movement of conduction electrons within the material and the interband excitations under resonant oscillation[11, 15]. The transparency of noble metals depends strongly on the frequency of the impinging light. While they are mostly opaque to the low-frequency microwave and far-infrared radiations, metals become increasingly more transparent as they reach the near-infrared and visible regions of the electromagnetic spectrum. The complex dielectric function $\varepsilon(\omega)$ is a central concept in this dissertation that helps explain the dispersive nature of the metals and other accompanying phenomena. The interactions of these metals with electromagnetic radiation can be understood using a classical picture based on the Maxwell's equations. These equations connect four macroscopic fields, namely the electric field ($\mathbf{E}$), the magnetic field ($\mathbf{H}$),

the dielectric displacement ($\mathbf{D}$) and the magnetic flux density ($\mathbf{B}$)[11]. The fields are also linked by the magnetization $\mathbf{M}$ and polarization $\mathbf{P}$ via the following relations.

$$\mathbf{D} = \varepsilon_0 \mathbf{E} + \mathbf{P} \qquad\qquad \mathbf{H} = \frac{1}{\mu_0}\mathbf{B} - \mathbf{M} \tag{2.1}$$

Here, ε_0 and μ_0 are the electric permittivity and magnetic permeability of vacuum, respectively.

When a metal is subjected to external electric fields, a displacement $\mathbf{r}$ of an electron occurs. This displacement is associated with a dipole moment $\mathbf{p} = e\mathbf{r}$. For a total of $\mathbf{n}$ free electrons, the cumulative effect can be described by macroscopic polarization per unit volume, $\mathbf{P} = n\mathbf{p}$. This polarization also has a frequency dependence and can be expressed as:

$$\mathbf{P}(\omega) = \varepsilon_0 \chi_e(\omega)\mathbf{E}(\omega) \tag{2.2}$$

From Maxwell's equations, we have

$$\mathbf{D}(\omega) = \varepsilon_0 \varepsilon(\omega)\mathbf{E}(\omega) = \varepsilon_0 \mathbf{E}(\omega) + \mathbf{P}(\omega) \tag{2.3}$$

Here, $\mathbf{D}$ is dielectric displacement and χ_e is electric susceptibility.

When we combine the two equations above and solve for ε, we get an expression for the dielectric function as a function of frequency of incident radiation.

$$\varepsilon = 1 + \chi_e(\omega) \tag{2.4}$$

2.1.2 Drude-Sommerfeld model

Reliable approximation of dielectric functions is very important in order to understand the optical response of noble metals. Here, we consider a plasma model where we assume a gas of free electrons having a number density n moves against a fixed background of positive ion cores[11, 21]. The electrons oscillate in response to the applied electric field. The damping of the oscillations is considered in this model through the inclusion of the characteristic collision frequency $\Gamma = \frac{1}{\tau}$, where τ is the relaxation time of the free electron gas. This time is usually on the order of one to few tens of femtoseconds. We can write an equation of motion for free elections under an external alternating electric field. If we assume the electric field to have a harmonic time dependence, we can express the field via $\mathbf{E}(t) = \mathbf{E}_0 e^{-i\omega t}$. We do not include a term for restoring force as the electrons that are being considered can move freely and are not bound to any particular nucleus.

$$m_e \frac{\partial^2 \mathbf{r}}{\partial t^2} + m_e \Gamma \frac{\partial \mathbf{r}}{\partial t} = e\mathbf{E}_0 e^{-i\omega t} \tag{2.5}$$

. Here, m_e and e are the effective mass and charge of the free electrons, and E_0 is the amplitude of the applied field. A solution to this equation is $\mathbf{r} = \mathbf{r}_0 e^{-i\omega t}$. This yields,

$$\mathbf{r}(t) = \frac{e}{m(\omega^2 + i\Gamma\omega)} \mathbf{E}(t) \tag{2.6}$$

Using the expression above and the definitions of polarization $\mathbf{P}$ and displacement $\mathbf{D}$, we arrive at an expression for the dielectric function ε.

$$\varepsilon(\omega) = 1 - \frac{\omega_p^2}{\omega^2 + i\Gamma\omega} \tag{2.7}$$

This expression can be divided into its real and imaginary components via

$$\varepsilon(\omega) = 1 - \frac{\omega_p^2}{\omega^2 + \Gamma^2} + i\frac{\Gamma\omega_p^2}{\omega(\omega^2 + \Gamma^2)} \tag{2.8}$$

Here, ω_p is the plasma frequency of free electron gas, given by $\sqrt{\frac{ne^2}{\varepsilon_0 m}}$[21]. This plasma frequency can be considered as the natural frequency of the oscillation of the free electron gas. The quanta of the plasma oscillations are known as plasmons.

2.1.3 Lorentz correction to Drude-Sommerfeld model

The Drude-Sommerfeld model predicts the dielectric functions of metals quite accurately at low frequency. However, the model deviates considerably from actual measured values at wavelengths shorter than $\sim$ 650 nm[21, 15]. This deviation can be explained by the response of bound electrons at these frequencies. This is due to the fact that high-energy photons are able to promote electrons from d-band to sp-conduction band and these transitions can be described as excitation of the bound electron oscillation. We can use the same approach as above to describe this motion of bound electrons.

$$m\frac{\partial^2 \mathbf{r}}{\partial t^2} + m\gamma\frac{\partial \mathbf{r}}{\partial t} + \alpha\mathbf{r} = e\mathbf{E}_0 e^{-i\omega t} \tag{2.9}$$

Here m is the effective mass of the electron, γ is the damping coefficient and α is the spring constant of the restoring force. The same approach we used in the previous sections yields

$$\varepsilon(\omega) = 1 + \frac{\omega_p^2}{(\omega_0^2 - \omega^2) - i\gamma\omega} \tag{2.10}$$

This expression can also be divided into its real and imaginary components.

$$\varepsilon(\omega) = 1 + \frac{\omega_p^2(\omega_0^2 - \omega^2)}{(\omega_0^2 - \omega^2)^2 + \gamma^2\omega^2} + i\frac{\gamma\omega_p^2\omega}{(\omega_0^2 - \omega^2)^2 + \gamma^2\omega^2} \tag{2.11}$$

Here, $\omega_0 = \sqrt{\frac{\alpha}{m}}$. This expression takes the contribution from the interband transitions of bound electrons into account and provides a better approximation of the dielectric function of metals at higher frequencies. A brief analysis of the real and imaginary portions of the dielectric function shows resonant behavior for the imaginary part and dispersive behavior for the real part[21].

2.2 Surface plasmon polaritons

Surface plasmon polaritons (SPP) are surface electromagnetic waves that propagate along a metal-dielectric interface [11]. When an incoming freely propagating optical field is coupled to an SPP mode, a strong resonant oscillation of conduction electrons near the metal's surface is achieved. The electric field caused by the oscillation of surface electrons decays exponentially (∼200 nm from the interface), providing sub-wavelength confinement of the electromagnetic field along the z-direction, as seen in figure 2.1 [12, 21]. The resulting SPPs are very sensitive to minute changes in local refractive indices close to this interface.

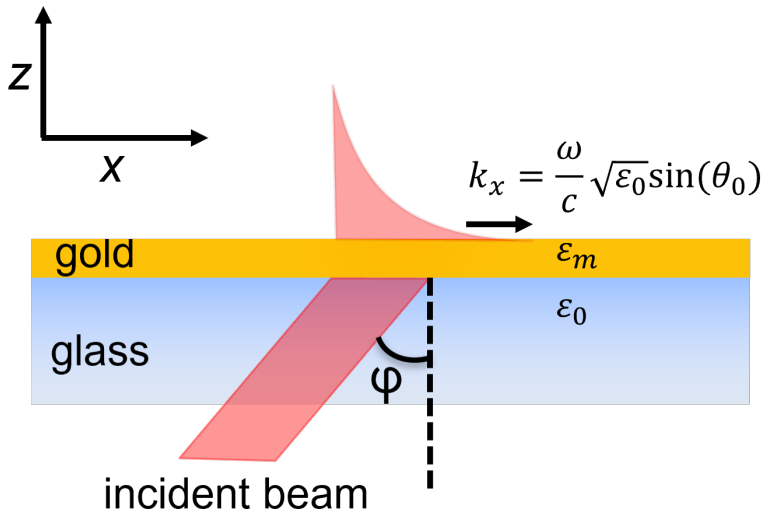

Figure 2.1: Propagating surface plasmon polariton modes at a metal-dielectric interface. Incoming optical field arrives at a phase-matched direction generating exponentially decaying evanescent electromagnetic field along the z-direction

As the SPP excitation is a coupled state between a photon and a surface plasmon, it embodies contributions from both the electromagnetic field and the collective oscillation of free electron gas. Consequently, SPPs can be excited using both photons and electrons. The conditions that need to be fulfilled in order to resonantly excite SPPs are conservation of frequency and conservation of in-plane momentum. Conservation of frequency is easily achieved but the same cannot be said for in-plane momentum when excitng with freely propagating light. In Figure 2.2, we can see that for any given frequency, the in-plane momentum for freely propagating light ($\omega = ck_x$) is always smaller than the in-plane momentum of surface plasmons.

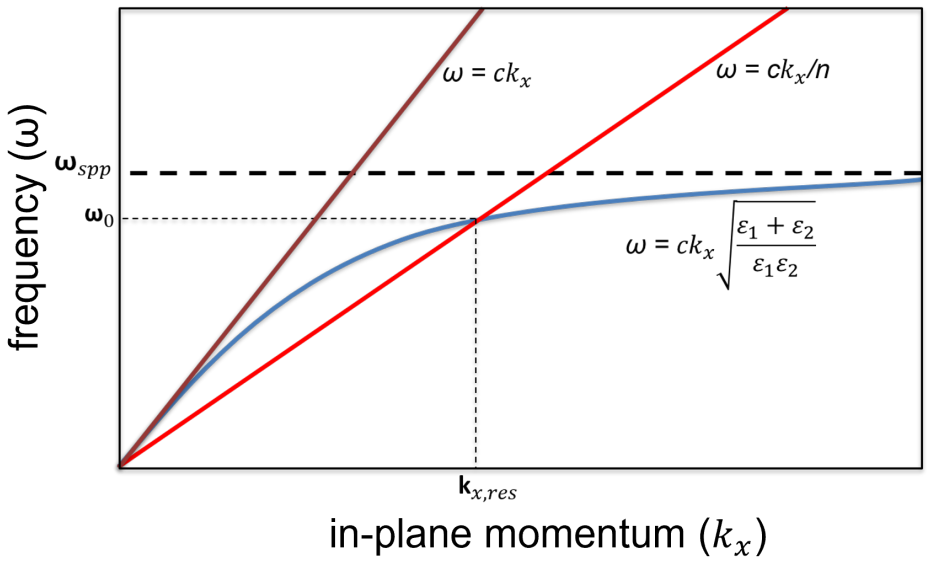

Figure 2.2: The brown line represent freely propagating light. The blue line shows surface plasmon polariton dispersion relation curve. The red line represents freely propagating light after a medium with a refractive index $n > 1$ has been inserted between air and plasmonic substrate. The intersection between the red and blue lines exhibits spp excitation using photons

As a result, the second condition is not fulfilled in this case and it is not possible to excite SPPs through freely propagating light unless additional momentum is provided to the incident photon. High-index prisms and gratings are commonly used to provide this additional momentum [11, 12, 21] and excitation of surface plasmon polariton waves become possible, as shown in Figure 2.2 with the ($\omega = ck_x/n$) line. In this research, we use a

variant of prism coupling by using a high numerical aperture objective-based Kretschmann configuration where incident radiation couples to SPP modes through a thin gold film (∼30 nm).

2.2.1 Properties of surface plasmon polaritons

The evanescent surface-bound SPP fields are p-polarized and have their maximum at $z = 0$ and decay exponentially as z increases. The field is given by

$$\mathbf{E} = \mathbf{E}_0 e^{i(k_x x \pm k_z z - \omega t)} \tag{2.12}$$

Here, $k = \frac{2\pi}{\lambda}$ where λ is the vacuum wavelength. The positive and negative signs correspond to the dielectric ($z > 0$) and metal ($z < 0$) sides, respectively. The expression does not contain any k_y component (for incoming beam propagating along the z-direction) as no surface-bound modes are present for s-polarization.

The dielectric function of metals is a complex number and its imaginary part accounts for the effects of ohmic losses at a metal-dielectric interface[21, 15].

$$\varepsilon_1 = \varepsilon_1' + i\varepsilon_1'' \tag{2.13}$$

Here, both ε_1' and ε_1'' are real numbers. This leads to a complex parallel wavenumber $k_x = k_x' + ik_x''$. This parameter describes the propagation of the SPP waves along the metal-dielectric interface. The real (k_x') and imaginary (k_x'') portions determine the wavelength of the SPP mode and its damping along the interface, respectively.

$$k_x' \approx \sqrt{\frac{\varepsilon_1' \varepsilon_2}{\varepsilon_1' + \varepsilon_2}} \frac{\omega}{c} \tag{2.14}$$

$$k_x'' \approx \sqrt{\frac{\varepsilon_1'\varepsilon_2}{\varepsilon_1'+\varepsilon_2}}\frac{\varepsilon_1''\varepsilon_2}{2\varepsilon_1'(\varepsilon_1'+\varepsilon_2)}\frac{\omega}{c} \tag{2.15}$$

The SPP wavelength can then be expressed in terms of the dielectric function and vacuum wavelength[21].

$$\lambda_{SPP} = \frac{2\pi}{k_x'} \approx \sqrt{\frac{\varepsilon_1'+\varepsilon_2}{\varepsilon_1'\varepsilon_2}}\lambda \tag{2.16}$$

As mentioned above, k_x'' describes the damping of the SPP field amplitude along the metal-dielectric interface. This damping gives rise to and exponential decay along the SPP propagation direction with $1/e$ decay length given by $1/k_x''$ for the field amplitude and $1/2k_x''$ for intensity. This ohmic loss-induced damping results in the heating of the metal. Considering the dielectric functions of two of the most used metals in plasmonics at $\lambda = 633$ nm, Ag ($\varepsilon = -18.2 + 0.5i$) and Au ($\varepsilon = -11.6 + 1.2i$), we can estimate their propagation lengths. At this wavelength, we determine the approximate $1/e$ intensity propagation lengths of ~ 60 μm and ~ 10 μm, respectively for Ag and Au. We have to keep in mind that these losses are calculated using the metal's bulk dielectric function. This approximation holds as long as the dimensions of the metallic structures are larger than the electron mean free path. For smaller structures, the likelihood of electron scattering from the interface increases. This leads to additional loss mechanisms that contribute to the local increase of the imaginary part of the metal's dielectric function[21].

Using a similar approach, we can also determine the evanescent field decay length associated with the SPP along the z-direction. The decay lengths into the dielectric and the metal can be calculated from $k_{1,z}$ and $k_{2,z}$ using the following expressions

$$k_{1,z} = \frac{\omega}{c}\sqrt{\frac{\varepsilon_1'^2}{\varepsilon_1'+\varepsilon_2}}\left[1 + i\frac{\varepsilon_1''}{2\varepsilon_1'}\right] \tag{2.17}$$

$$k_{2,z} = \frac{\omega}{c}\sqrt{\frac{\varepsilon_2^2}{\varepsilon_1' + \varepsilon_2}}\Big[1 - i\frac{\varepsilon_1''}{2(\varepsilon_1' + \varepsilon_2)}\Big] \tag{2.18}$$

Using the dielectric functions for Ag and Au at 633 nm, we determine the $1/e$ decay lengths to be $1/k_{1,z} = 23$ nm and $1/k_{2,z} = 421$ nm for Ag; and $1/k_{1,z} = 28$ nm and $1/k_{2,z} = 328$ nm for Au. This shows that the evanescent SPP waves penetrate into the dielectric over a longer distance than its penetration into the metal.

2.2.2 SPP-based sensing

SPPs allow nanoscale field confinement enabling sub-diffraction limited probing of chemical species with high sensitivity. SPP-based surface plasmon resonance (SPR) sensing has found applications in colorimetric chemical sensing, molecular diagnostics and lab-on-a-chip platforms, among others [13, 22]. SPR technology is currently the industry standard for measurement of biomolecular binding kinetics on plasmonic substrates [13]. SPPs have been used to enhance the sensitivity of fluorescence, Raman and nonlinear optical signals [23, 14, 24, 25].

The typical sensor implementation of SPR uses the uniform surface plasmon fields provided by SPPs and detects small changes in coupling angle, which reflects the local refractive index in the vicinity of the plasmonic substrate when molecular binding events take place. As with any biosensor, ensuring high selectivity is of utmost importance in SPR-based biomolecular sensing. Gold is usually the plasmonic substrate of choice due to the relative ease of tethering organic molecules through sulfur bonds to the gold surface [26, 27]. The ensemble averaged data obtained from this sensor can provide quantitative information on binding/dissociation kinetics, specificity and concentration of the sample of interest in real-time. However, due to the same inherently ensemble averaging nature of collected data here (Figure 2.3) [28],

information on individual molecules cannot be easily retrieved. The imaging variant of SPR sensor, known as SPR microscopy (SPRM), overcomes this limitation and enables direct visualization of individual particles [29, 30, 31, 32]. Imaging of cells, microorganisms, exosomes, DNA, RNA and proteins has been possible with SPRM [33, 34, 35, 36, 37, 38, 39]. However, SPRM methods suffer from compromised spatial resolution due to their non-ideal point-spread function (PSF) which is characterized by long-diffractive tails. The spatial resolution can be somewhat improved when advanced image processing techniques are implemented [37, 39].

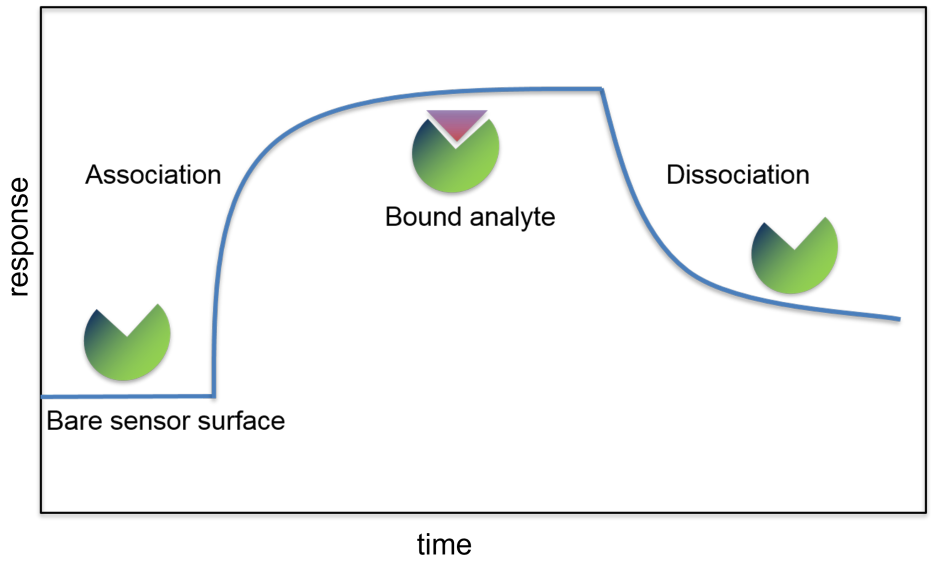

Figure 2.3: Typical surface plasmon resonance sensorgram showing variation in refractive indices upon binding and dissociation of moleculear targets. Retrieval of individual binding event information is problematic here

Another important sensing application of SPP is surface plasmon coupled emission (SPCE). In SPCE, a highly directional emission improves the collection efficiency, thus improving detection sensitivity [23]. SPCE has been used successfully in DNA sensing, aptamer-based protein sensing, oxygen sensing and more notably, in immunological sensing [40, 41, 42, 43]. Despite the fact that SPCE requires fluorescent labeling, it certainly is an improvement over traditional fluorescence-based sensing because of high detection sensitivity and efficient background suppression.

2.3 Localized surface plasmons

In the previous section, we have seen that SPPs are surface-bound propagating electromagnetic waves. In contrast, localized surface plasmons are non-propagating excitations of conduction electrons of metallic nanostructures that are coupled to an external electromagnetic field. These oscillations usually arise due to the scattering of sub-wavelength particles in an oscillating electric field. The subwavelength dimensions of the particle plays a pivotal role here. This surface exerts a restoring force on the oscillating electrons setting up a resonance, resulting in the enhancement of the electromagnetic field both inside and outside the particle. This resonance effect is known as localized surface plasmon resonance (LSPR). Unlike SPPs, no phase-matching conditions need to be fulfilled for LSPR excitation. As a result, direct illumination is sufficient for plasmon resonance excitation. For noble metals such as Ag and Au, the oscillation of conduction electrons can be resonantly excited with visible light, leading to their wide adoption as the materials of choice in plasmon-based sensing application.

2.3.1 Interaction of a sub-wavelength metal particle with an external electromagnetic field

A simple quasi-electrostatic approximation is sufficient in order to understand the interaction between a sub-wavelength spherical metal nanoparticle ($d \ll \lambda$) and an incident electromagnetic field. Under this assumption, the entire particle "feels" the same field across its entire volume. We consider a spherical metal particle with diameter a and dielectric function ε_m[21, 15, 11]. The metal is assumed to be surrounded by a dielectric medium with a dielectric function ε_d. While we will not show the detailed calculations here, we will discuss the main outcomes relevant to understanding the fundamentals of LSPRs.

If an external electromagnetic field with an amplitude $\boldsymbol{E_0}$ is applied along the z direction, the field can be described as $\mathbf{E} = \mathbf{E}_0 z$. In our quasi-electrostatic approximation we can use the solution of the Laplace equation for the potential, $\nabla^2\Phi = 0$. This allows us to calculate the electric field $\mathbf{E} = -\nabla\Phi$. The dipole moment $\mathbf{p}$ can be related to the field amplitude using the following expression.

$$\boldsymbol{p} = 4\pi\varepsilon_0\varepsilon_m a^3 \frac{\varepsilon - \varepsilon_m}{\varepsilon + 2\varepsilon_m}\boldsymbol{E_0} \tag{2.19}$$

This expression shows that the applied electric field induces a dipole moment which is proportional to $|\mathbf{E}_0|$. Another important parameter in our discussion is the polarizability α of the material, which can be related to $\mathbf{p}$ by $\mathbf{p} = \varepsilon_0\varepsilon_m\alpha\mathbf{E}_0$. This yields

$$\alpha = 4\pi a^3 \frac{\varepsilon - \varepsilon_m}{\varepsilon + 2\varepsilon_m} \tag{2.20}$$

This is the expression for the complex polarizability of a subwavelength spherical particle in the quasi-electrostatic approximation[21]. It can be inferred that the polarizability goes through a resonance while the denominator, $|\varepsilon + 2\varepsilon_m|$ is minimum. For a small or slowly changing imaginary dielectric function $\mathrm{Im}(\varepsilon)$, this yields

$$\mathbf{Re}[\varepsilon(\omega)] = -2\varepsilon_m \tag{2.21}$$

This is known as the Fröhlich condition and the associated oscillation is called the dipole surface plasmon of the nanoparticle. For a metallic particle following the Drude model (effects of interband transitions of bound electrons are neglected), the Fröhlich condition is fulfilled at $\omega_0 = \frac{\omega_p}{\sqrt{3}}$, assuming the surrounding medium is air. The resonance undergoes red-shifting as the value of ε_m is increased. This shifting of resonance as a function of dielectric function, or equivalently refractive index, serves as the foundation of SPR based optical sensing.

The resonance in α is accompanied by resonances in the internal and dipolar electric fields. They are given by

$$\mathbf{E}_{in} = \frac{3\varepsilon_m}{\varepsilon + 2\varepsilon_m}\mathbf{E}_0 \tag{2.22}$$

$$\mathbf{E}_{out} = \mathbf{E}_0 + \frac{3\mathbf{n}(\mathbf{n}\cdot\mathbf{p} - \mathbf{p})}{4\pi\varepsilon_0\varepsilon_m}\frac{1}{\mathbf{r}^3} \tag{2.23}$$

Here, $\mathbf{n}$ is the unit vector in the direction of the point being considered.

An important consequence of the resonantly enhanced polarization α is that the efficiencies at which the particle absorbs or scatters light are also increased. The expression of absorption and scattering cross-sections (C_{abs} and C_{scat} show a clear resonant behavior

$$C_{scat} = \frac{k^4}{6\pi}|\alpha|^2 = \frac{8\pi}{3}k^4a^6\Big|\frac{\varepsilon - \varepsilon_m}{\varepsilon + 2\varepsilon_m}\Big|^2 \tag{2.24}$$

$$C_{abs} = k\mathrm{Im}[\alpha] = 4\pi ka^3\mathrm{Im}\Big\{\frac{\varepsilon - \varepsilon_m}{\varepsilon + 2\varepsilon_m}\Big\} \tag{2.25}$$

For particles that are much smaller than λ, absorption effects ($\sim a^3$) dominate over scattering ($\sim a^6$). These expressions for C_{abs} and C_{scat} are valid for both metals and dielectrics. For particles with $a > 100$ nm, the quasi-electrostatic approximation is no longer valid as the change in the phase of the incident electromagnetic field over the entire volume becomes noticeable and can no longer be neglected. In such cases, more rigorous analytical approaches become necessary. Mie theory can solve this electrodynamic problem by accounting for the retardation. However, applicability of Mie theory is limited to spherical particles. In Mie

theory, the internal and scattered fields are expanded using a power series into a set of normal modes. The quasi-electrostatic approximation can be recovered by restricting this power series to the first order.

2.3.2 LSPR-based sensing

The ability of LSPR based antennas to localize incident electromagnetic radiation into nanoscale regions has led to important applications in chemistry, biology, energy and numerous other fields. LSPR based chemical sensing techniques are most commonly used for suface enhanced spectroscopy applications, such SERS, surface-enhanced fluorescence and surface-enhanced intrared absorption. A major portion of this dissertation focuses on SERS and its ultrafast analogue, SE-CARS for high-throughput molecular sensing.

As discussed above, the near-field coupling between metallic nanoparticles that support LSPR and incident electromagnetic radiation result in confined optical fields where light-matter interactions are strongly enhanced. In SERS, Raman active molecules located in the electromagnetic "hotspots" are efficiently driven in order to amplify the molecular signal. Over the past four decades, SERS has seen remarkable advances and single-molecule sensitivity has been achieved. The mechanisms behind field localization and enhancement in the SERS process are well-studied and rigorous electromagnetic theory can be found in literature discussing them in detail[16, 21, 8]. Briefly, the enhancement of Raman scattering is understood to be consisting of electromagnetic and chemical enhancement effects. Electromagnetic field enhancement originates because of LSPR mediated field localization due to the antenna property of the plasmonic substrate. Field enhancement factors as high as ~ 350 (or equivalently 10^5 intensity enhancement) have been reported[44]. On the other hand, the chemical enhancement effects arise due to changes in the electronic structure of molecules attached to metallic antennas. This charge-transfer mechanism causes some Raman-active

vibrational modes to undergo selective enhancement. Chemical enhancements on the order of ~ 100 have been reported[45]. Experimental observations strongly indicate that the majority of the enhancement effects originate from the electromagnetic contribution.

If we consider a Raman-active molecule placed inside an external electromagnetic field being driven at the pump frequency ω_p, the LSRP-mediated electromagnetic enhancement factor can be expressed as

$$\beta(\omega_p) = \frac{|\mathbf{E_{loc}}|}{|\mathbf{E_0}|} \tag{2.26}$$

The polarization $\mathbf{p}(\omega)$ of the molecule at the Stokes-shifted frequency ω_S can be expressed as

$$\mathbf{p}(\omega_S) = \alpha^R(\omega_p - \omega_S)\mathbf{E}(\omega_p) = \alpha^R(\omega_p - \omega_S)\beta(\omega_p)\mathbf{E}_0(\omega_p) \tag{2.27}$$

Here, $\alpha^R(\omega)$ is the Raman contribution to the molecule's electronic polarizability. The polarization radiates through the dipolar mode of the metallic nanoantenna and subsequently couples to the radiative field with an enhanced efficiency $\beta(\omega_S)$. The intensity of the SERS signal can then be expressed as

$$I_{SERS}(\omega_S) \propto |\beta(\omega_S)\mathbf{p}(\omega_S)|^2 = |\alpha^R(\omega_p - \omega_S)|^2|\beta(\omega_S)|^2|\beta(\omega_p)|^2|\mathbf{E}_0(\omega_p)|^2 \tag{2.28}$$

As the difference between ω_p and ω_S is much smaller than the linewidth of the localized surface plasmons, we can consider $\beta(\omega_p) \approx \beta(\omega_S)$. We can then predict the overall electromagnetic enhancement of the SERS process to be $\sim \beta^4$.

LSPR based chemical sensing systems rely on nanogaps between metallic nanostructures or sharp features of single nanostructures in order to produce local electromagnetic hotspots. Generally, clusters of metallic nanoparticles are preferred for SERS or surface-enhanced

fluorescence sensing due to the high likelihood of nanogap formation. The intense fields generated in these gaps have been successfully exploited to achieve single-molecule sensitivity [18, 46]. A number of other geometries have been explored as SERS substrates. Arrays of nanopillars, nanoholes, sharp metallic tips, metallic shells, core-and-shell nanoparticles and metal-insulator-metal structures are some of the well-explored geometries that have found success as SERS substrates. Most of these studies focus on gold and silver as the enhancement structure material due to their strong LSPR response in the visible and NIR regime.

The same field localization mechanism enhances the emission from fluorescent molecules. Nanostructures, similar to the ones mentioned in the case for SERS, have been explored for surface enhanced fluorescence (SEF). The general idea for field localization remains the same. Aggregates of plasmonic nanoparticles with narrow gaps are routinely used to enhance fluorescence signal. Sizes and shapes of the nanoparticles assemblies are modified to tune their resonances. This tunability allows efficient coupling and excitation of the fluorescent molecule and subsequent radiation. However, the fluorescence is quenched when the target molecule is placed too close to the metal surface. In such cases, a thin dielectric spacer layer is applied to minimize the transfer of non-radiative energy from the molecule to the metal.

2.4 Dielectric nanoantennas for chemical sensing

Optical antennas are structures that enhance light-matter interaction by efficiently converting propagating optical radiation to localized energy, and vice versa. The quality of an antenna is defined by the efficiency at which it can localize propagating optical fields (or vice versa) and how well it can couple near-field information in the hotspot to far-field radiation. According to the principle of reciprocity, optical antennas can simultaneously operate in both transmitting and receiving modes[21]. Figure 2.4a illustrates a antenna converting

near field into a freely propagating radiation. On the other hand, figure 2.4b shows the same antenna localizing incident propagating field into a confined near field.

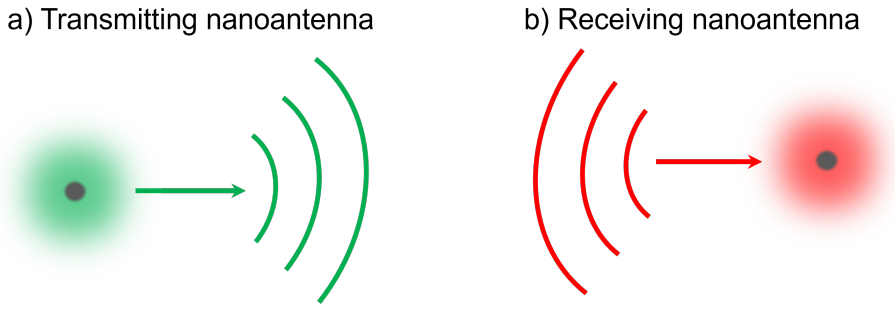

Figure 2.4: A simple schematic illustration of a (a) transmitting and a (b) receiving optical antenna

Advances in fabrication techniques have enabled shrinking optical antennas to nanoscale dimensions. These nanoantennas have found widespread applications in optical sensing, analytical chemistry, bio-imaging and advanced photodetector technologies to name a few. Most optical nanoantennas explored for sensing applications feature metallic nanostructures due to their surface plasmon resonance in the visible range. However, these metals are known to be adversely affected by large ohmic losses and subsequent heating effects cause morphological changes to the metallic structures, rendering them unusable. High-index dielectric particles hold promise as alternatives to metallic nanoantennas due to their low-loss nature, strong scattering efficiency and electromagnetic field localization capabilities for surface-enhanced spectroscopy, chemical sensing and nonlinear nanophotonic applications.

2.4.1 Nature of dielectric field confinement

Previously, we have discussed the response of sub-wavelength spherical nanoparticles inside an incident electromagnetic field. We can extend the approach to dielectric particles as well in order to understand the nature of field confinement in these materials. Mie theory provides an analytical framework to represent the scattered electromagnetic field as a sum of electric-type (transverse magnetic, TM) and magnetic-type (transverse electric, TE) spherical harmonics.

The amplitudes of these harmonics are represented by the coefficients a_n and b_n for the electric and magnetic modes, respectively. At resonance, the fields associated with each harmonic are enhanced both inside and outside the material. Unlike metallic nanoantennas where the enhancement of the electric field relies on the resonant oscillation of free electrons, the optical response of high-index dielectric particles arise from displacement currents that are associated with the movement of bound electrons(Figure 2.5).

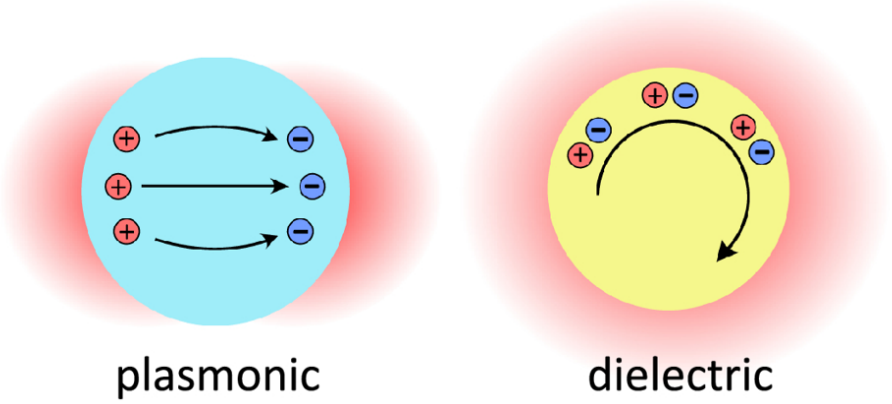

Figure 2.5: Comparative illustration of optical response of metals and dielectrics [1]

Some of these particles such as Si, Ge and GaP have magnetic response in the optical regime which provides an additional channel for field confinement that is not available to metallic nanoantennas. For a given diameter of the nanoparticle, the magnetic dipole response can be observed at the lowest energy Mie resonance. In addition, these dielectric nanoantennas are able to control the directionality of far-field radiation due to the coherent mixture of the electric and magnetic modes [47, 48]. When two (or more) of these particles are brought together and properly excited, magnetic dipoles couple with each other in addition to electric dipole coupling, and, subsequently, enhanced near-fields are produced[2]. In figure 2.6, we consider the response of this dimer nano-antenna system using two orthogonal polarizations and compare that with a plasmonic antenna with similar dimensions. For the metallic dimer nanoantenna system, an electronic resonance mediated by localized surface plasmons generates an electric field hotspot when the incident field is polarized along the dimer axis. However, field confinement is not expected for orthogonal polarization. The dielectric dimer

nanoantenna system, on te other hand, is able to demonstrate strong coupled resonances, followed by field confinement, for both polarization schemes. Electric dipoles are induced for polarization along the dimer axis and magnetic dipoles are induced for orthogonal polarization.

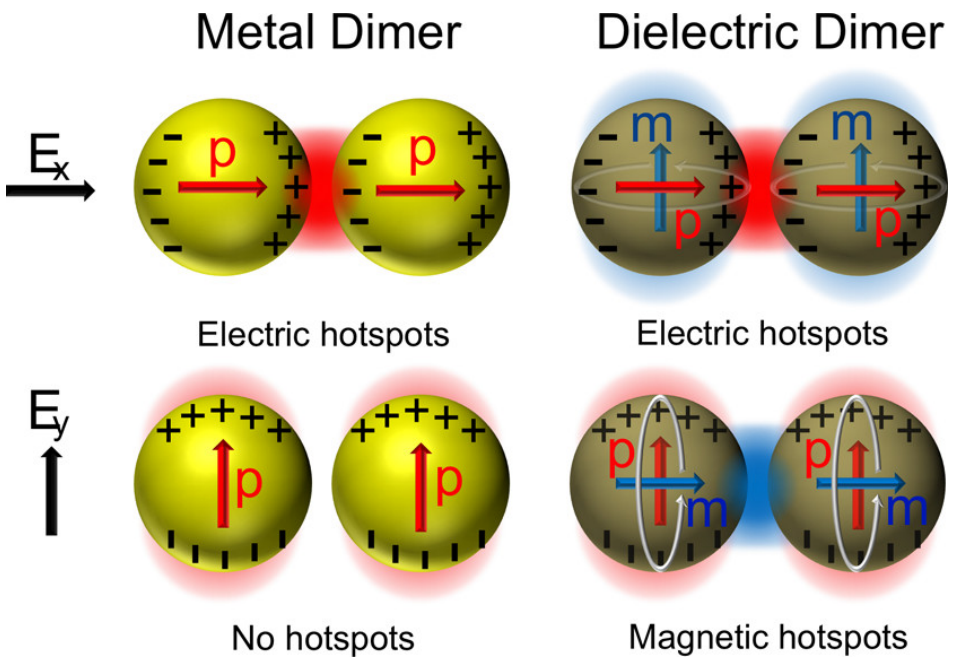

Figure 2.6: Comparative illustration of metallic and dielectric dimer nano-antennas generating electromagnetic hotspot. Reproduced with permission [2].

Generally, the light-dielectric material interaction in a homogeneous medium are explained with the help of Mie-Debye-Lorenz theory [8, 49]. For a dielectric sphere, the curvature of the surface of the sphere and the discontinuity in the refractive index affect the spatial distribution inside and outside the particle r. The scattering efficiency Q, which is the ratio of the power of the scattered light to that of the incident light, can be expressed as

$$Q_{scat} = \frac{2}{k_o r^2} \sum_{l=1}^{\infty} (2l+1)(|a_l|^2 + |b_l|^2) \tag{2.29}$$

where the coefficients a_l and b_l are scattering coefficients. The coefficients are functions of spherical Bessel function (j_l), spherical Hankel function of the n-th kind ($h_l^{(n)}$), dielectric function of the particle (ε_d), dielectric function of the media (ε), wavenumbers inside (k_i)

and outside (k_o) of the particle and the radius of the particle. Subsequently, the scattering efficiency in the near-field can be expressed as[50]

$$Q_{NF} = 2\sum_{l=1}^{\infty}\{|a_l|^2[(l+1)|h_{l-1}^{(2)}(k_0 r)|^2 + l|h_{l+1}^{(2)}(k_0 r)|^2] + (2l+1)|b_l|^2|h_l^{(2)}(k_0 r)|^2\} \quad (2.30)$$

This equation can be readily applied to calculate the electric and magnetic field distribution near a dielectric particle.

An interesting study was reported in which antenna properties of 100 nm Ag and Si particles were compared [51] in order to understand the feasibility of dielectric nanoantennas. The extinction property of Ag was characterized using the LSPR modes, while Si particles demonstrated Mie type modes arising from the spatial confinement of incident electromagnetic radiation. Calculation of the near-field scattering efficiency Q_{NF} revealed that the resonances in the near and far-field are similar, with minute variation in the positions and shapes of the peaks. These calculations show that the Si particles can be as efficient as plasmonic Ag particles in localization of external optical fields. This observation underlines the efficacy of Mie resonances in field confinement applications for non-plasmonic materials.

2.4.2 Chemical enhancement in dielectric nanoantenna based spectroscopy

We have already discussed electromagnetic field enhancement mechanisms in metallic and dielectric based nano-antennas. There are also direct interactions between the molecule and the substrate that play a role (albeit relatively minor) in enhancing light-molecule interactions. These effects arise due to transfer of charges between the substrate and the analyte through a conductive "bridge". Charge-transfer resonance between the Fermi level (or band-edges for semiconductor materials) and the molecular level provides a resonant condition for chemical

enhancement. There is also a non-resonant condition in which a substrate-molecule complex is created, resulting in a large increase in the polarizability in the ground state. To achieve a deeper understanding of the chemical enhancement in SERS or SEF process, the combined molecule-substrate system has to be analyzed. The polarizability α of the molecule goes through considerable modification once it is chemisorbed on the substrate, as new electronic states are introduced. In case of SERS (or SE-CARS), which is one of the central themes of this dissertation, the Raman spectrum of the target molecule undergoes noticeable modification compared to the corresponding spontaneous Raman spectrum of the free molecule. For metals, adequate theoretical groundwork exists. The two-state model is a well-known framework in which a Green's function approach of the nonequilibrium junction is combined with a general scattering theory. In one of the models based on this approach, a molecule is considered to be coupled to two electrodes in such a way that HOMO and LUMO of the target molecule each connect with one of the electrodes [52, 53]. The Hamiltonian of the system is composed of interactions between the molecular vibrations and tunneling electrons along with the coupling between the molecular vibration and the thermal bath. This approach is accurate to all orders of perturbation theory and considers both weak and strong coupling regimes. This model is able to individually quantify relative contributions of the molecular and metal-molecule charge transfer processes. The model suggests that the molecular enhancement is stronger when the incident radiation is tuned closer to the electronic resonance of the molecule. However, these resonances may not always dominate the scattering intensity due to interference effects between molecular and excitonic resonances[54, 8].

Another implementation of the two-state model suggests that the chemical enhancement is directly related to the HOMO-LUMO gap [55]. The proponents of this model argue that the molecule/substrate system stabilized by π bonding is capable of modifying the polarizability α of the molecule, leading to enhancement of the Raman signal. Under nonresonant

conditions, the derivative of α with respect to the k^{th} normal mode Q_k can be expressed as

$$\frac{\partial \alpha_{\alpha,\beta}}{\partial Q_k} = -\frac{(\mu_{CT,\alpha} E_\alpha)(\mu_{CT,\beta} E_\beta)}{\omega_{CT}^2} \Big(\frac{\partial \omega_{CT}}{Q_k} \Big) \tag{2.31}$$

here, ω_{CT} is the frequency of charge-transfer resonance and μ_{CT} is the dipole moment for the lowest charge-transfer transition. If we consider ω_{mol} to be the frequency corresponding to the HUMO-LUMO gap, the chemical enhancement factor is then given by $EF = A(\frac{\omega_{mol}}{\omega_{CT}})$. Here, A is a constant. Both of the models discussed above have been confirmed with DFT calculation. There is also a unified resonance model by Albrecht et al., in which the excitation of molecules were explained by considering the polarizability α as a sum of different terms. Each of the terms involve an infinite sum over all molecular states [56, 57, 58]. This model is only valid in the weak-coupling regime and it reduces to the earlier two models that we discussed when the excitation is tuned far from resonance.

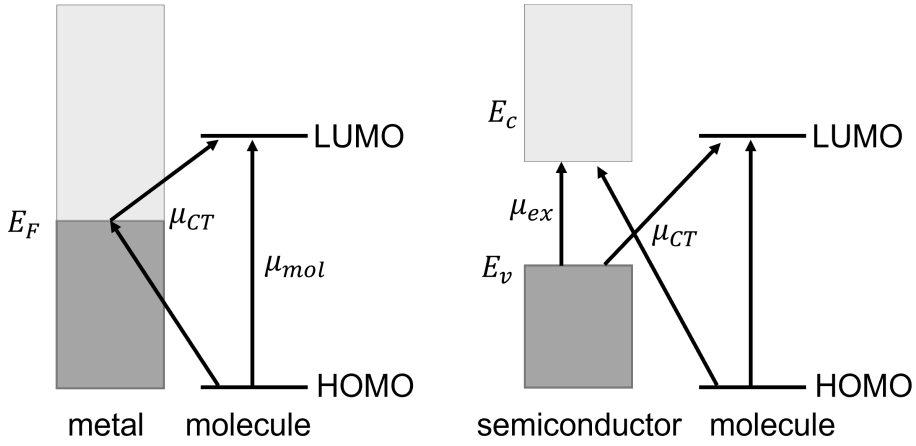

Figure 2.7: Charge-transfer mechanism at metal/molecule and metal/semiconductor systems. The dark shaded regions represent the valence band, the light shaded regions represent the conduction band and E_F denotes the Fermi level.

The models that we discussed above were developed considering plasmonic antennas only. The general framework, however, can be modified and extended for dielectrics as well. In Si, Ge and other similar dielectric materials, the Fermi level is not directly available for charge transfer. Instead, the transfer of charges occur here either into the conduction band

or out of the valence band, as shown in figure 2.7. In these materials, excitonic or interband transition creates electron-hole pairs. This resonance can contribute to SERS enhancement in a manner similar to molecular resonances in metal-based SERS. As a result, excitonic resonances provide another pathway for SERS enhancement with dielectric materials. The expansion of the polarizability α contains a sum over many of these terms. However, very few of those effectively contribute to the overall SERS enhancement depending on the wavelength of the incoming field.

2.4.3 Choosing the right dielectric material

While selecting dielectric particles for surface-enhanced spectroscopy application, some factors need to be considered. First, we need to consider the refractive-index of the material. Mie resonances show a strong dependence on the difference between the refractive indices of the particle and the surrounding medium. Figure 2.8 nicely illustrates this. Calculations of scattering cross sections of large ($d = 2\mu m$) Si and SiO_2 particles clearly show that high-index Si demonstrates strong Mie resonances, while low-index SiO_2 does not exhibit any such behavior.

Second, absorption losses need to be taken into account while choosing the dielectric material due to their ability to weaken Mie resonances. The absorption properties of the material can be found by analyzing the imaginary part of the refractive index of the material, $\tilde{n} = n + ik$, where n is the real refractive index and κ is the extinction coefficient. The extinction coefficient is directly related to the absorption coefficient α through, $\alpha = \frac{4\pi\kappa}{\lambda}$. Semiconductors such as Si, Ge, GaAs, GaP and InP are known to exhibit some of the highest refractive indices in our preferred spectral window while producing low absorption losses (see table 2.1).

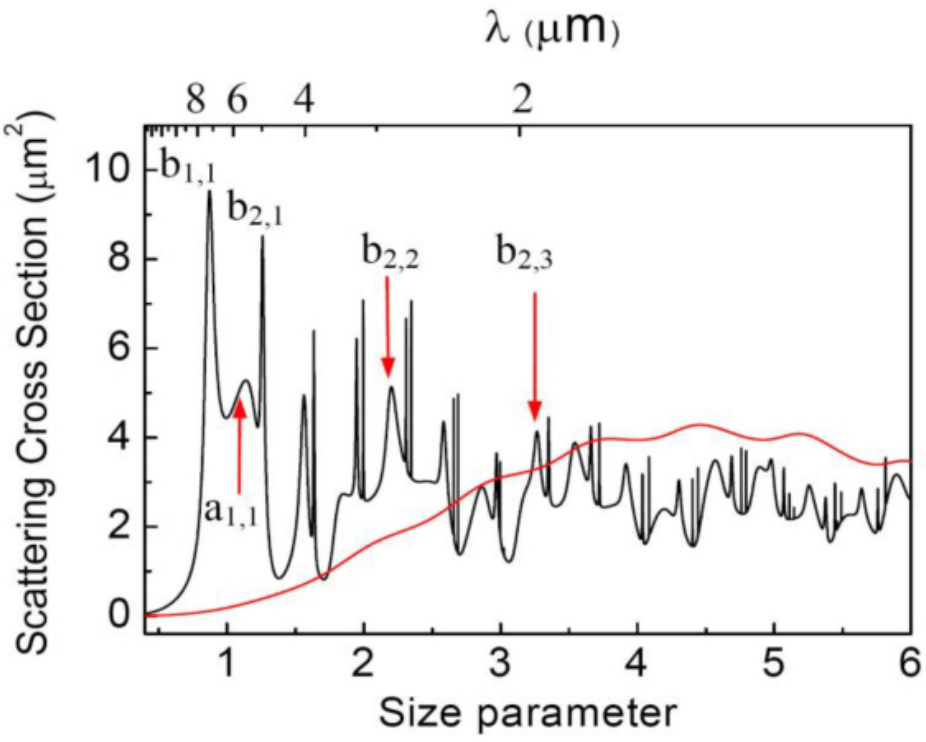

Figure 2.8: Comparative illustration of Mie resonances for different size parameters ($x = \frac{2\pi r}{\lambda}$) of low-index SiO_2 (red lined) and Si microparticles (black line) [3].

Material	**Spectral Range**, μm	**Refractive Index**, n	**Extinction Coefficient**, k
Si	0.50–1.45	4.293–3.486	0.045–0.001
GaAs	0.50–0.80	4.037–3.679	0.376–0.089
GaP	0.50–0.80	3.590–3.197	∼0
InP	0.50–0.80	3.456–3.818	0.203–0.511
TiO_2	0.50–1.00	2.715–2.483	∼0
Ge	0.50–0.60	4.460–5.811	2.366–1.389
	0.60–0.80	5.811–4.699	1.389–0.3
	0.80–1.90	4.684–4.129	0.3–0.001

Table 2.1: Comparison of refractive index of dielectric materials of interest [1]

2.4.4 Surface-enhanced Raman scattering (SERS) with dielectric nanoantennas

In the previous sections, we have discussed how dielectric materials can enhance light-matter interactions, particularly Raman scattering of molecules, through electromagnetic and chemical enhancement mechanisms. By modifying the size, shape and other geometrical param-

eters, one can take advantage of one or more of these enhancement mechanisms.

In this dissertation, we explore Si as the antenna material for dielectric SE-CARS studies. The abundance of the material in nature along with favorable optical and thermal properties have contributed to its integration into some analytical platforms. The first demonstration of Si based SERS came in the form of Si nanoparticles where ∼100 fold enhancement of Raman scattering was observed [59]. Roughened Si electrodes have been studied to understand the morphological dependence on SERS enhancement [60, 61]. The pioneering Si nanowire based SERS study by Cao et al. achieved an enhancement of $\sim 10^3$ under 785 nm excitaion [62]. Subsequent work on similar vertically oriented structures explored tuning the size and shape of the wires to achieve higher enhancements [63, 64]. These studies, however, involved the enhancement of Raman spectrum from Si itself and did not include the detection of any analyte. Wells et al. investigated various other nanostructures such as Si nanopillars for SERS enhancement NHS-rhodamine dyes. This particular nanoantenna exhibited an enhancement factor of ~ 200 with a detection sensitivity in range of few tens of attomoles [65]. Si and Ge nanowire based SERS also showed success in enhancing the Raman signal from a number of other dye molecules including N719 and PATP. Some of these work involved hydrogenation of substrate surfaces for efficient charge-transfer [66]. The work also showed that the efficiency of the charge-transfer process can be tuned by controlled doping of the antenna. n-type Si structures showed Si-to-molecule electron injection and p-type structures allow molecule-to-Si charge transfer.

While progress in Si-based SERS has been sporadic since its first observation, the quest for metal-free SERS has gained momentum over the last decade. Rodriguez et al. used mechanically milled Si nanoparticles to achieve SERS enhancement of *para*-aminobenzoic acid (PABA) molecules in which the effective enhancement was similar to plasmonic SERS [67]. This work showed that Si based nanostructures are prime candidates as nanoantennas for molecules that do not contain functional groups with strong affinity for noble metals. In

such cases Si based antennas can provide similar enhancements to plasmonic antennas while producing reproducible and stable SERS signals.

One of the major reasons behind choosing Si as the antenna material in Chapters 4 and 5 is its favorable thermal property, particularly its lower optical absorption and higher specific heat of (5x higher compared to Au [68]). Maier et al. investigated the heating effects on dielectric Si and GaP dimer nanoantennas and compared that with Au antennas of the same dimensions [5, 4]. The results in Figure 2.9 show that Si based structures produced 18 times lower increase in temperature compared to Au nanoantennas. This low heating has important implications in SERS studies and its importance becomes even more significant when ultrafast irradiation is involved, such as in SE-CARS applications. This lower heating protects the antennas from disintegrating, prevents the target molecule from getting damaged and improves the stability and reproducibility of the signal.

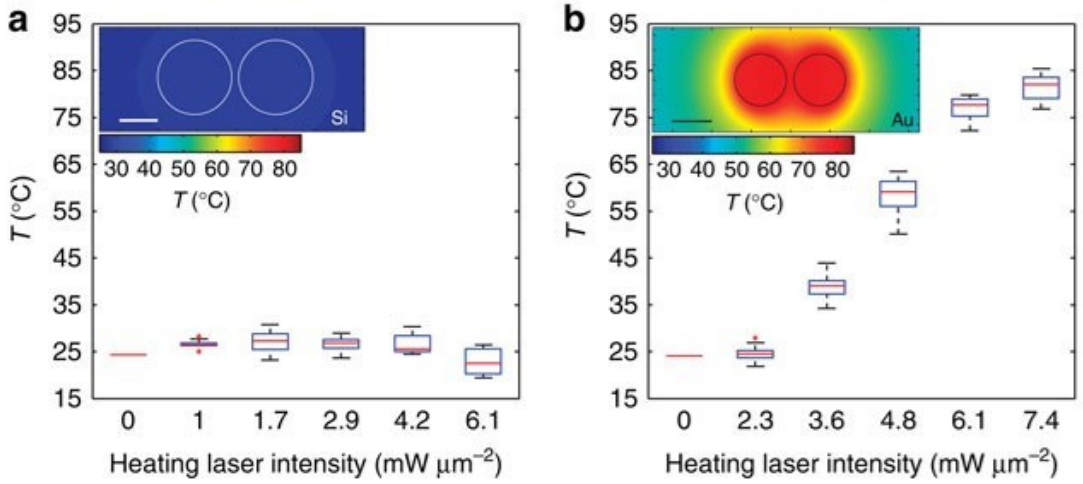

Figure 2.9: Comparision of thermal effects in (a) Si and (b) Au dimer based nanoantennas. The calculated temperature maps in the inset for both (a) and (b) are calculated for 5 mW/μm^2 excitation field. Reproduced with permission from [4]

Similar results were obtained when comparing GaP dimer nanoantennas with similarly structured Au based ones, as seen in Figure 2.10 [5]. An interesting fact to note here is that the GaP antenna does not produce any heat at all as the imaginary part of the dielectric function for GaP approaches zero in the visible range, resulting in no resistive losses.

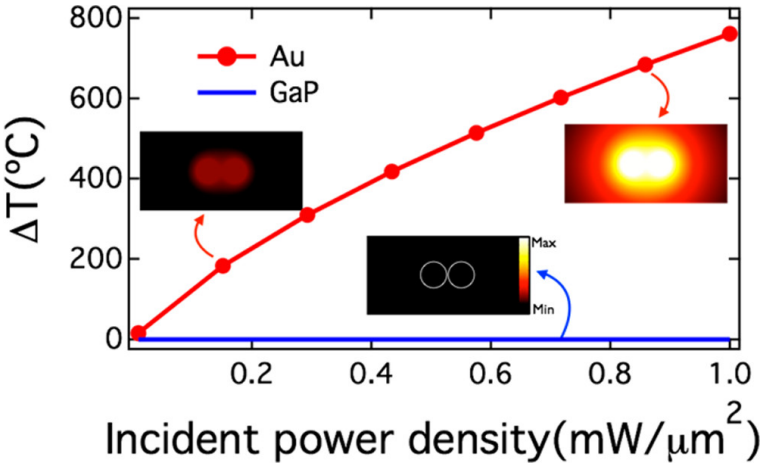

Figure 2.10: Comparision of thermal effects in (a) GaP and (b) Au dimer based nanoantennas. The calculated temperatures show significant heating in Au based nanoantenna, while no noticeable heating was predicted in the dielectric one. Reproduced with permission from [5]

Other materials apart from Si have also been explored as dielectric nanoantennas for SERS. By tuning their optical and chemical properties along with their morphology, amplification of Raman scattering has been achieved. Table 2.2 summarizes some of the examples of dielectric based SERS investigation along with the shape of the antenna and main enhancement route.

Material	Shape	Main contribution to enhancement	Ref
TiO_2	nanoparticles	CT	[69, 70, 71, 72]
	nanoparticles	QC	[73, 74, 75]
	nanofibers	EM	[76, 77]
	spherical core/shell beads	EM	[78, 79]
	3D inverse opals	EM	[80, 81]
ZnO	nanocrystals, nanorods, nanowires	CT	[82, 83, 84]
	nanoporous 3D network	CT	[85]
	1D nanostructures	EM	[86, 87]
CuO, Cu_2O	nanocrystals	CT	[88, 89, 90, 91]
	nanospheres	CT + EM	[92]
$AgFeO_2$	nanoparticles	CT + EM	[93]
α-Fe_2O_3	nanoparticles	CT	[94, 95]
Fe_3O_4	nanoparticles	CT	[96]
SnO_2	nanoparticles	CT	[97]
V_2O_5	nanoparticles	CT	[98]
ReO_3, W_xO_y	nanoparticles	CT + EM	[99, 100]
SiO_2	microspheres	EM	[101, 102]
TiO_2, Fe_2O_3 composites	nanocomposites	CT + EM	[103, 104, 105]
	nanoparticles	CT + EM	[106, 107]
	quantum dots	QC + CT	[108, 109]
Si, Ge	low-density nanowire arrays	EM	[63, 64, 110]
	high-density nanowire arrays	CT, EM	[66, 59, 61]
	nanoparticles	EM	[67, 111]
	Si/TiO_2 heterostructures	EM	[112]

Table 2.2: Summary of recent studies involving dielectric materials for SERS enhancement. CT, charge transfer mediated enhancement; EM, electromagnetic enhancement; QC, quantum confinement based enhancement. Reproduced from [8] with permission

2.5 Nonlinear optical phenomena and their plasmonic enhancements

Nonlinear optics is a branch of photonics where the response of a material system changes in a nonlinear fashion when stimulated by a strong incident optical field [10]. The response here is described by the polarization density $\mathbf{P}(t)$:

$$\mathbf{P(t)} = \varepsilon_0 \Big[\chi^{(1)}\mathbf{E}(t) + \chi^{(2)}\mathbf{E}^2(t) + \chi^{(3)}\mathbf{E}^3(t) + ... \Big] \tag{2.32}$$

where ε_0 is the permittivity in vacuum and $\chi^{(n)}$ is the n-th order susceptibility of the material of interest [10].

Higher order susceptibilities ($n > 1$) only come into play for strong incident fields, which was

experimentally not possible to achieve before the development of laser in 1960 [9]. Only after this important invention, light sources with sufficient intensity became available and innovation in the field of nonlinear optics took off. Important second-order optical processes include second-harmonic generation (SHG), sum-frequency generation (SFG), difference-frequency generation (DFG), whereas third-harmonic generation (THG), two-photon absorption (TPA) and four-wave mixing (FWM) are the most common third-order processes. While third-order processes can be observed in all materials, second-order processes are limited to structures with broken centrosymmetry within the dipolar approximation of light-matter interaction [10]. In this dissertation, we study two different third-order nonlinear optical processes and their plasmonic enhancement. In chapter 3, we study two-photon absorption from planar gold surfaces and how the subsequent fluorescence is enhanced when nanoparticles are placed near the surface. In chapters 4 and 5, we study coherent anti-Stokes Raman scattering (CARS) and its enhancement through plasmonic and non-plasmonic antennas.

2.5.1 Two-photon absorption (TPA) and coherent anti-Stokes Raman scattering (CARS)

In two-photon absorption, two photons of identical (degenerate TPA) or different (non-degenerate TPA) energies are simultaneously absorbed by the material and the combined energy matches the transition energy from the ground state to an excited state of the material [10], as shown in Figure 2.11a. Although the absorption process requires two photons, the material response is third-order in the incoming fields. After a phonon-coupled non-radiative relaxation, the excess energy in the material is released through radiation, the resulting process is referred to as two-photon excited fluorescence (TPEF).

In coherent anti-Stokes Raman scattering (CARS), two pulsed laser sources with sufficiently high intensities are used to coherently drive Raman-active vibrational modes within

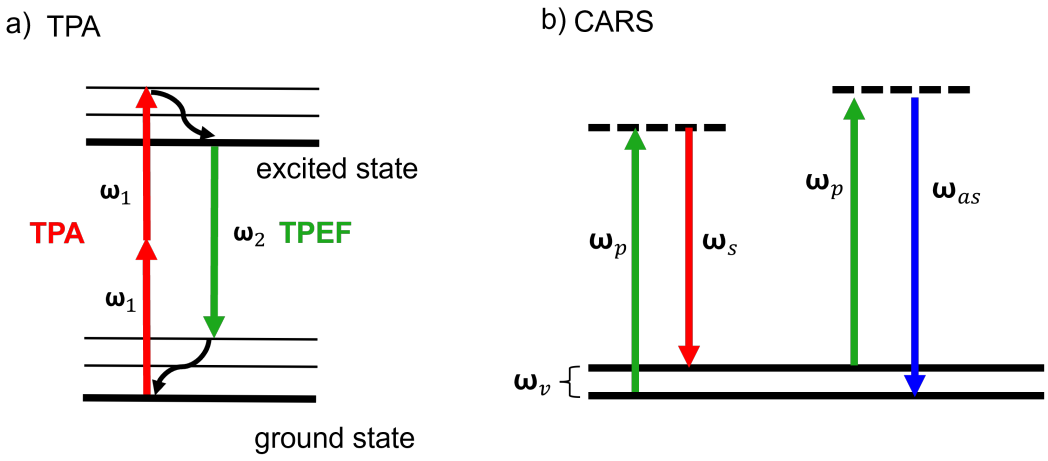

Figure 2.11: Jablonski diagrams of (a)TPA and (b) CARS

a molecule. The frequencies of the two beams, called pump (ω_p) and Stokes (ω_S), are chosen such that their difference matches the frequency of the vibrational mode-of-interest (Figure 2.11b). After interacting with a third field which is usually derived from the pump beam, the material may return to the ground state under the emission of a blue-shifted field at the anti-Stokes frequency ($\omega_{as} = 2\omega_p - \omega_s$). The resulting CARS signal can be orders-of-magnitude more intense than the corresponding spontaneous Raman scattered signal [113].

2.5.2 Enhancement of nonlinear optical effects

Plasmonic enhancement of nonlinear optical phenomena began with second-harmonic generation (SHG) in 1974 when Simon et al. achieved a 30 fold increase in the SHG signal with propagating SPPs supported on a thin silver film [114]. In 1981, a 10^4 enhancement of SHG signal was observed by Chen et al. on an electrochemically roughened silver surface relative to a flat reference film using non-propagating localized surface plasmons (LSP) [115]. Along with this widely-explored second-order process, plasmonic enhancement of third-order optical processes such as THG [116, 117], TPA [118, 119] and FWM [120, 24, 121, 25] have also been investigated over the past few decades.

Plasmonic enhancement of CARS was inspired by the advent of surface-enhanced Raman scattering (SERS), a spectroscopic technique that has enabled enhancement of the notoriously weak Raman signal and made single molecule detection possible through LSPs supported by metallic nanostructures [18, 122, 46]. As SERS uses the amplifying qualities of LSPs, the field is not uniform across the entire field-of-view, making it incompatible with wide-field imaging applications. Widefield SPP illumination, on the other hand, provides uniform field enhancement in the two-dimensional sample plane [11]. SPP mediated CARS generation with subsequent far-field detection was demonstrated as early as in 1979 [123]. After that proof-of-principle study, investigation regarding plasmonically enhanced coherent Raman scattering (CRS) remained mostly unexplored while advances in CARS microscopy surged in the late 1990s and early 2000s [124, 125, 126, 127]. Recent literature includes a number of LSPR mediated SE-CARS micrcosopy studies [128, 129, 130, 131]. The first wide-field SE-CARS microscope was developed in 2016 enabling wide-field CRS imaging with a million-fold enhancement in detected signal [24]. Subsequent work on wide-field SE-CARS has successfully demonstrated three-dimensional imaging of live-cells [132].

2.5.3 Nanoantenna mediated enhancement in SE-CARS

A deep understanding of the SE-CARS process requires a detailed theoretical framework of surface-enhanced coherent Raman scattering. However, no such theory has yet been developed. The theories used for SERS are borrowed and extended to interpret results obtained from SE-CARS experiments. As with SERS, it is assumed that the primary enhancement mechanism is governed by electromagnetic effects. Considering a molecular dipole placed in close proximity to a spherical particle with reasonably high polarizability α, the local electric field $\mathbf{E_{loc}}(\mathbf{r}, \omega_p)$ is modified due to the interaction between the particle and molecular dipole.

The local field $\mathbf{E_{loc}}(\mathbf{r}, \omega_p)$ can be expressed as[20]

$$\mathbf{E_{loc}}(\mathbf{r}, \omega_p) = \mathbf{E}(\mathbf{r}, \omega_p) + \mathbf{E_p}(\mathbf{r}, \omega_p) \tag{2.33}$$

Here, $\mathbf{E}(\mathbf{r}, \omega_p)$ is the incident field applied to a molecule placed at $\mathbf{r}$ and $\mathbf{E_p}(\mathbf{r}, \omega_p)$ is the field scattered by the particle in response to the pump field. Similarly, the local field in response to the incoming Stokes field can be expressed as

$$\mathbf{E_{loc}}(\mathbf{r}, \omega_s) = \mathbf{E}(\mathbf{r}, \omega_s) + \mathbf{E_s}(\mathbf{r}, \omega_s) \tag{2.34}$$

Here, $\mathbf{E_s}(\mathbf{r}, \omega_s)$ is the field scattered by the particle in response to the Stokes field. The amplitude of the nonlinear polarizations of the molecule at the Stokes (ω_s) and anti-Stokes (ω_{as}) frequencies can be written as

$$\mathbf{p}(\mathbf{r}, \omega_{as}) = \{(\frac{\partial \alpha}{\partial Q})_0 \xi(\Omega)\} E^2(\omega_p) E^*(\omega_s) = \gamma_v(\omega_{as}) E^2(\omega_p) E^*(\omega_s) \tag{2.35}$$

$$\mathbf{p}(\mathbf{r}, \omega_s) = \{(\frac{\partial \alpha}{\partial Q})_0 \xi(\Omega)\}^* |E(\omega_p)|^2 E(\omega_s) = \gamma_v^*(\omega_s) |E(\omega_p)|^2 E(\omega_s) \tag{2.36}$$

Here, $\gamma_v(\omega_{as})$ and $\gamma_v(\omega_s)$ are third-order hyperpolarizabilities of the target molecule, and $\xi(\Omega)$ is the frequency dependent responsiveness of the molecule. This Ω here is defined as the frequency difference between the pump and Stokes fields, $\Omega = \omega_p - \omega_s$.

The far field radiation at a point $\mathbf{R}$ can be written as

$$\mathbf{E}(\mathbf{R}, \mathbf{r}, \omega) = \mathbf{E}_d(\mathbf{R}, \mathbf{r}, \omega) + \mathbf{E}_{scat}(\mathbf{R}, \mathbf{r}, \omega) \tag{2.37}$$

Here, the last field term is the field scattered by the dipole located at $\mathbf{r}$ and observed from

R. When the particle is excited at its resonances (for a metallic particle, it will be the plasmonic resonance), we can reasonably expect $\mathbf{E}_{scat} \gg \mathbf{E}_d$ and the molecular response is radiated through the particles dipolar mode. Using this formalism, it can be shown that the overall enhancement in the SE-CARS process can be orders-of-magnitude stronger than what is achievable through SERS. We can rewrite 2.33 as

$$\mathbf{E}(\mathbf{r}, \omega_p) \approx [1 + F(\mathbf{r}, \omega_p)]\mathbf{E}(\mathbf{r}, \omega_p) \tag{2.38}$$

Similarly, we can rewrite 2.37 as

$$\mathbf{E}(\mathbf{R}, \mathbf{r}, \omega) \approx [1 + F(\mathbf{r}, \omega)]\mathbf{E}_d(\mathbf{R}, \mathbf{r}, \omega) \tag{2.39}$$

Using these, we can write the CARS signal field as

$$\mathbf{E}(\mathbf{R}, \mathbf{r}, \omega) \propto [1 + F(\mathbf{r}, \omega_{as})]\gamma(\omega_{as})[1 + F(\mathbf{r}, \omega_p)]^2\mathbf{E}^2(\mathbf{r}, \omega_p)[1 + F(\mathbf{r}, \omega_s)]^* E^*(\mathbf{r}, \omega_s) \tag{2.40}$$

The fields that are scattered by the particle are much more intense compared to the ones that are scattered by the molecule alone and also the incident fields. As a result, we can write $[1 + F(\mathbf{r}, \omega)] \approx \beta(\omega)$. We can then write the SE-CARS intensity at the far-field as

$$I_{as} \propto |\beta(\omega_p)\mathbf{E}(\omega_p)|^4 |\beta(\omega_s)\mathbf{E}(\omega_s)|^2 |\beta(\omega_{as})\mathbf{E}(\omega_{as})|^2 \tag{2.41}$$

This shows that the overall enhancement of CARS in presence of a nanoantenna is $\beta \approx |\beta(\omega_p)|^4 |\beta(\omega_s)|^2 |\beta(\omega_{as})|^2$. In a manner similar the one used to express the electromagnetic enhancement for SERS earlier, we can justify that

$$\beta(\omega_p) \approx \beta(\omega_s) \approx \beta(\omega_{as}) \tag{2.42}$$

This allows us to estimate the overall SE-CARS enhancement to be $\sim |\beta|^8$[20].

Now, we consider the coherent background from the nanoantenna's intrinsic $\chi^{(3)}$ response. This contribution can be included in order to write an expression for the total field at the far-field

$$\mathbf{E}_{total}(\mathbf{R}, \mathbf{r}, \omega_{as}) = \mathbf{E}_{antenna}(\mathbf{R}, \mathbf{r}, \omega_{as}) + \mathbf{E}_{molecule}(\mathbf{R}, \mathbf{r}, \omega_{as}) e^{i\Delta\phi(\omega_{as})} \tag{2.43}$$

Here, $\mathbf{E}_{antenna}$ is the independent contribution of the nanoantenna (usually metal), without considering the presence of any molecule. The phase term $e^{i\Delta\phi(\omega_{as})}$ is included in the expression to reflect the interference effects between the molecular and antenna contributions. While the contribution of the molecule ($\mathbf{E}_{molecule}$) in the total radiated field is also accomplished through the antenna, this radiation depends on the polarization of the molecule near the antenna which is strongly modified when they are coupled.

2.5.4 Heating of nanoantennas under ultrafast excitation

Photothermal heating of plasmonic nanoantennas occur due to the unavoidable energy transfer between the incident electromagnetic radiation and the antenna[20]. This effect becomes particularly pronounced and becomes a major issue when ultrafast irradiation is involved. Dephasing after the coherent excitation of surface plasmons at its resonance (ω_0) induces a transfer of energy between the incident optical field and the material. This dephasing is attributed to Landau damping, which is understood to be responsible for the transfer of quanta $\hbar\omega_0$ from the oscillation of surface plasmons to the metallic antenna[133, 134]. This is accomplished by exciting electron-hole pairs near the Fermi level E_F. Hot electrons are produced with maximum electron and hole energies of $E_e = E_F + \hbar\omega_0$ and $E_h = E_e - \hbar\omega_0$, respectively. The process happens on the order of a few tens of femtoseconds. After the generation of hot electrons, the energy is redistributed through inelastic electron-electron interactions and reaches a thermalized Fermi-Dirac distribution in the timescale of hundreds

of femtoseconds. Subsequently, the energy is transferred to the lattice through electron-phonon coupling in the 1-100 ps timescale. This results in the heating of the metal, followed by dissipation of this heat to the surrounding medium.

The thermal response of the nanoantenna under ultrafast irradiation has a dynamic nature and different antenna temperatures are expected for picosecond and femtosecond CARS experiments. As such, free-electron temperatures must be considered separately from the lattice and molecular temperatures. While the temporal evolution of this electron heating phenomenon is well-understood, it is more complicated and sometimes not possible to measure the spatial distribution of the temperature near the electromagnetic hotspot. One of the ways that we can measure this distribution is through observing the broad emission from the metal, known as the electronic Raman scattering (ERS). At ps time scales, we can gain useful insight about the Fermi-Dirac distribution of coupled electron-hole states, which can be estimated with the help of the Boltzman distribution for large spectral shifts [135, 20]. Through the analysis of the anti-Stokes scattered emission, it has been suggested that the temperature of the electron near the electromagnetic hotspot can reach thousands of Kelvin [6] in the ps time scales, as illustrated in Figure 2.12.

The discussion in the preceding paragraph provided insight into the thermal response of the electron gas near an electromagnetic hotspot. However, the heating kinetics of the molecule itself can be vastly different. Thermal equilibrium between the molecule and the antenna is understood to occur in few tens of picoseconds or longer timescales [136, 137]. When surface-enhanced coherent Raman scattering is considered, it is necessary to see if any transfer of energy takes place between the plasmonic junction and the molecule on the picosecond-femtosecond timescales. If such transfer occurs, it is possible that the temperature of the molecule can increase rapidly. One way to measure this temperature is to analyze the ratio of Stokes to anti-Stokes scattered signal. However, it is not trivial to independently measure the molecular temperature while avoiding other processes that contribute to up-pumping of

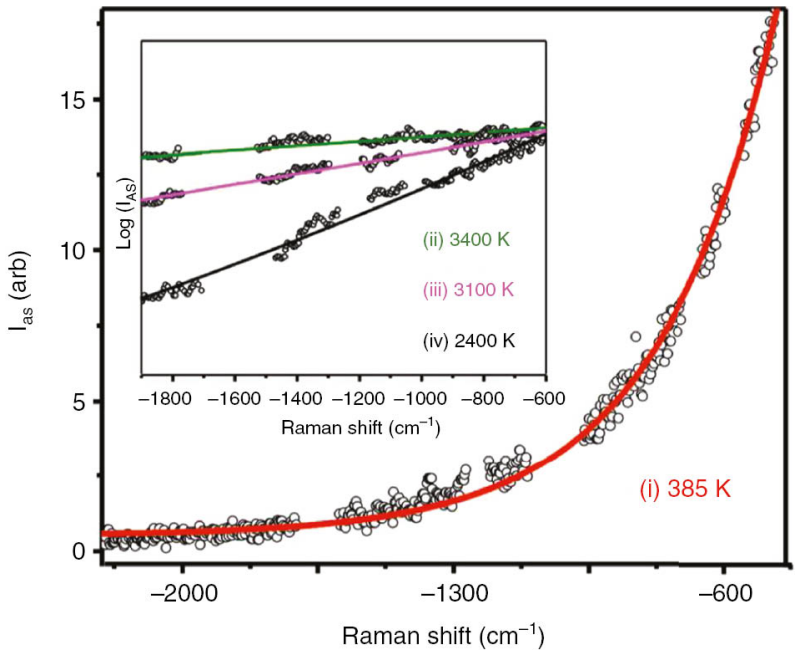

Figure 2.12: Temperature of electron gas measured near a gold nanodumb-bell antenna, probed through the electronic Raman scattering process. Curve (i) shows the anti-Stokes signal under 634 nm cw illumination using an average incident intensity of 30 μW/cm^2. (ii)-(iv) were taken under 6 ps, 785 nm illumination using an average incident intensity of 100 μW/cm^2. Reproduced with permission from [6].

the molecule's vibrational states ($\nu = 1$ and higher). Recently it has been suggested that the increase in molecular temperature (probed using the Stokes to anti-Stokes ratio) is not as drastic as in the case of electron temperature and this increase is relatively modest (< 100 K) under ultrafast excitation [138, 7]. Figure 2.13 shows the temperature of 4-nitrobenzenthiol attached to a Au nanoantenna under 1035 nm ~250 femtosecond excitation. The figure clearly shows that an increase in temperature happens on the picosecond timescale and subsequently decreases within a similar timescale. Due to this characteristic timescale which is also on the order of vibrational lifetime of the probed Raman-active modes, it is suggested that thermalized hot electrons near the plasmonic hotspot are responsible for this heating process. This data was obtained for peak powers of 10^7 W/cm^2. The experiments strongly suggest that the temperature of the molecule is dependent on the thermal response of the nanoantenna. However, $\Delta T_{molecule}$ is only a small fraction of $\Delta T_{electron}$. This observation indicates that the molecular temperature can be strongly affected by the heat capacity of

the surrounding medium and the notion is supported by studies in which the $\Delta T_{molecule}$ were found on the order of few hundreds of Kelvins under ultrafast irradiation, in which the plasmonic system was surrounded by low heat capacity shells made of silica [139].

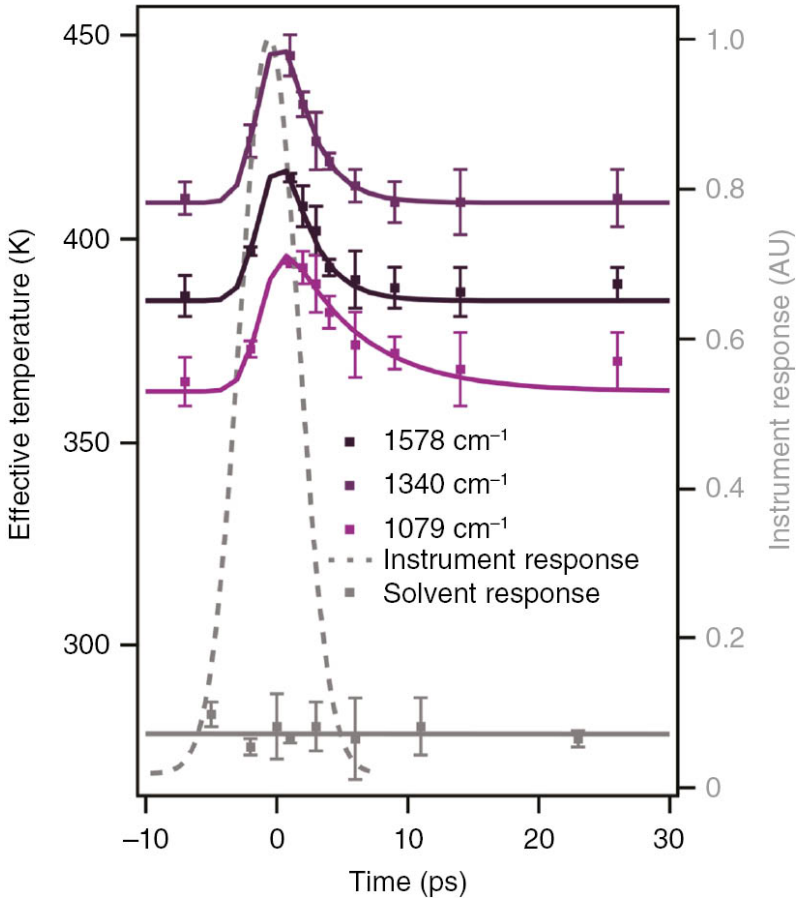

Figure 2.13: Temperature of 4-nitrobenzenthiol measured using Stokes-to-anti-Stokes ratio in an ultrafast SERS experiment. Reproduced with permission from [7]

The discussion in this section investigated the relative increase in temperature of electrons in the vicinity of the plasmonic hotspot and the molecule. However, additional effects become important under increased illumination dosages. It has been suggested that at peak field intensities ($\beta^2 I$) of 10^{12} W/cm^2 and above, direct ionization inside the molecule is expected to take place caused by the bending of atomic potentials and accompanying electron tunneling[140, 6]. These instantaneous effects do not depend on the temperature of the electron gas near the plasmonic hotspot. Experiments involving Au nanodumbbells under femtosecond irradiation ($\beta^2 I \approx 10^{13}$ W/cm^2) revealed photo-induced morphological changes

to the antenna [141]. This observation supports previous studies reporting arching and ionization effects in plasmonic structures in cw SERS measurements where $\beta^2 I$ reached $\sim 10^{13}$ W/cm^2.

Chapter 3

Sensing biomolecular interactions by the luminescence of a planar gold film

3.1 Rationale

Surface sensitive optical techniques are important for studying a wide range of biomolecular binding interactions. Fluorescence sensing, refractometric sensing and surface plasmon resonance (SPR) sensing are some of the most widely used detection strategies where selectivity is achieved solely based on optical contrast. Fluorescence based sensing methods utilize fluorescent probes to identify the analyte of interest [142]. It has found diverse applications in a variety of fields, including analytical chemistry, molecular biology, spectroscopy and microscopy to name a few [143, 144, 145, 146]. But its utility is limited by phototoxicity, photobleaching and, in some cases, the unavailability of suitable fluorescent probes. These limitations can be overcome by employing the intrinsic refractive properties of materials to generate optical contrast. A common approach to refractometric optical sensing is based on interferometry, where minute changes in refractive indices are measured as variations in

phase and amplitude of the applied light field [147, 148]. The phase changes facilitated by a single nanoparticle has been shown to be sufficient for producing detectable interferometric signals [149, 150, 151]. Nonetheless, an intrinsic limitation of interferometric sensors is a large background, which ultimately affects sensitivity and attainable spatial resolution.

Surface plasmon resonance (SPR) sensing is a refractometric sensing technology that provides enhanced detection sensitivity by utilizing surface plasmon polariton (SPP) modes supported by a metal film. The coupling of free space light to SPP modes is highly sensitive to minuscule changes in local refractive indices at the metal-dielectric interface [152, 153, 154]. SPR sensors do not require interferometric stability, and as such they are much simpler and robust compared to other refractometric sensors. The SPR method can be useful for extracting information on biomolecular interactions, chemical sensing as well as in theranostic applications. SPR sensors are currently the gold standard for studying the binding and dissociation kinetics of a wide range of biomolecules [153, 155, 156].

In the typical sensor implementation of SPR, binding/dissociation events are inherently ensemble averaged, and as a result information on individual binding/dissociation events cannot be easily retrieved. An imaging variant of SPR sensing, called surface plasmon resonance microscopy (SPRM), makes it possible to visualize individual binding/dissociation events with a camera. SPRM has been successful in dynamic imaging of a multitude of structures that are of biological interest, such as cells [33], bacteria [34], viruses [35], exosomes [36], DNA [37, 38], polymeric and protein nanoparticles [39] among others. Nevertheless, the SPRM technology suffers from a number of limitations including an inherently strong background and a non-ideal pointspread function (PSF) characterized by long-diffractive tails [35, 37, 157]. The wave-like PSF affects the spatial resolution of the SPRM approach compared to the confined, point-like PSF common to conventional optical imaging systems. Advances in image processing address these issues to some extent [158, 159, 36], but do not completely eliminate all of their inherent drawbacks.

To overcome some of the limitations of SPRM sensors, we recently developed a SPP-based sensor that makes use of an alternative optical signal [160]. Instead of monitoring small changes in the SPP-coupling angle or in the SPP interference pattern, this novel sensor uses the two-photon excited luminescence (TPEL) of the planar Au film as the sensing signal [161, 162, 118]. We demonstrated that the TPEL signal grows whenever a nanoscopic particle is within the nanoscale vicinity of the gold film, producing a localized emission source against a dark background that can be easily captured on a far-field camera. The PSF of the sensor is well-behaved and devoid of flares or long diffractive tails that plague conventional SPRM systems. We hypothesized that the signal originates from the field confinement introduced by the nanoscopic particle near the surface, giving rise to a higher probability of electron-hole pair generation in the gold layer, which, after electron-hole recombination, produces fluorescence-like radiation. Based on the suggested mechanism, we called this approach confined optical field enhanced fluorescence emission, or Cofefe for short.

Cofefe is a promising tool but this technology is still in its infancy and as such, there are questions that need to be answered in order to realize its full potential. Among these open questions are the need for evidence for the suggested signal mechanism, as well as proof that the Cofefe approach can be used reliably for kinetic studies of biomolecular interactions.

3.2 Methods and materials

3.2.1 Optical setup

A schematic of the optical setup is shown in Figure 3.1. A detailed description of the system has been given previously [160]. Briefly, the microscope uses a Ti:Sapphire light source (Mira 900, Coherent) with a center wavelength of 800 nm. The laser produces a 76 MHz pulse train of ∼180 fs pulses. The beam is conditioned to produce a linearly polarized and collimated

beam with a clean, transverse Gaussian profile of 10 mm diameter. The beam is then focused with a lens (f = 250 mm) onto the back focal plane of a 1.49 NA, oil immersion objective lens (Olympus), giving rise a collimated beam at the Kretschmann angle ($\sim 65^o$) to excite SPP modes at the gold/sample interface. The beam illuminates the sensor surface over a $\sim$100 μm diameter field of view (FOV). The ultrashort pulses generate two-photon excited luminescence upon binding of nano-particles at the gold film and the subsequent emission is collected in the epi-direction by the same objective lens. A 700 nm short wave pass dichroic mirror separates the signal from the incident beam. The signal is further filtered by a 625 nm$\pm$45 nm band pass filter and a 750 nm short wave pass filter. The filtered signal is subsequently projected onto an EM-CCD camera (iXon3, Andor) at a frame rate of 1 fps, unless otherwise noted. For the DNA binding experiments, the average illumination power before entering the objective lens ranged from 15 mW to 100 mW. Spectrally resolved measurements are performed by replacing the imaging EM-CCD camera is by a fiber-coupled spectrometer (Acton SpectraPro SP-2500, Princeton Instruments) equipped with a EM-CCD (ProEM 1600, Princeton Instruments).

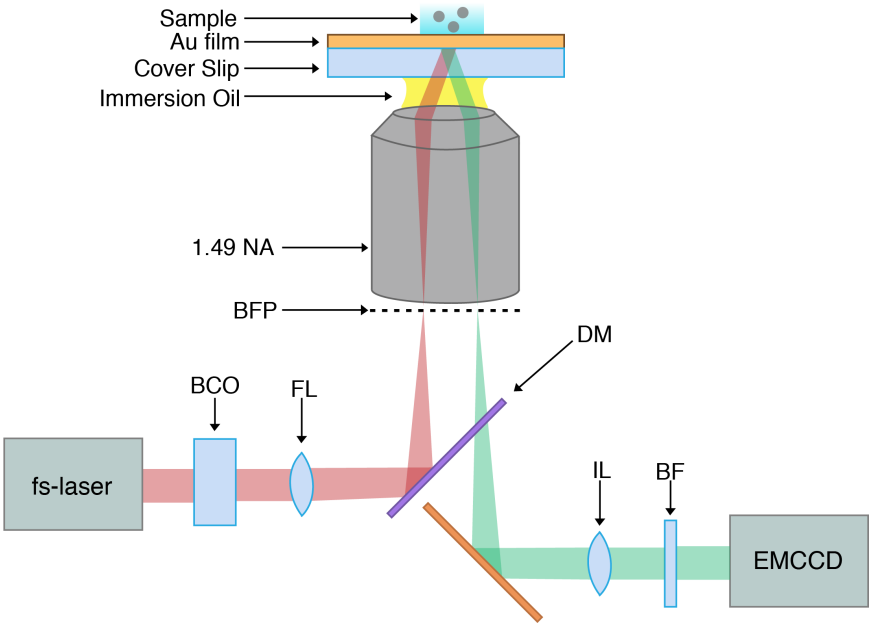

Figure 3.1: Schematic of the Cofefe microscope system. BF: bandpass filter; IL: imaging lens; DM: dichroic mirror; FL: focusing lens; BCO: beam conditioning optics; BFP: back focal plane; Obj: objective lens

3.2.2 Sample preparation

The sensor surface is prepared by thermally evaporating 30 nm Au on a BK7 borosilicate coverslip (VWR) using a 2 nm Cr adhesion layer. Before deposition of gold films, the coverslips are subjected to sonication in EtOH/Water and acetone/Water solutions. A mixture of sulfuric acid and Nochromix (VWR) is used to clean the glass surface without leaving any residues. For distance dependent field confinement experiments, atomic layer deposition (ALD) is used to deposit 2, 5 and 10 nm thick Al_2O_3 spacer layers over freshly prepared gold films. Suspensions of 30 nm silicon nanoparticles (Melorium Technologies) and gold nanoparticles (10, 40 and 100 nm; Sigma Aldrich) are used without further purification. Rhodamine 6G is obtained from Sigma Aldrich and prepared as a 20 μM aqueous solution.

Two different sequences of thiol modified DNA oligonucleotides, purchased from Integrated DNA Technologies (Coralville, Iowa), are used, namely 5'-S-S$(CH_2)_6T_{30}$-3' (called T_{30}) and 5'-S-S$(CH_2)_6A_{30}$-3' (called A_{30}). The gold coated surfaces are partitioned using silicon isola-

tion wells and exposed to 10 μL of 250 μM A_{30} oligonucleotides in a 1$\times$ phosphate buffered saline solution overnight. The T_{30} oligonucleotides are adhered to 40 nm gold spheres according to the procedure described by Hurst *et al* [163]. In our experiments, 150 pM AuNP is mixed with 5 μL of 1 mM T_{30} oligonucleotides. The DNA hybridization adsorption events are observed in the Cofefe microscope by bringing a suspension of T_{30} modified gold nanoparticles into contact with an A_{30}-modified gold film. Each binding event appears as an individual diffraction-limited bright spot against a dark background on the EM-CCD.

3.2.3 Image analysis

Recorded images are analyzed in ImageJ for manual counting of individual binding events, achieved by identifying clear bright spots with a signal-to-noise ratio of at least 10.

3.3 Results

3.3.1 Cofefe enables background-free particle detection

The main advantage of Cofefe over SPRM is that the former offers better image contrast, which can result in better detection sensitivity. Figure 3.2a shows a SPRM image of a single 100 nm Au particle. The characteristic diffractive tails extend the PSF over a wide area. Interference between the diffraction patterns of nearby particles can complicate particle localization. The corresponding Cofefe image is shown in Figure 3.2b. Several important differences can be observed. First, the Cofefe signal provides a positive bright signal against a dark background, thus enabling background-free detection. Second, the PSF is radially symmetric and does not exhibit diffractive tails. Third, the PSF is much more confined in space, making the registration of multiple particles within a certain region of interest more

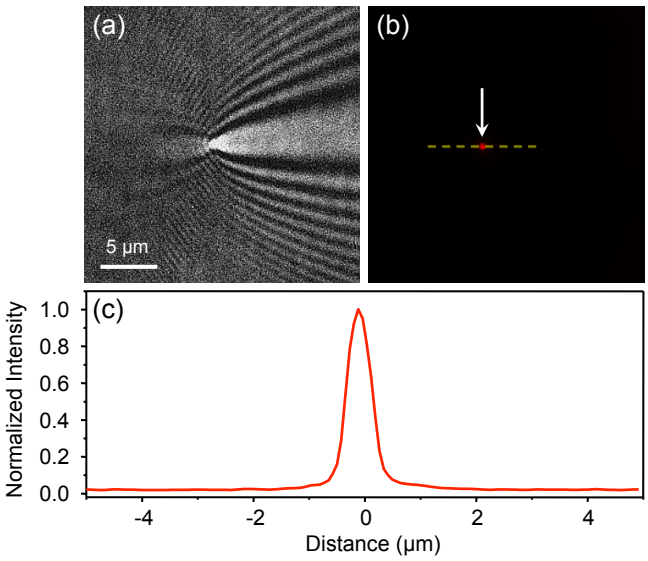

Figure 3.2: Comparison between SPRM and Cofefe imaging of an individual 100 nm Au particle. (a) SPRM image. (b) Cofefe image of the same particle. Arrow points to the particle. (c) Cross section taken at the dashed line shown in (b).

straightforward compared to the situation in SPRM. A one dimensional cross section of the PSF is given in Figure 3.2c, illustrating the positive signal relative to a low background. The signal to background ratio is more than 100 for all Au particles detected in the ensemble.

3.3.2 Cofefe is due to field confinement

In this Section, we examine the proposed mechanism of the Cofefe sensor, namely field confinement upon formation of a nanocavity between the target and the planar film, followed by two-photon excited electron-hole pair generation in the gold film. This mechanism has been suggested because strong luminescent signals were observed when non-fluorescent particles, such as silicon nanoparticles, polystyrene nanoparticles and lipid droplets, approached the Au surface [160]. Since it is unlikely that non-fluorescent particles produce strong luminescent signals, the Cofefe response has been attributed to excitations in the gold layer itself. Using femtosecond NIR pulses, the nonlinear response of gold has been ascribed in part to the interband excitation of d-band electrons to the sp conduction band [164]. Subse-

quent relaxation and radiative electron-hole recombination at the X and L symmetry points has been suggested as the origin of the observed broadband emission from nano-structured gold [161, 162, 118].

Here we wish to study whether the aforementioned confinement effect is responsible for the Cofefe optical signals. Since field confinement is a rapidly decaying function with increasing separation of the target from the planar surface, we surmise that the Cofefe signal show a steep decrease as the distance between the nanoparticle and the gold surface is increased. For this purpose, we prepare gold films with applied layers of alumina to control the target-surface distance on the nanometer scale. First, we examine the two-photon excited fluorescence signal of an aqueous Rhodamine 6G (R6G) solution as the thickness of the alumina layer is increased. The results are shown by the black squares in Figure 3.3. Because the sample lacks nano-particles, field confinement is absent and no luminescence from the gold is anticipated. Instead, the signal originates from the R6G fluorophores in the solution. On the bare gold, we expect that the SPP field induces a strong two-photon excited signal in the fluorescent R6G solution atop the Au surface. This is indeed observed. A similar result is obtained when a 2 nm alumina layer separates the gold film and fluorescent solution. In fact, no significant change in the signal strength is seen when the thickness of the alumina layer is increased to 10 nm. This indicates that the amplitude of the SPP field in the sample is not significantly affected by the presence of the alumina layer, a finding that corroborates observations made in studies on SPP enhanced emission of fluorophores [165].

Second, we study the sensor emission for an aqueous suspension of 40 nm-diameter gold nano-spheres. On bare gold, bright point-like spots are observed on the camera when the gold nano-particles adhere to the gold surface. The average strength of the signal, however, is somewhat weaker when the experiment is repeated with a 2 nm layer of alumina, even though the SPP coupling angle has been adjusted to maintain a similar coupling efficiency. Progressively weaker signals are observed when the layer thickness is increased to 5 nm and

10 nm, although the luminescent signal is still clearly visible. To investigate this trend, we perform Cofefe measurements of more than 20 adhered nano-particles and determine the average signal observed for a given thickness of the alumina layer. The results are plotted as the red circles in Figure 3.3, suggesting an exponential-like decay of the signal as the alumina layer thickness is increased. This observation provides evidence that field confinement is likely the origin of the enhanced luminescence signal upon particle binding to the surface.

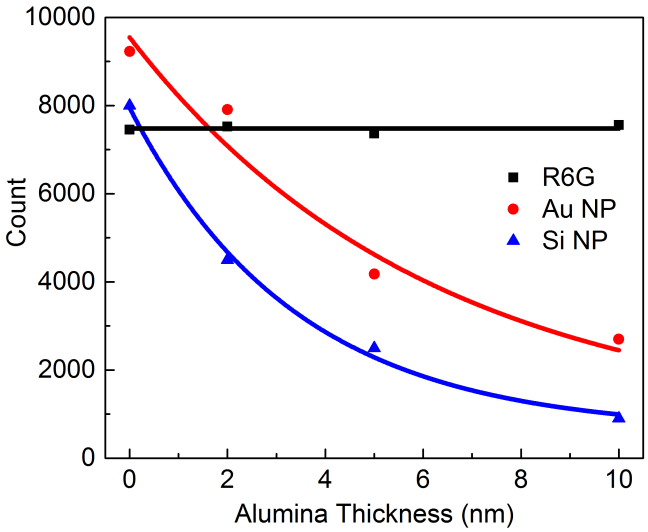

Figure 3.3: Signal strength of the sensor for various samples as a function of the thickness of an alumina layer atop the gold film. Black squares indicate a 20 μM aqueous solution of Rhodamine 6G, red circles denote the average signal obtained from adhered 40 nm gold nano-spheres, and blue triangles represent the average signal for 30 nm diameter Si nano-particles. Solid lines are linear (black) and curved (red, blue) splines to the data that serve as a guide to the eye. Note that the laser excitation power is scaled such that all samples produce approximately the same signal at zero thickness of the alumina layer.

Nonetheless, 40 nm gold nano-spheres are plasmonically active and display intrinsic luminescence due to the same mechanism of electron-hole pair generation in gold. Indeed, the average signal from gold particles appears to approach a non-zero constant value as the alumina layer thickness increases, an observation that can be attributed to the intrinsic TPEL of the gold nano-particle itself. Therefore, we have repeated the measurements with an aqueous suspension of 30 nm diameter Si nano-particles. Since solid Si does not exhibit a

strong TPEL signature, we may assume that the signal is solely due to excitations in the gold sensor layer through the proposed field confinement effect. The blue triangles in Figure 3.3 represent the average signal from adhered Si particles ($n > 20$) as a function of alumina thickness. The results show that the sensor emission for the Si sample decreases significantly as the alumina thickness grows. At 10 nm, the average signal closely approaches the noise floor, suggesting that for 10 nm gaps the field confinement effect has virtually disappeared. These combined results thus provide strong evidence that field confinement is an important aspect of the sensor's operating principle.

If the proposed mechanism is valid then the origin of the luminescence is in the local generation of electron-hole pair in the gold layer. This implies that the luminescence spectrum should resemble that of gold. It is known that TPEL of gold displays a broadband spectrum in the visible range with only limited features [118, 166, 167]. Figure 3.4 shows the spectral dependence of the sensor emission for the case when Si nano-particles are adhered to the gold surface. For this purpose, the emission intercepted from an area rich in nano-particles is coupled into a spectrometer. We observe a broad and feature-less spectrum that spans from 550 nm to 750 nm, and which closely resembles the luminescence spectrum of gold previously reported [118, 166, 167]. The luminescence signal of the bare gold film is shown by the black line in Figure 3.4, which exhibits a broadband profile that resembles the blue curve but is significantly weaker. This indicates that the field confinement-induced luminescence, enabled by the presence of the particles, is substantial. Taken together, these results support the suggested mechanism of the Cofefe sensor.

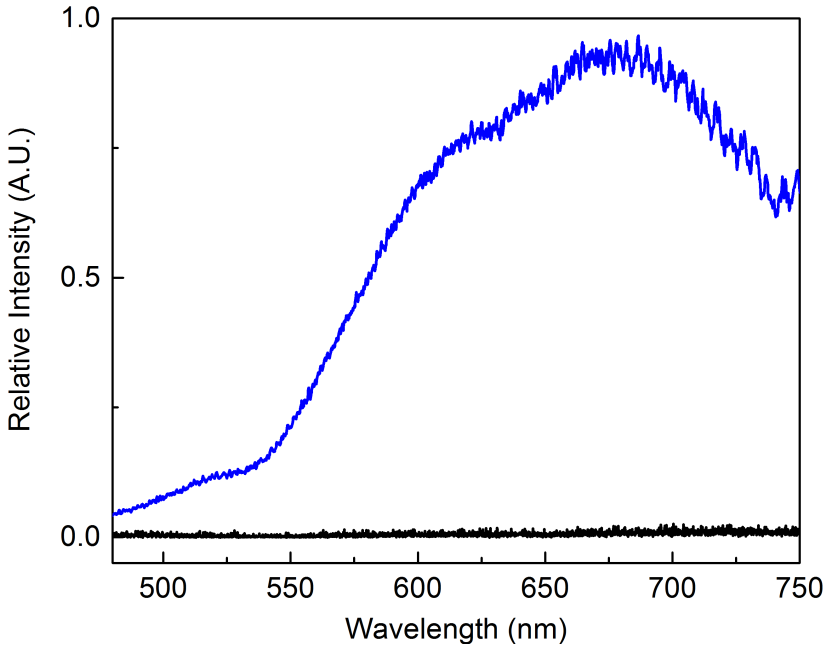

Figure 3.4: TPEL emission from the gold sensing surface observed from a bare film (black) and in the presence of adhered Si nanoparticles (blue).

3.3.3 Cofefe produces background-free images in binding assays

In contrast to traditional SPR sensors where the signal appears on top of a strong optical background, the Cofefe sensor produces a background-free signal. This feature enables registering of individual binding events with high sensitivity. In the following, we study the practical implementation of the Cofefe sensor for monitoring molecular binding events near the gold surface. For this purpose, we use a DNA binding assay that is based on the binding between T_{30} modified 40 nm gold nanoparticles (Figure 3.5a) and the gold surface functionalized with complementary A_{30} strands (Figure 3.5b).

Figure 3.5c depicts a representative Cofefe image where several modified gold particles have bound to the functionalized gold surface. Individual binding events show up as clean, sub-micron level, diffraction-limited spots on the camera. Each bright spot corresponds to a single binding event. Functionalized gold nanoparticles further enhance the detected signal because of their own localized surface plasmon resonances. When no particle is adsorbed on

the surface, the background signal is ∼100 counts/s, which is approximately the dark count rate for our camera. This dark count rate can go up to ∼400 counts/s for higher illumination powers. For individual binding events, an average signal-to-noise ratio (SNR) of more than 100 is achieved with illumination doses of ∼30mW before the objective lens for a 60 μm diameter spot on the sensor (10.6 μW/μm^2). The observed emission is stable and shows no blinking behavior. The excellent contrast thus achieved facilitates the analysis of binding events. In addition, in the limit of non-overlapping diffraction-limited spots, the method allows for multiple events to be detected simultaneously within the FOV.

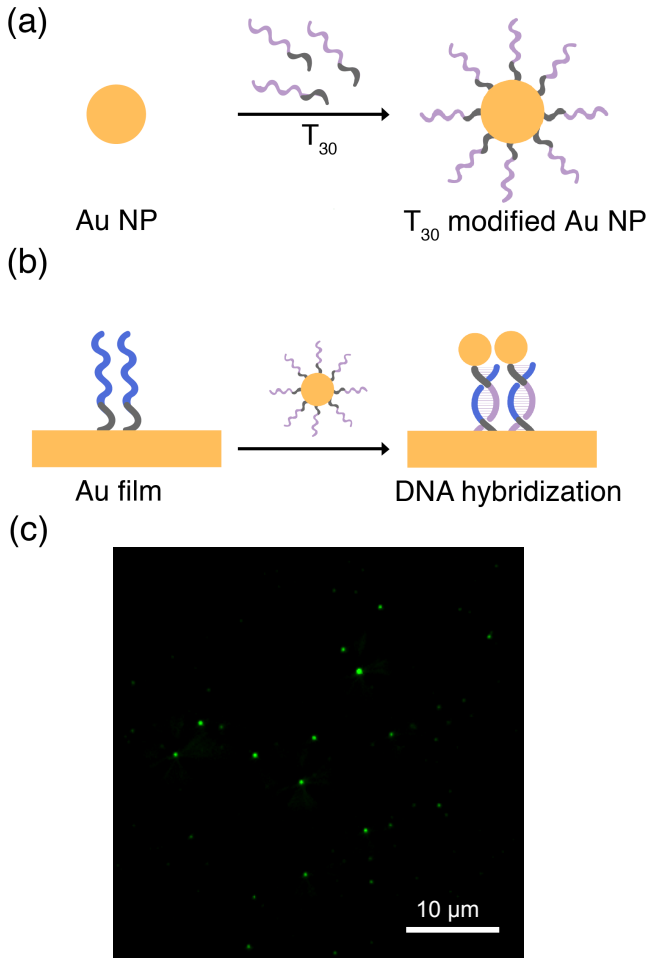

Figure 3.5: (a) Functionalization of 40 nm Au nanoparticles. (b) DNA hybridization. (c) Cofefe image of DNA hybridization events. Each bright green spot corresponds to the location of an Au NP bound to the functionalized gold surface.

We next examine the utility of the Cofefe sensor for dynamic binding studies. A freshly

prepared gold surface functionalized with single stranded DNA (A_{30}) is exposed to a suspension of gold nano-particles modified with single stranded DNA (T_{30}), and Cofefe images are collected over a time span of 15 minutes. The number of detected spots (binding events) is plotted as a function of time in Figure 3.6a for a nano-particle concentration in the 6 pM to 500 fM range. The binding curves show a characteristic behavior, exemplified by a rapid rise within the first two minutes and a decelerated rate of binding events thereafter. After 15 minutes, the highest number of binding events is seen for the highest concentration (6 pM), whereas the lowest number of events is obtained when the concentration is low (500 fM). When the experiment is repeated with nano-particles modified with non-complementary strands, no significant binding is observed. At a concentration of 6 pM, only 8 non-complementary binding events are recorded. This negligible amount of non-specific binding underlines the potential of the Cofefe sensor for application in many other bioaffinity assay applications. In Figure 3.6b, the number of binding events observed after 10 minutes is plotted as a function of concentration. An expected linear relationship is obtained, similar to results obtained previously in SPRM sensors [37].

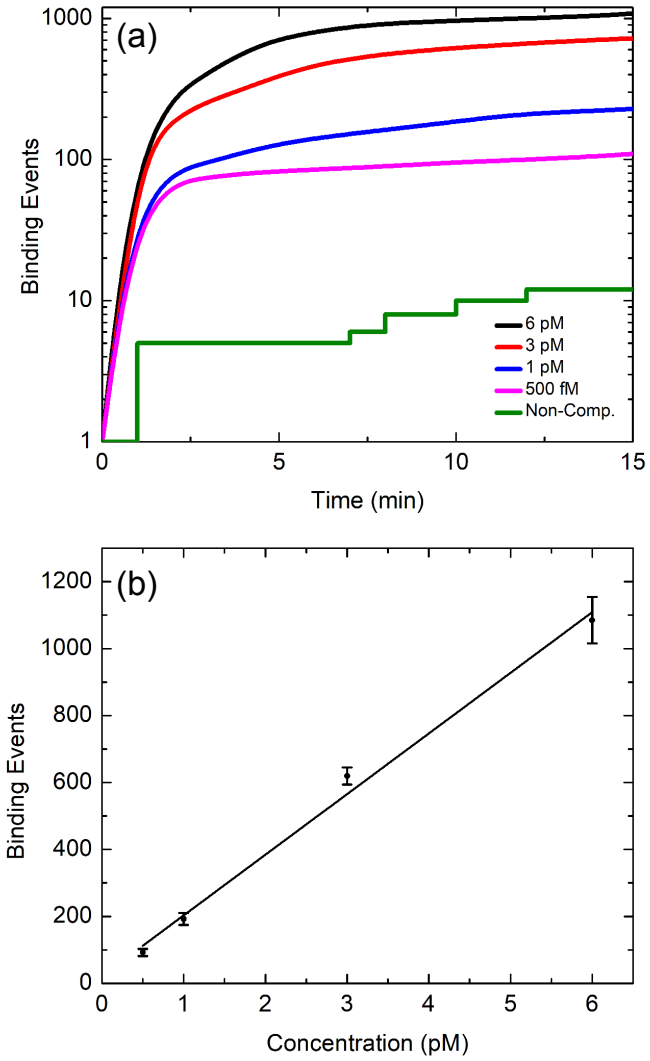

Figure 3.6: (a) Number of DNA-modified Au particles bound to the sensing surface as a function of time. (b) Number of binding events after 10 minutes as a function of particle concentration.

3.3.4 Resolution Enhancement with Super Resolution Radial Fluctuations

For particles sized below the diffraction limit of light, the detected spot on the camera reveals a clean radially symmetric pointspread function [160]. This suggests that localization analysis techniques that are used in fluorescence imaging could be implemented to improve the resolution of the Cofefe image [168, 169]. Enhancing the resolution is useful for increasing

the number of particles that can be detected within the field of view, thus enhancing the multiplexing capability of the sensor.

Super-resolution methods such as photo-activated localization microscopy (PALM) [170, 171] and stochastic optical reconstruction microscopy (STORM) [172] rely on the intermittent emission of fluorophores to localize spatial features. The Cofefe signal, on the other hand, originates from a nanoscopic volume in the gold layer and produces non-intermittent radiation. The Cofefe signal from nearby emitters is analogous to the high emitter density limit in conventional fluorescence microscopy, where the high density of emitters limits the ability of resolving blinking statistics in the presence of a high background. An alternative method, super-resolution radial fluctuations (SRRF) [173], is well suited to improve the spatial resolution in this high density limit. Assuming that the signal represents a collection of point emitters with a radially symmetric point spread function, SRRF can detect regions of higher local radial symmetry than their surroundings. By correlating radial symmetry maps from a sequence of raw images collected sequentially in time, SRRF provides a rapid evaluation of likely emitter positions.

Figure 3.7(a) shows a Cofefe image of 20 nm Au nano-particles deposited on the gold sensing surface. The green boxed area, shown enlarged in 3.7(b), highlights an individual particle. The apparent size of the point source is defined by the PSF, with a width that measures $\sim$0.4 μm [160]. To improve the resolution, we use the SRRF algorithm, based on 100 raw frames acquired at 68 fps. For comparison, the SRRF signal is overlaid on the Cofefe image acquired over the same interval of time. After application of the SRRF, the effective resolution is increased, producing a reduced full-width half maximum (FWHM) of $\sim$120–140 nm, as illustrated by the red profile in Fig. 3.7(d). Note that after application of the SRRF algorithm, the point source appears as a single lobe without additional fringes or flares.

Besides individual particles, brighter spots can be seen in Fig.3.7(a), suggesting that sev-

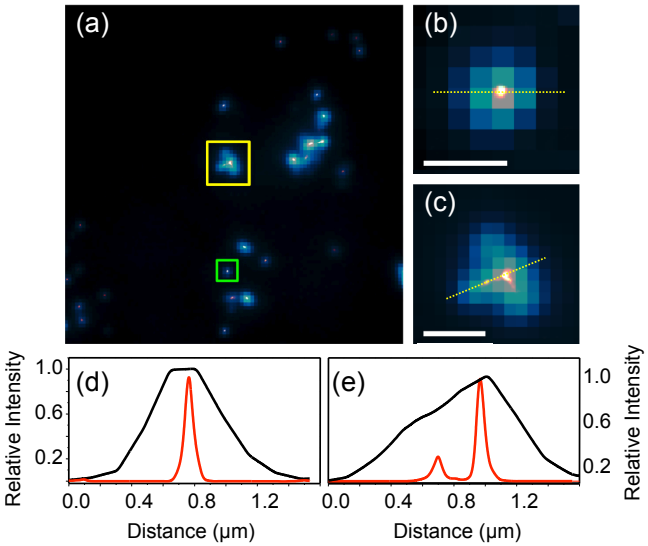

Figure 3.7: (a) Cofefe image of 20 nm gold particles (blue) overlaid with the SRRF enhanced image (bright orange). (b) Enlarged view of the green boxed area in (a), which contains a single 20 nm Au particle. (c) Enlarged view of the yellow boxed area in (a), which contains multiple particles within the diffraction limited volume. (d) Cross section taken at the dotted line in (b). Black line is the raw data and the red line is obtained after application of SRRF. (e) Cross section taken at the dotted line in (c). Black line is the raw data and the red line is obtained after application of SRRF. Scale bars are 1 μm.

eral particles may be found within the length scale defined by the diffraction limit. One of these areas is shown enlarged in Fig.3.7(c). Such spots are difficult to quantitatively analyze without additional resolution enhancement. With SRRF, the particles can be better discriminated in regions of high density, revealing that multiple particles can be found within the bright area of Fig. 3.7(c). The corresponding cross section shown in panel 3.7(e) shows the significant improvement in particle localization after application of SRRF. A single particle can be seen about 0.2 μm removed from the main cluster, a feature indiscernible without the use of super-resolution techniques. These results make clear that the Cofefe approach can be conveniently combined with super resolution techniques, further improving the analytical capabilities of the sensor.

3.4 Discussion

In this work, we have studied the mechanism of the Cofefe sensor and applied this new device to the study of DNA hybridization kinetics. As the Cofefe sensor produces images that are based on incoherent luminescence from the gold surface, it enables the detection of binding events as bright, non-interfering spots against a dark background. Our previous work has shown that Cofefe signals can be observed for both luminescent nano-particles (Au nano-spheres) and non-luminescent nano-particles (Si nano-structures and lipid droplets), suggesting that the optical signal might stem from the gold film rather than from the proximal nano-particles alone. These observations point to the role of field confinement in the nano-cavity formed between the planar surface and the nano-object. The experiments performed here confirm this notion. First, by adding an alumina spacer between the nano-particle and the gold film, the Cofefe signal is seen to decay in an exponential fashion. Such behavior can be expected if field confinement is responsible for inducing luminescence in the gold film. Second, the luminescence spectrum resembles that of nano-structured gold after two-photon excitation. In the absence of fluorescent nano-particles, this observation identifies the gold film as the origin of the luminescence. Hence, the suggested Cofefe mechanism implies that the gold sensing surface not only serves to provide the SPP illumination field, it also constitutes the material responsible for the generation of radiation. Gold is known to exhibit a strong nonlinear optical response in the presence of surface plasmon excitations [174, 175], which corroborates our findings here. The ability of the Au film to produce light of a color different from the illuminating light makes Cofefe a very attractive sensing mechanism that goes much beyond what conventional SPR sensors can offer.

The DNA binding measurements discussed in this work yield binding curves that closely resemble SPRM studies of the same DNA binding assay [37], providing evidence that the Cofefe sensor can be used for reliable quantitative biomolecular binding studies. In addition, we have observed high specific to non-specific binding ratios (more than 100:1), which should

potentially translate to widespread application in bioaffinity assays where analytes may be present at low concentrations.

While the Cofefe sensor reproduces previous SPRM results in terms of binding kinetics, it does so with a PSF that is intrinsically point-like against a low background. The application of localization-based algorithms for improving the resolution is a clear advantage of the Cofefe approach. The SRRF algorithm used in this work is particularly well suited for Cofefe images, improving the resolution of individual particles to the 120–140 nm range. Compared to PSF reconstruction techniques in SPRM [159, 36], the processed images in Cofefe enable a clean and point-like localization of particles, which differs from the reconstructed PSF in SPRM in that it is free from remaining fringes or flares. Ultimately, the fringe-free localization makes it possible to identify individual particles at higher densities, which is an attractive capability for sensing at higher concentrations.

Although the current sensor already enables practical bio-affinity studies, there are several steps that can be taken to improve the performance of the device. For instance, using an optimized optical imaging system, it is relatively straightforward to increase the FOV, which is currently 100×100 μm^2. By expanding the FOV to 250×250 μm^2 more binding events can be observed without significant undersampling of the data, thus improving the statistical sampling of binding event. In addition, tailored dichroic mirrors and bandpass filters can be implemented to ensure maximum transmission of the Cofefe signal, resulting in stronger signals and thus faster and more reliable sensing. Finally, template-stripping can be used to produce ultra-flat gold films, with a surface roughness of less than 5 Ångstrom, using mica as template. As the quality of the gold film is a key factor in the signal-to-background ratio of the Cofefe signal, optimizing the film quality will undoubtedly enhance the sensitivity of the sensor.

3.5 Conclusion

We have shown that optical field confinement plays a key role in signal generation process of the Cofefe sensor. This mechanism stipulates that Cofefe is suitable for detection of non-fluorescent particles, a notion that offers opportunities for monitoring nanoscopic objects of biological significance. The utility of the Cofefe sensor is underlined by the successful DNA binding measurements through hybridization on the gold sensing surface, as presented in this work. These studies emphasize that Cofefe is a promising new tool in the field of particle sensing. It takes advantage of some of the conveniences of SPRM microscopy, but at the same time eliminates the fundamental problem of a bright background and low spatial resolution that plagues it. As the Cofefe technology is still in its infancy, there is room for improvement of the sensor. Through optimization of the sensing area, detection optics and the use of smoother gold films, we believe that detection of viruses, bacteria, exosomes, liposomes and, ultimately, single protein structures are within reach.

Chapter 4

Surface-enhanced coherent anti-Stokes Raman scattering of molecules near metal-dielectric nanojunctions

4.1 Rationale

Surface enhanced Ramans scattering (SERS) is a widely used spectroscopic tool for sensing molecules at low concentrations. In SERS, plasmonic nano-antenna systems enhance the sensitivity of the otherwise weak Raman effect [176, 20, 177]. These metallic nanostructures support surface plasmon resonances that can confine propagating electromagnetic radiation to nanoscale regions, where the molecule of interest is efficiently driven. Subsequently, the antenna enhances the radiation of the induced Raman polarization, enabling strong signal collection in the far-field [178, 179, 180, 181, 182]. The enhancement mechanism of SERS is well understood, and well-designed nanostructures have successfully pushed the sensitivity of this technique to the single-molecule limit [46, 183, 184]. While SERS does allow massive

enhancement of the feeble Raman effect, it is limited in terms of acquisition rates and struggles to record spectra at rates faster than $\sim$ 10 Hz in the single molecule limit. For single molecule applications that require much faster readout rates, such as DNA sequencing applications [185, 19], the SERS mechanism alone may not be sufficient.

In coherent Raman scattering (CRS) the vibrational transition in the molecule is stimulated, and thus the molecular transition rate can be significantly higher compared to the transition rate in spontaneous Raman scattering. In addition, in the case of an ensemble of molecules, the molecular oscillators are driven in unison, producing coherent radiation that takes advantage of the constructive interference between the dipolar radiators. The combination of these two effects can give rise to much higher signal levels in CRS compared to linear Raman methods. For this reason, CRS spectroscopy and microscopy techniques have gained popularity in applications where the long signal acquisition time of spontaneous Raman scattering is a limiting factor [186, 187, 188, 189, 127, 190]. Various CRS implementations have demonstrated spectral acquisition rates that are many orders of magnitude faster than what can be achieved with spontaneous Raman or SERS. Examples include Fourier transform coherent anti-Stokes Raman scattering (CARS) with spectral acquisition rates of 100 kHz [191, 192] and arrayed detection of stimulated Raman scattering (SRS) at spectral acquisition rates of 200 kHz [193].

Such fast spectral acquisition rates, however, were obtained for relatively high molecular concentrations, and are thus not easily extended to the limit of a few molecules. In this limit, the coherent amplification of the CRS signal no longer applies [189], yet the stimulated vibrational transition afforded by the CRS process still offers a potential mechanism for enhanced transition rates relative to spontaneous Raman scattering. In this context, the combination of CRS with the field enhancement provided by surface plasmon resonances appears a route toward higher Raman radiation rates than those obtained in conventional SERS.

Surface-enhanced CRS was first demonstrated in the form of surface-enhanced CARS (SE-CARS) in 1979, using the propagating surface plasmon polariton (SPP) modes supported on a flat silver film to amplify the CARS spectrum of liquid benzene [194]. Subsequent work has focused predominantly on plasmonic junctions in gold and silver nano-structures, confirming the ability of plasmonic resonances to amplify the CRS signal, even reaching the single-molecule limit [195, 121, 131, 177]. These metallic systems are chosen as they feature some of the highest achievable field-enhancement factors. However, there is a limit to how much incident radiation can be applied before photo-induced breakdown of the plasmonic substrate and the molecule occurs [137, 196, 136, 197, 133, 134, 198, 135, 6]. It has been shown that under ultrafast excitation, the electron temperature can reach thousands of Kelvin [141], and that also the lattice temperature can go up, affecting the structural integrity of the junction. It has also been reported that near the local peak intensities (defined as $\beta^2 I$, where β is the local field enhancement factor and I is the incident intensity) of $10^{12} - 10^{13}$ W/cm^2, bending of the potential followed by electron tunneling can cause photo-induced ionization of the molecule [140]. The heat-induced morphological distortions at the metallic junctions are accompanied by steep field gradients that defy standard Raman selection rules, and involvement of charge-transfer plasmons and plasmon-induced chemistry complicate matters, making these SE-CRS measurements extremely difficult to reproduce [20]. As a result, there is a need for new SE-CRS systems that enable reliable and reproducible measurements by substantially minimizing the inherent drawbacks of the metal-molecule-metal nanojunctions used for SE-CRS thus far.

Addressing this issue of reproducibility of SE-CRS measurements requires a reimagining of experimental geometries. Plasmonic systems that are easy to fabricate repeatably and that can efficiently produce a robust optical response with lower local heating can play an important role here. A case in point is the use of a flat gold film on a glass substrate as the main antenna system. We have previously shown that such a system provides reproducible total enhancement factors of $\sim 10^6$ for the case of SE-CARS [24, 25]. Even higher enhancement

factors can be expected for nanoantenna systems comprised of metal particles placed on top of a metal film. This particle-on-a-film configuration has been explored by multiple groups as a promising platform for reproducible (linear) spectroscopic studies [199, 200, 201, 202, 203]. Facile fabrication methods and high attainable field enhancement factors make this system particularly suitable for SERS studies.

While this particle-on-a-film geometry substantially mitigates heating issues, the thermal load at the junction can be further reduced by using high-index dielectric particles that are known to exhibit higher specific heat capacities while also showing excellent antenna properties. It has been recognized that Si and GaP dielectric particles provide strong field enhancements at optical and NIR frequencies while producing orders-of-magnitude lower dissipative losses compared similar structures made of gold [4, 5]. The mechanism behind metallic and dielectric nanoantenna induced field enhancement processes are fundamentally different. The metal induced plasmonic fields are generated as a result of free-electron plasma oscillations [15]. In dielectric nanoantennas, electromagnetic field localization arises due to the generation of strong displacement currents inside the material. These currents generate inner-electric field distributions, which are accompanied by electric fields outside the material as well. As a result, when dieletric particles form nanojunctions, they also provide field enhancement in the cavity [17, 4]. These high-index dielectric nanoparticles provide a low-loss alternative to their metallic counterparts, which we explore in this study as a potential platform for reliable surface-enhanced CRS sensing.

In this work, we seek to overcome the aforementioned inherent limitations of unpredictable SE-CARS enhancement systems. We utilize a simple experimental geometry to perform repeatable and controllable wide-field SE-CARS measurements at Au film-Au particle and Au Film-Si particle nanojunctions. We demonstrate successful generation of detectable SE-CARS signals using the lowest reported average incident intensities to date using a metal-molecule-metal nanojunctions. We also successfully perform a first-of-its-kind SE-CARS

measurements at the metal-dielectric heterojunction, opening up the possibility of next generation of surface-enhanced coherent Raman sensors that do not rely on fragile metallic nano cavities.

4.2 Methods and materials

4.2.1 Sample preparation

Gold sensing surfaces are prepared using a physical vapor deposition (PVD) process. A 45 nm thick Au film on top of a 2 nm thick Cr adhesion layer is evaporated on BK7 coverslips (Corning). Note that this Cr layer introduces attenuation of the surface plasmon wave as a result of the poor (nonmetallic) optical properties of Cr at near-infrared wavelengths, yet it is used here to enable better adhesion of the gold to the glass coverslip. The coverslips are thoroughly cleaned prior to deposition by sonicating them in EtOH/water and acetone/water baths. Freshly prepared gold films are functionalized by overnight incubation in 5 mM ethanolic solution of 4-(mercaptomethyl)benzonitrile (MMBN) obtained from Sigma-Aldrich. 40 nm gold nanoparticles (Sigma-Aldrich) and 60 nm Silicon nanoparticles (Meliorum Technologies) are used without further purification. The particles are drop cast on functionalized films prior to measurements. Scanning electron measurements reveal that the drop-casting procedure results in the formation of small isolated clusters of 1-10 nanoparticles on the gold surface.

4.2.2 Optical setup

The optical setup is based on an inverted Olympus IX73 microscope frame. The system uses a light source that consists of a source laser and a synchronously-pumped optical parametric

oscillator (OPO). The source laser is a Nd:Vanadate oscillator (Pico-Train, High-Q) producing ∼7 ps pulses at a center wavelength of 1064 nm and is used as the Stokes beam for the SE-CARS measurements. Figure 4.1 provides a schematic of the optical layout.

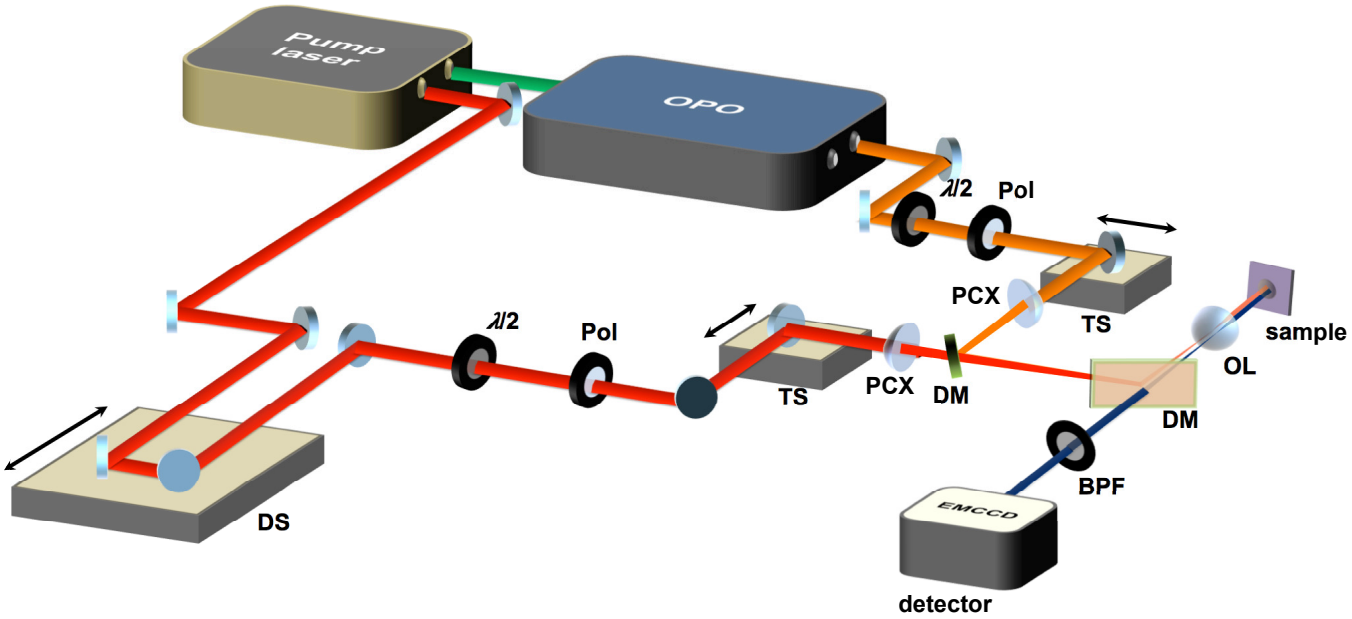

Figure 4.1: Schematic of the wide-field SE-CARS microscope system.DS, delay stage; $\lambda/2$, half-wave plate; PL, linear polarizer; TS, translation stage; PCX, plano-convex lens; DM, dichroic mirror; OL, 1.49 NA objective lens; BPF, bandpass filter.

A portion of this beam is frequency-doubled and then used to synchronously pump the OPO (Levante Emerald, APE Berlin) to generate a tunable (720 - 980 nm) pump beam. Both the pump and Stokes beams are conditioned to produce linearly polarized and collimated beams with clean, transverse Gaussian profiles. The spatially and temporally overlapped beams are then separately focused with plano-convex lenses (f = 250 mm) onto the backfocal plane (BFP) of a 60×, 1.49 NA (APON60XOTIRF, Olympus) objective lens, producing collimated beams at the exit pupil of the objective lens for wide-field illumination of the sample. The beams are incident at their respective Kretschmann angles to excite SPP modes at the gold/nanoparticle interface. After interacting with the target molecule, the anti-Stokes scattered radiation is generated and the epi-directed signal is separated from the incident fields by a dichroic mirror (850 nm SWP, Semrock) and projected onto an EM-CCD camera (iXon3, Andor) after going through two bandpass filters (794/32 nm,

Semrock). The expanded beams produce a field of view (FOV) of 105×105 μm^2. For the SE-CARS measurements at Au film-Au particle nanojunctions, the average incident powers at the sample in both beams are kept low (5-10 mW in pump and 5-15 mW in Stokes) to avoid saturation of the EM-CCD with two-photon excited fluorescence (TPEL) and the images were collected at 1 second/frame. These power levels correspond to power densities of $0.64-1.27$ μW/μm^2 for the pump and $0.64-1.91$ μW/μm^2 for the Stokes beam in the sample plane. In the Au film-Si particle heterojunctions, the field enhancements are lower compared to Au-Au nanojunctions. This necessitates higher power levels (up to 140 mW of average power in each beam or 17.92 μW/μm^2) and longer integration times (30 seconds/frame).

4.2.3 Numerical simulations

Numerical simulations of the local electromagnetic fields are performed using the finite-difference time-domain (FDTD) method (Ansys Lumerical FDTD). The Palik library is used for dielectric function estimation for all the materials involved [204]. The 2 nm Cr layer is ignored in the simulations. For a given sample, an incidence angle sweep is performed to find the Kretschmann angle for efficient excitation of propagating surface-plasmon polariton modes. Using the maximum coupling angle, subsequent simulations are performed to calculate electromagnetic fields at the vicinity of the nanojunction. Fine meshing of 0.167 nm is used in all cases. Experimental values for the thickness of the film, diameter of the particles and the cavity length are used for these calculations.

4.3 Results

4.3.1 SE-CARS at Au film-Au particle nanojunction

We use a high numerical aperture microscope objective-based Kretschmann configuration to individually couple the freely propagating pump and Stokes beams to the SPP modes supported on the planar gold film. The SPP coupling angles for each of the beams can be found by monitoring the back-reflection from the film on the detector. Equivalently, TPEL from the gold film can be monitored to find this angle [205]. This luminescent background is attributed to the interband transitions in the gold film and the subsequent radiative recombination of electron-hole pairs.[162]

We first perform SE-CARS measurements on a Au particle-Au film nanoantenna system in the wide-field Kretschmann configuration. Our target is 4-(mercaptomethyl)benzonitrile (MMBN), which is present as a monolayer on the surface of the gold film. A 40 nm diameter gold particle is placed atop the molecular layer, as shown schematically in Figure 4.2(a). Using finite-difference time-domain (FDTD) calculations for this experimental configuration, we find that the combined effect of propagating SPPs from the gold film and the LSPR of the gold particles results in an effective field enhancement factor β_p of 108 at a pump wavelength of 909 nm. Similarly, we find $\beta_s = 96$ at the Stokes wavelength ($\lambda_s = 1064$ nm) and $\beta_{as} = 117$ for the anti-Stokes wavelength ($\lambda_{as} = 793$ nm). Figure 4.2(b) shows the hotspot formed between the particle and the gold film under SPP illumination conditions. The hotspot size is found to be $\sim$5 nm in diameter. Using a surface coverage of 6 molecules/nm^2 [206, 207, 208], we estimate that there are $\sim$120 molecules in each electromagnetic hotspot under these conditions.

In the experiment, the average incident powers of both beams are kept low (5-10 mW in pump and 5-15 mW in Stokes) to avoid saturation of the EM-CCD with TPEL. With the resulting

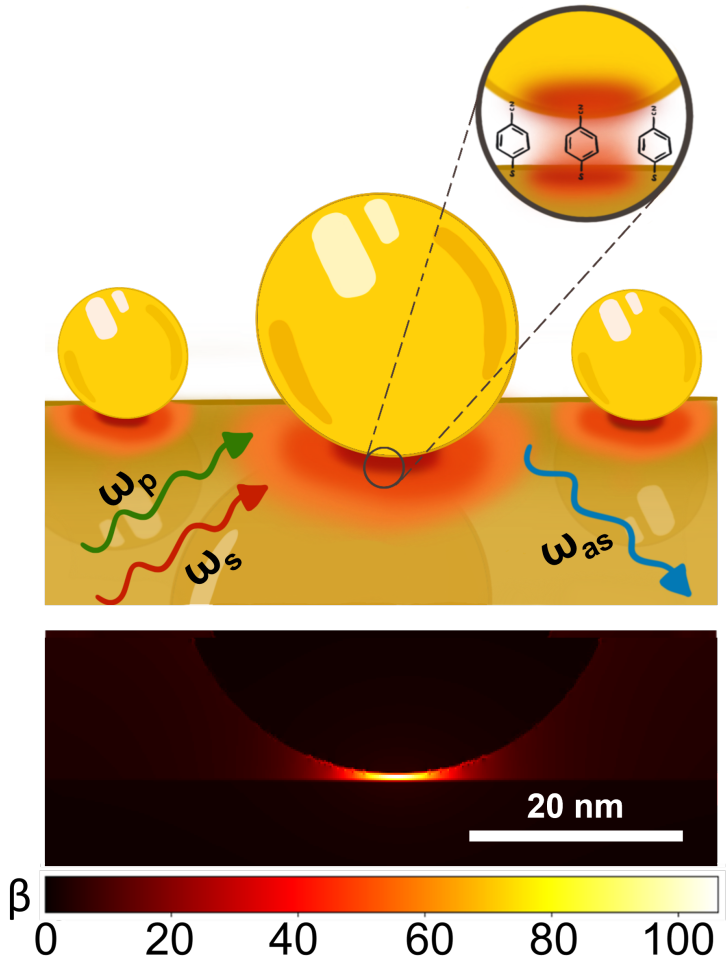

Figure 4.2: (a) Schematic of our experimental geometry for SE-CARS at Au film-Au particle nanojunction. (b) FDTD simulation near the junction under 909 nm illumination in the Kretschmann configuration.

power densities in the 1 μW/μm^2 range, these average excitation intensities to generate a detectable CARS signal are lower than reported in previous studies. The TPEL background is generated by the pump beam and can be independently determined by blocking the Stokes beam. In the following, we subtract the TPEL background signal to isolate the SE-CARS signal.

Figure 4.3 shows the SERS spectrum of the Au-MMBN-Au structure near the 1604 cm^{-1} resonance of the aromatic ring vibration. The Figure also shows two wide-field SE-CARS

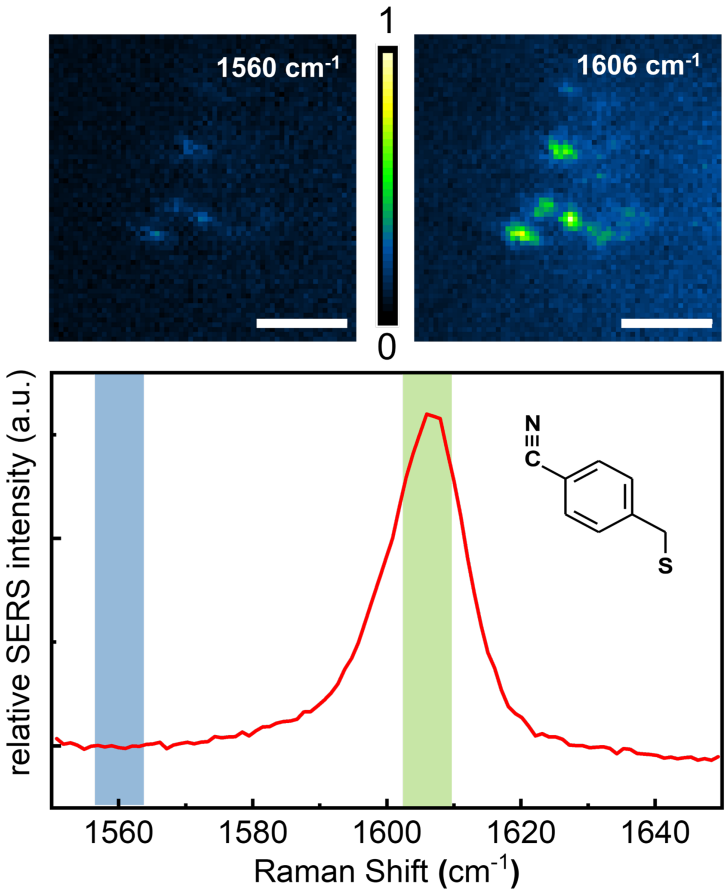

Figure 4.3: SE-CARS images of MMBN molecules located in a Au film-Au particle nanojunction. On-resonance images were taken at 1606 cm^{-1} and off-resonance images were taken at 1560 cm^{-1}, as shown in the SERS spectrum of MMBN immobilized on a 40 nm gold nanoparticle. Scale bar is 2 μm.

images, taken at an off-resonance energy of 1560 cm^{-1} and at the on-resonance energy of 1606 cm^{-1}. The image shows small clusters of gold nanoparticles on the Au film. The difference between the on and off-resonant settings is evident and repeatable, and is attributed to the vibrational resonant excitation of MMBN. For the particular image shown in Figure 4.3, we observe molecular signal levels of ~160 photons/s. We note that $\beta^2 I$ in this case is 2.83×10^9 W/cm^2, which is at least 3 orders of magnitude smaller than the photodamage threshold of gold. From this, we can infer that in principle higher effective local peak intensity can be applied to generate more SE-CARS signal. While the "hot" cavity does enable strong light-matter interactions, TPEL (~1850 photons/s as shown in Figure

4.3) from the film and the plasmonic gold nanoparticles establish a limit on the allowable incident power levels. After TPEL subtraction, the background visible in the off-resonant image at 1560 cm^{-1} can be attributed to the coherent four-wave mixing (FWM) background from the gold nanojunction. The electronic FWM background in this case is on average $\sim$13% relative to the molecular vibrational signal.

Under the current excitation conditions, the SE-CARS signal is clearly observed, yet the signal shows variation over time. Blinking-type behavior can be observed for several hotspots on the 1-100 s timescales. In addition, the magnitude of the SE-CARS signal gradually decays on a timescale of $\sim$ 3 minutes under constant illumination. We attribute these observations to thermal effects at the Au-Au junction. These observations have motivated us to explore metal film-dielectric particle heterojunctions that are less susceptible to thermal effects and that exhibit lower metal-induced TPEL.

4.3.2 SE-CARS at Au film-Si particle heterojunction

Next, we examine the capability of heterojunctions consisting of a metallic gold film and dielectric silicon nanoparticle to generate vibrationally resonant SE-CARS signal from the MMBN molecule. Electromagnetic field calculations (FDTD) provides insight into how the particle size and coupling angles for the pump, Stokes and anti-Stokes frequencies affect the overall CARS enhancement factor. Figure 4.4 demonstrates that the coupling angle changes more dramatically for the anti-Stokes radiation compared to the longer wavelength pump and Stokes beams.

While the Kretschmann angle changes rapidly for the shorter wavelengths, the simulations show that they have little impact on the attainable overall CARS enhancement factors. Figure 4.5(a) shows numerically calculated enhanced local fields in the vicinity of the Au film-Si particle junction. For a heterojunction consisting of a 45 nm Au film and a 60 nm

Si nanoparticle, we calculate a moderately high β_p of ∼35 at the pump wavelength of 909 nm. Similar calculations were performed for the Stokes and anti-Stokes wavelengths. Given that SE-CARS signal scales as $\beta_p^4\beta_s^2\beta_{as}^2$, we expect the local fields to be strong enough to generate vibrational response from the aromatic ring mode even with the low illuminating power densities that are being used in our wide-field SE-CARS microscope. As shown Figure 4.5(b), the overall CARS enhancement factor is predicted to remain near 10^{12} for the particle sizes studied here.

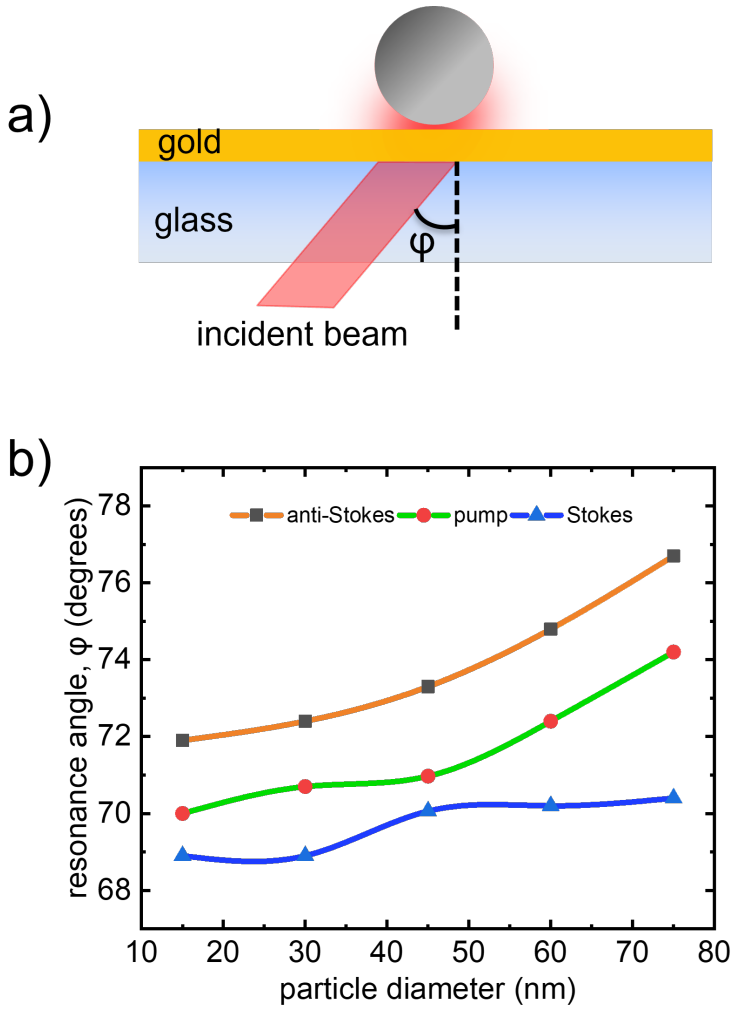

Figure 4.4: a) Cartoon of the incoming beam arriving at the Kretschmann angle (φ) at the Au film-Si particle hereojunction b) Kretschmann angles for pump, Stokes and anti-Stokes wavelengths for different diameters of silicon nanoparticles. The lines connecting the data points are used here as visual guides only. No fitting is performed on these data

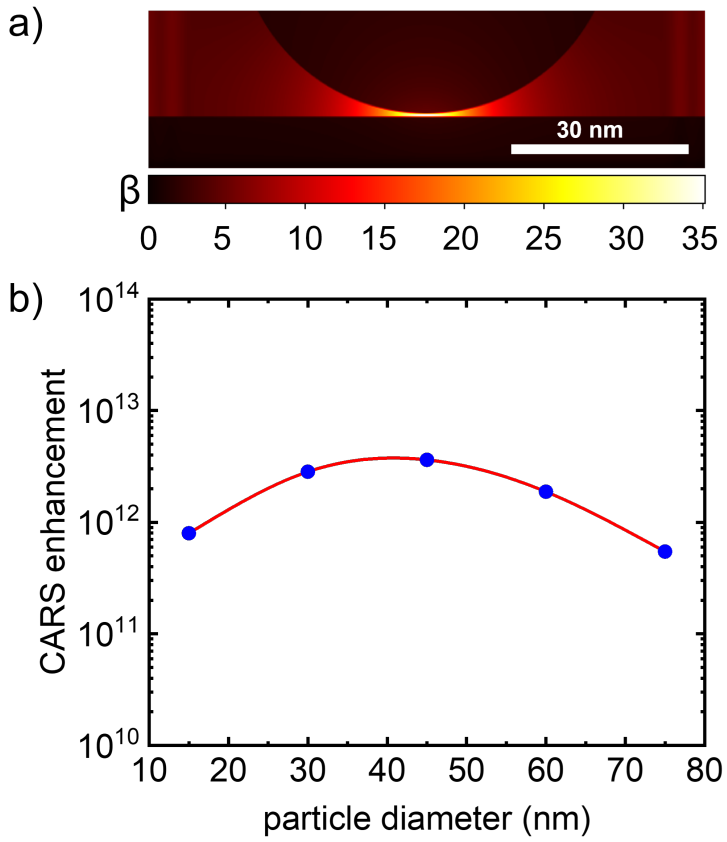

Figure 4.5: a) FDTD calculations for locally enhanced fields near the Au film-Si particle heterojunction at the pump wavelength of 909 nm. Particle has a diameter of 60 nm. b) Overall SE-CARS enhancement ($\beta_p^4\beta_s^2\beta_{as}^2$) factor as a function of Si nanoparticle diameter

In the heteorjunction experiments, the average power in each of the incident beams is varied between 100-140 mW, corresponding to intensities of 12.8-17.92 μW/μm^2. Further increase of illumination dosage is not feasible as they have been observed to result in photo-induced thermal damage to the Au film itself. Given that the lateral size of the field distribution is approximately the same as in the case for Au-Au junction, we estimate that a similar number of molecules ($\sim$120) are being probed for each film-particle hotspot.

Figure 4.6 shows the wide-field SE-CARS spectrum (green dots) in the 1560-1630 cm^{-1} window. The SE-CARS data is overlaid on top of the CARS spectrum of the bulk MMBN (blue trace) that is shown as reference. Unlike the wide-field SE-CARS measurements, the CARS spectrum of bulk MMBN is obtained using tightly focused beams produced by a 1.49 NA

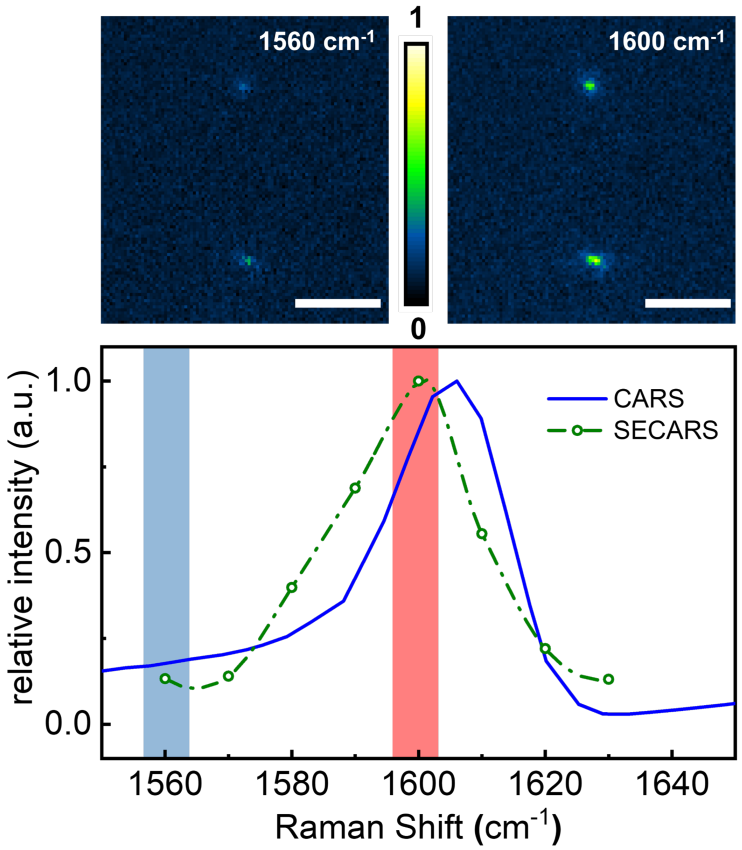

Figure 4.6: SE-CARS spectrum of MMBN located inside Au film-Si particle heterojunction. The green dots show SE-CARS data points taken at 10 cm^{-1} intervals. The CARS spectrum of bulk MMBN is shown as the blue trace as reference. Above the spectrum, representative on and off-resonance images are shown. Scale bar is 5 μm.

microscope objective. The SE-CARS measurements are taken at 10 cm^{-1} steps with the 1604 cm^{-1} resonance as the vibrational mode of interest. We observe a spectral SE-CARS profile that roughly resembles the CARS spectrum of bulk MMBN. The spectral dependence provides strong evidence that the SE-CARS signal from the Si-Au junction resolves the vibrationally resonant response of MMBN. The SE-CARS images show clear contrast between on and off resonant settings. The molecular SE-CARS signal in this experiment is found as ~235 photons/s (as shown in Figure 4.6). We observe TPEL background from the Au film in this configuration as well. However, due to the non-luminescent and non-plasmonic nature of the Si nanoparticles, this background signal does not overwhelm the far-field detector. The TPEL background (~550 photons/s as shown in Figure 4.6) is subtracted to obtain the

SE-CARS response from the MMBN molecule in this configuration as well.

Besides the TPEL background, we also observe FWM background. Though always present, this FWM background is not observed to be as strong as the TPEL background and is found to be less than 5% relative to the molecular SE-CARS signal, i.e. significantly less compared to the FWM contribution in the Au-Au nanojunction. Unlike the gold nanojunction, the heterojunction appears stable. We do not observe blinking of the SE-CARS signal on the time scale of minutes, and the overall magnitude of the signal also remains constant on this time scale. From this observation we infer that thermal effects are less prominent in the heterojunction compared to the situation in the Au-Au junctions.

4.4 Discussion

In this work, we have used an experimental configuration to perform wide-field SE-CARS microscopy experiments in a repeatable and controllable manner, using low incident intensities. This chosen geometry consists of Raman-active molecules placed inside a cavity formed between a nanoparticle and a planar gold film, while the illuminating pump and Stokes beams arrive at their respective Kretschmann angles in order to excite propagating SPP modes. We have used both metallic and dielectric nanoparticles to form these junctions and have successfully driven Raman coherences in the sample. This technique shows that we do not need to exclusively rely on lossy metallic platforms to create confined nanoscopic hotspots, as our results show that dielectric materials can be involved in the formation of the confined local fields required for SE-CARS.

Here, we have used collimated pump and Stokes beams for wide-field illumination. Compared to traditional point-scanning CARS microscopes. This wide-field geometry allows for orders-of-magnitude lower average intensities incident on the sample. In the Au film-Au particle

configuration, the field enhancement in the junction exceeds one hundred times ($\beta > 100$). While the intense local field enables stronger light-matter interaction, the accompanying TPEL background makes it difficult to achieve higher signal levels by raising the illumination dosage. There is also a coherent FWM contribution from the gold itself because of its strong $\chi^{(3)}$ response. However, in the Kretschmann illumination mode, the background FWM signal is much weaker than the incoherent TPEL background from the gold. This observation correlates well with previous work [24, 20, 25]. In addition, thermal effects are present as intermittent blinking of the signal points, accompanied by an overall decay of the signal.

In order to reduce local heating effects at the junction and the strong TPEL radiation from the gold, we have used silicon nanoparticles that exhibit a high refractive index in the visible and near-infrared spectral range. Nanostructures fabricated from silicon and other similar high-index dielectric materials are known to provide significant confinement of the electric and magnetic fields, making them ideal candidates for optical nanoantenna applications. Silicon's ability to provide strong local fields along with its low-loss nature and thermal stability are features that led us to explore its use for SE-CARS [4, 5]. Numerical simulations show a total enhancement of $\sim 10^{12}$ in the case of Au film-Si particle system. Note that because of the $\sim \beta^8$ dependence of the SE-CARS signal such enhancements are substantial compared to what is commonly achieved for SERS measurements. Yet, the total enhancement factor obtained here is still relatively modest for a SE-CARS measurement.

The use of Si as a high-index dielectric material to form nanojunctions minimizes some of the major drawbacks encountered in typical all-metal nanoantennas. In particular, the unfavorable structural changes to antennas due to local heating is reduced here significantly (because of lower optical absorption and higher specific heat of Silicon[17, 5]) as evidenced through reduced blinking and improved stability of the signal. Both TPEL and FWM backgrounds are present in this geometry as well, but due to the non-luminescent and non-plasmonic nature of dielectric Si nanoparticles (with radii much larger than the exciton radius), the

TPEL background is significantly reduced in Au film-Si particle systems. However, the lower effective β requires higher illumination dosage and longer acquisitions times to be able to generate detectable SE-CARS signal. The continued illumination at higher power densities can eventually damage the flat Au film, limiting the allowable radiation dosage in this geometry as well. Nevertheless, this metal film-dielectric particle system allows more control over the measurements compared to the metal film-metal particle system. The inherent limitation of this geometry is the strong TPEL background that is always present even though it is reduced for the dielectric particle-metal film heterojunction by more than a factor of 3 relative to the all-metal nanojunction. The next logical step in this field would be to use all-dielectric nanoantenna systems that are not susceptible to intense thermal effects at the junctions and that can effectively eliminate the TPEL background.

4.5 Conclusions

We have demonstrated an experimental geometry to perform reliable, repeatable and controllable SE-CARS measurements at metal film-metal particle and metal film-dielectric particle nanojunctions. We successfully show generation of molecular SE-CARS signals using the lowest reported average illumination densities to date. We also show SE-CARS spectroscopy at metal film-dielectric particle heterojunctions, paving the way for development of new biomolecular sensing assays that do not rely on lossy and fragile metallic nanojunctions.

Chapter 5

Enhancement of molecular coherent Raman scattering with silicon nano-antennas

5.1 Rationale

Surface-enhanced Raman scattering (SERS) is a popular tool for molecular sensing at ultralow analyte concentrations. In the conventional implementation of this technique, antennas composed of metallic nano-structures are used to efficiently capture and confine light to nanoscopic regions that contain the molecular species of interest [176, 20]. The molecule is efficiently driven by the confined optical fields in the electromagnetic "hotspot" and the nanoantenna then efficiently outcouples the induced near-field Raman polarization to far-field radiation, which is subsequently captured with a photodetector [180, 181, 182]. Ever since the inception of SERS in 1973 [209], numerous SERS enhancement structures have been devised and the technique has been successfully extended to capture Raman spectra

from single molecules [46, 183, 184]. The mechanisms behind optical field localization and enhancement of the signal in SERS have been intensely studied and are generally well understood. While SERS allows enormous enhancement of the feeble Raman signal, acquisition rates beyond one to few tens of Hz are difficult to achieve in the single or few-molecule limit [185, 19]. DNA sequencing, rapid molecular screening and other high-throughput applications necessitate faster readout rates that SERS alone may not be able to provide.

Surface-enhanced analogues of coherent Raman scattering (CRS) methods are promising candidates to probe molecular vibrations at much faster rates compared to SERS. Surface-enhanced CRS was first demonstrated in 1979 where the coherent anti-Stokes Raman scattering (CARS) signal from liquid benzene was amplified with the help of surface plasmon polaritons supported on a flat Ag film antenna [194]. Subsequent progress on surface-enhanced CRS has focused largely on engineering metallic nanoantennas based on Au and Ag to increase and/or optimize the sensitivity of detection [210, 211, 212, 213, 214, 215, 130, 216, 217, 24, 25, 132, 218, 219, 220]. The quest has seen considerable success and single-molecule sensitivity has been demonstrated by multiple groups [195, 121, 131, 177]. However, significant local heating at metallic junctions has proved to be a major obstacle, affecting the reproducibility of the SE-CARS measurements. When subjecting metallic nanoantennas to ultrafast irradiation, the local peak intensities can reach $\sim 10^{12} - 10^{13}$ W/cm^2, a range in which photo-induced ionization of the molecule can happen due to the bending of the potential followed by electron tunneling [140, 137, 196, 136, 197, 133, 134, 198, 135, 141]. The morphological changes to the antenna due to intense local heating and plasmon-induced chemistry make it notoriously difficult to perform SE-CARS measurement in a reliable and reproducible manner [20].

The reproducibility challenges associated with SE-CARS measurements based on plasmonic nanoantennas originate from photo-induced heating effects that are intrinsic to metals. To make SE-CARS systems more reliable, moving beyond these lossy and fragile metallic sub-

strates is necessary. High-index dielectric particles such as Si, Ge and GaP are known to exhibit favorable electromagnetic and thermal properties at the optical and near-infrared frequencies [4, 5, 17, 8, 221]. These properties make them particularly suitable for surface-enhanced spectroscopy applications, where heating of the antenna is a limiting factor. In nanoantennas based on these materials, localization of the incident optical fields occur as strong displacement currents are generated inside the material. These currents produce electromagnetic fields both inside and outside the material, which lead to confinement of the incident electromagnetic fields when nanocavities are formed between these dielectric particles. The potential of dielectric nano-structures to efficiently confine the electromagentic field has been known for a while and has been implemented in some SERS studies [8, 112, 66, 64, 63, 110]. We have recently shown that the use of dielectric materials in antenna designs can help mitigate photo-induced instabilities in SE-CARS measurements[222]. That work focused on antennas formed between a Si nanoparticle and a flat Au film, which afforded reproducible SE-CARS signals, but suffered from a strong electronic two-photon excited luminescence (TPEL) background originating from the gold film.

In our current work, we present the first demonstration of SE-CARS measurements without the involvement of surface plasmons supported by metallic nanostructures. Instead, we use a Si-based all-dielectric nano-antenna with favorable thermal properties for stabilizing the CARS signal as well as to substantially reduce the TPEL background. Using all-dielectric nanojunctions, we show that the stability of the CARS signal is dramatically improved relative to the SE-CARS signal observed from Au nano-dumbbell based antennas. This work paves the way for future surface-enhanced coherent Raman sensors that offer the reproducibility needed for reliable high-speed biomolecular screening applications.

5.2 Methods and materials

5.2.1 Sample preparation

The silicon-based nano-antennas in this study are assembled from 150 nm diameter, pyridine-functionalized Si nanoparticles (Meliorum Technologies), which are used without further purification. The nano-particles are suspended in water, sonicated and spin-cast on a BK7 coverslip prior to measurement. Nanojunctions are formed by spontaneous congregation of the particles during the spin-casting process. We use gold-based nano-antennas as a reference system for comparison. This antenna system has previously been used for SE-CARS experiments.[121, 141] The system consist of dimers of $\sim$ 90 nm diameter Au nanospheres, covered with trans 1,2-bis(4- pyridyl) ethylene (BPE), obtained from Cabot Security Materials. The nano-dumbbells are encapsulated in a silica shell of thickness 40-70 nm. The nano-dumbbells are suspended in water, sonicated and spin-cast onto BK7 glass coverslips. The SE-CARS spectrum of the BPE-functionalized Au dumbbell antenna shows two clear peaks in the 1560-1650 cm^{-1} range, attributed to the pyridyl ring stretching mode and the ethylene C=C stretching vibration. Figure 5.1 shows the SE-CARS spectrum of BPE molecules adhered to the Au nano-dumbbell system in the 1570 cm^{-1} to 1655 cm^{-1} range. The spectrum shows the expected pyridyl ring stretching mode and the ethylene C=C stretching mode, obtained from a single dumbbell antenna. Representative on-resonance (1600 cm^{-1}) and off-resonance (1560 cm^{-1}) SE-CARS images of clustered dubmbell antennas, spin-cast on a glass coverslip, are shown in the figure as well.

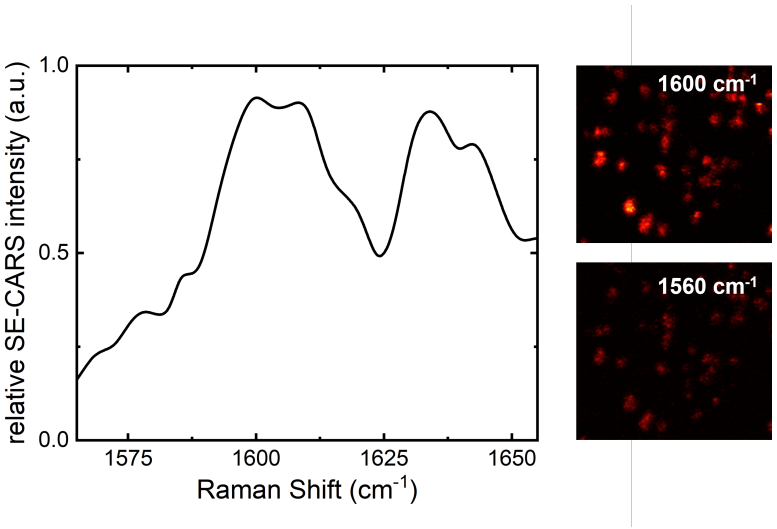

Figure 5.1: SE-CARS spectrum of BPE molecule taken with Au nanodumbell atneanna showing two distinct peaks located around 1600 cm^{-1} and 1635 cm^{-1}. Representative on (1600 cm^{-1}) and off (1560 cm^{-1}) resonance images are shown next to the SE-CARS spectrum.

5.2.2 SE-CARS imaging experiments

A schematic of the SE-CARS microscope system is shown in Figure 5.2. The SE-CARS system is based on a laser-scanning optical microscope (Fluoview 300, Olympus) with an Olympus IX71 inverted microscope frame. A modelocked fiber laser (aeroPULSE, NKT Photonics) with ∼2 ps long pulses and 80 MHz repetition rate provides the wavelength-fixed Stokes beam (1031 nm) for the SE-CARS experiments. A portion of this beam is frequency-doubled and the generated 515.5 nm beam synchronously pumps an optical parametric oscillator (Picoemerald, APE) to generate the tunable (700-960 nm) pump beam. The beams are spatially and temporally overlapped and subsequently conditioned to produce linearly polarized beams with clean transverse Gaussian profiles. The collinear beams are then focused using a water immersion 1.15 NA 40x objective lense (Olympus). The generated anti-Stokes signal is collimated using a condenser, filtered (775 ± 25 nm, Semrock) and detected using a photo-multiplier tube (R3896, Hamamatsu). In the experiments involving Si-particles, the average power for each beam is varied between 500 μW - 2 mW at the sample plane. A galvanometric scanner allows raster scanning over an 117 μm × 117

μm area of the sample, with a pixel dwell time of 4.27 μs per pixel. This corresponds to 1.12 frames/second acquisition rate for a 512 $\times$ 512 frame. For SE-CARS measurements on Au nano-dumbbells, the power for each of the incident beams is varied between 10 μW - 500 μW at the sample plane, while using the same dwell time of 4.27 μs per pixel.

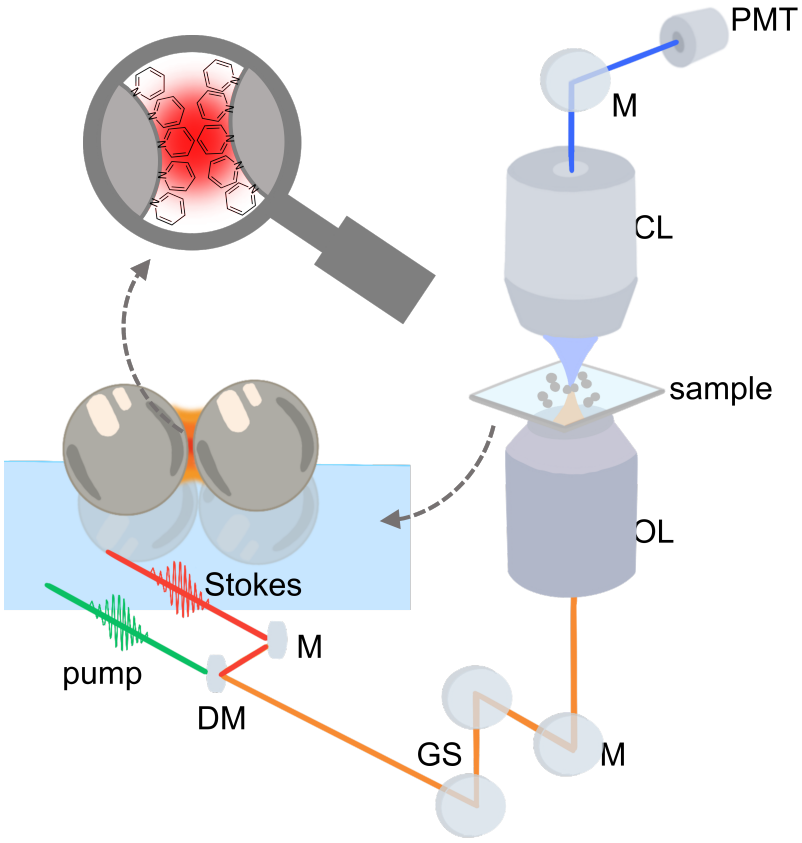

Figure 5.2: Schematic of the SE-CARS microscope. GS, galvanometric scanner; M, mirror; DM, dichroic mirror; OL, objective lens; CL, condenser lens; PMT, photomultiplier tube

5.2.3 Numerical simulations

Lumerical FDTD is used to perform local electromagnetic field calculations using the finite-difference time-domain (FDTD) method. Data for the dielectric function of all the materials are taken from the Palik library [204]. In the simulations, we consider nanojunctions formed

between two Si nanoparticles, forming a dimer as the exemplar nanoantenna system. Fine meshing of 0.1 nm is used near the Si-dimer junction. The same geometry is used to calculate the absorption spectrum of the antenna system. Electromagnetic field enhancement data for the Au nano-dumbbell system are taken from Crampton et al. [141].

COMSOL Multiphysics is used to calculate the thermal response of both nanoantenna systems due to exposure to electromagnetic radiation. Water is chosen as the surrounding media in order to replicate actual experimental conditions. The Palik library is used for the thermal simulations as well.

5.3 Results

5.3.1 SE-CARS with Si nanoantenna

In this work, we move away from metal-based nanoantenna systems and use dielectric antenna formed from clustered Si-nanoparticles to enhance the coherent Raman response of the molecule. In order to examine the capability of this dielectric antenna to efficiently capture and confine incident optical fields, we use Lumerical FDTD to calculate the expected absorption spectrum of the antenna and the local fields inside the nanojunction. Figure 5.3a shows the calculated extinction spectrum of an antenna system from two Si-nanoparticles that form the exemplar dimer, along with the pump, Stokes and anti-Stokes frequencies involved in the experiment. The spectrum of the dielectric antenna is composed of a magnetic response in the optical range in addition to an electric resonance. This response is due to the displacement currents originating from the oscillation of bound electrons. The electric field calculations (shown in Figure 5.3b) reveal an effective field enhancement factor β_p of $\sim$14 for the pump wavelength of 885 nm. Similar calculations are performed for the Stokes and anti-Stokes wavelengths resulting in $\beta_s = 13$ ($\lambda_s = 1031$ nm) and $\beta_{as} = 15$ ($\lambda_{as} = 775$ nm).

As such, the expected overall CARS enhancement factor is $\beta_p^4\beta_s^2\beta_{as}^2 = 1.46 \times 10^9$. The diameter of the electromagnetic hotspot is estimated as ~6 nm. Assuming a surface coverage of 6 molecules/nm^2 and both particles have monolayers of pyridine, we are exciting ~340 molecules in each junction.

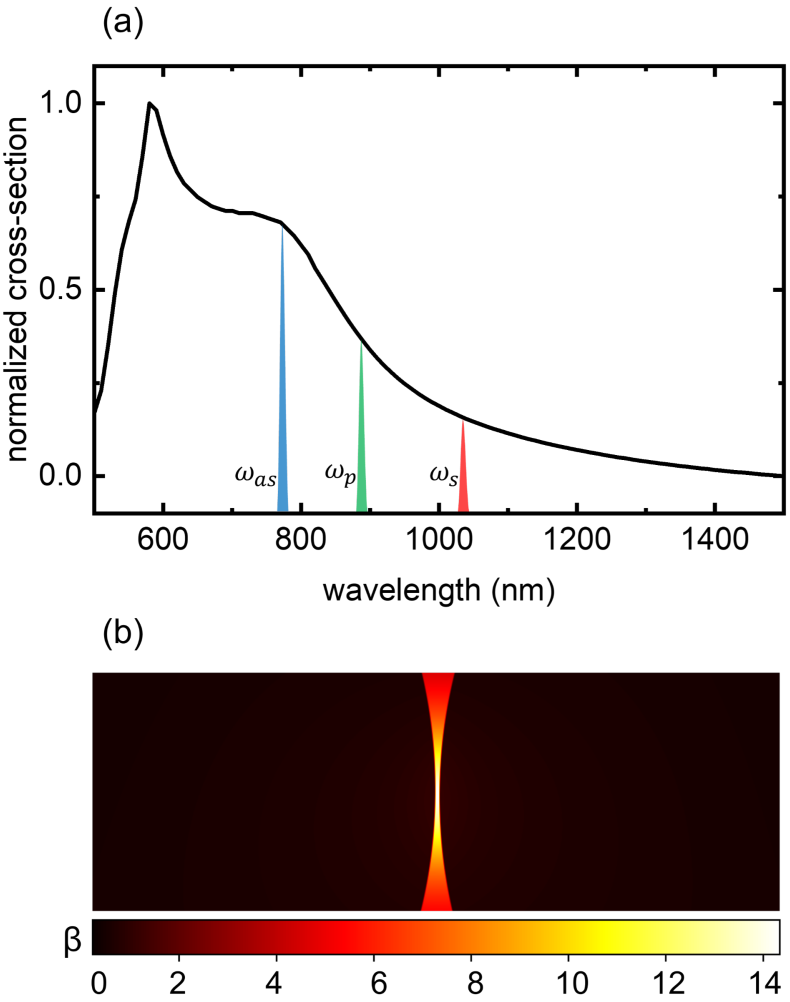

Figure 5.3: a) Calculated absorption spectrum of Si dimer nanoantenna system. The three colors represent the anti-Stokes, pump and Stokes wavelengths (from shorter to longer wavelengths). b) local electric field enhancement near the Si-Si nanojunction under 885 nm illumination. The local field enhancement factor is denoted by $\beta(\omega) = |E_{loc}/E_0|$

We target the ring stretching modes near 1580 cm^{-1} for our SE-CARS experiment based on the CARS spectrum for 99% pure pyridine, as seen in Figure 5.4(a). The spectral measurements are taken at 6 cm^{-1} intervals, ranging from 1552 cm^{-1} to 1630 cm^{-1}. This corresponds

to scanning the pump wavelength between 882.7 nm and 888.8 nm. The spontaneous Raman spectrum of pyridine shown in Figure 5.4(b) reveals that the CARS signature derives from several Raman modes. The pyridine modes in this range are substantially weaker than the ring breathing modes near 1000 cm^{-1} [223], but the selected modes are targeted here because of better laser performance for the CARS process in this spectral range. Note that in addition to the resonant signature in the CARS spectrum, a nonresonant background from pyridine itself is present.

In the dielectric nanoantenna system, consisting of clusters of Si particles, the measurements consistently produce vibrationally resonant signal from the target molecule. Background signal is acquired by temporally separating the pump and Stokes beams by 8 ps where no overlap is present. This background is subtracted to obtain the vibrationally resonant SE-CARS image. Figure 5.5a shows an SE-CARS image of clustered Si particles. The clusters appear as bright spots that are close to the diffraction-limited resolution of the SE-CARS microscope. Given the size of the spots, we estimate that these locations may each contain one to six 150 nm Si particles. Two sample locations (labeled 1 and 2 in Figure 5.5a) show the expected SE-CARS response from pyridine, suggesting the successful formation of a nanojunction, as evidenced by a distinct and reproducible peak in the 1580-1600 cm^{-1} region. Figure 5.5b shows the mean SE-CARS spectrum with one standard deviation of error, obtained from 50 individual particle clusters. The spectrum shows clear vibrational sensitivity near the 1580-1600 cm^{-1} spectral region. To the best of our knowledge, this is the first demonstration of surface-enhanced coherent Raman scattering with non-metallic antenna.

The CARS vibrational feature observed in the imaging experiments appears blue-shifted from the CARS signature seen in pure pyridine. Density functional theory calculations show that the pyridyl ring stretching vibration is expected to blue-shift upon bonding of the nitrogen to silicon (see section 5.4). The blue-shift observed in the SE-CARS measurements

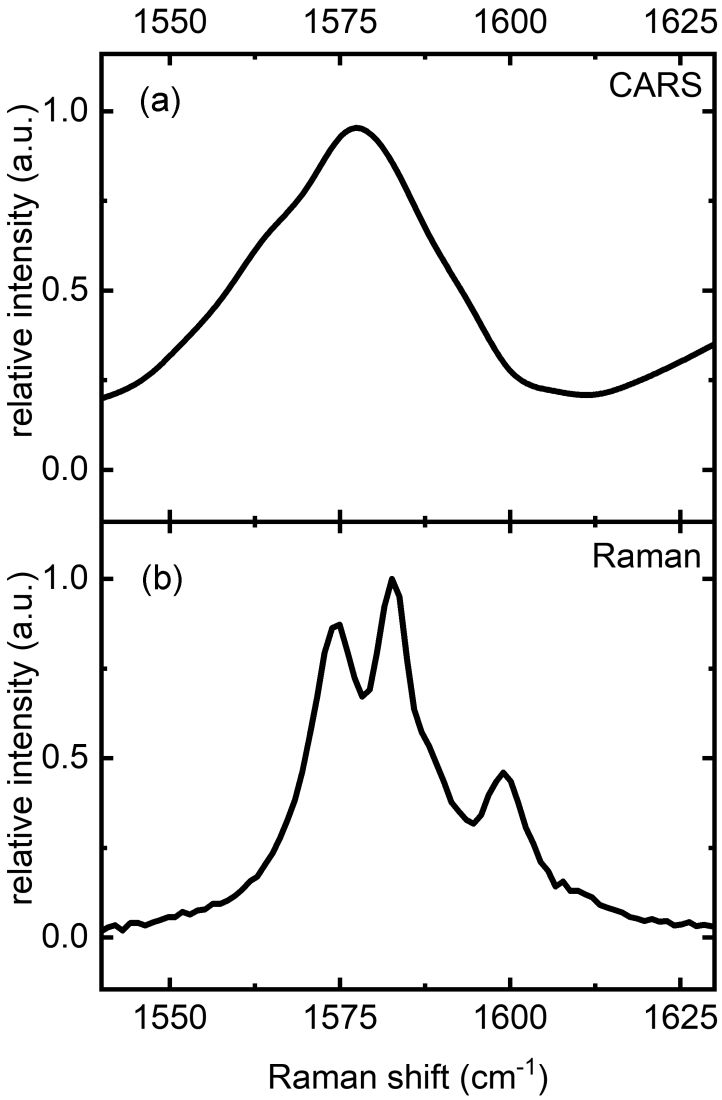

Figure 5.4: (a) CARS and (b) spontaneous Raman spectra of 99% pyridine in the 1540-1630 cm^{-1} range.

thus supports the notion that the vibrational signature in the 1580-1600 cm^{-1} range can be attributed to silicon-bonded pyridine molecules.

We note that there is a persistent background in most images taken in this configuration. The background signal is vibrationally non-resonant, depends on the spatial and temporal overlap of both beams and radiates at the $(2\omega_p - \omega_s)$ frequency. Based on this observation, the origin of this background is determined to be four-wave mixing (FWM) due to the strong $\chi^{(3)}$ response of Si, which is found to contribute on average ~24% of the total signal on resonance. The contribution from broadband TPEL is on average <4%.

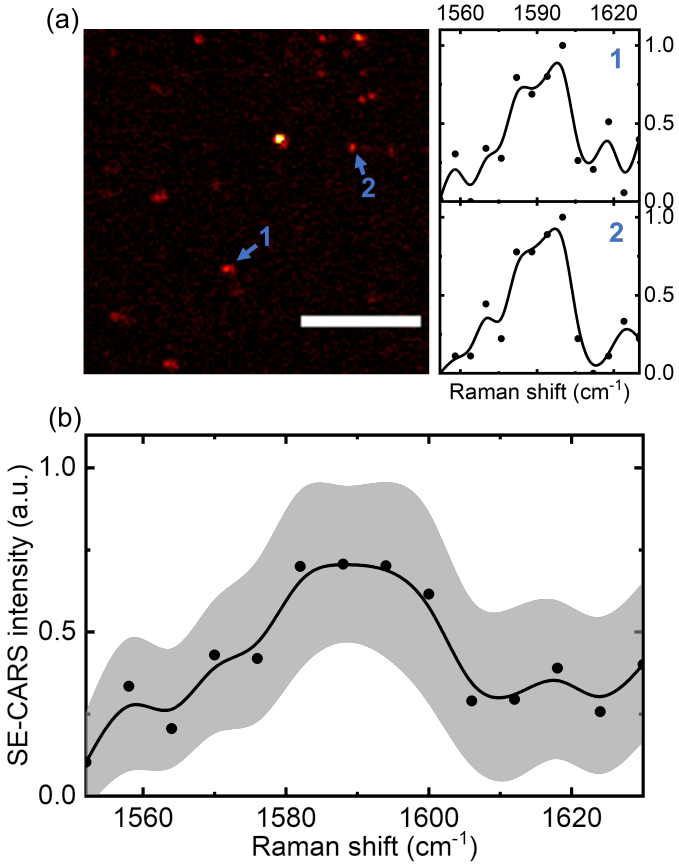

Figure 5.5: SE-CARS with Si nanoantenna. (a) SE-CARS image of pyridine functionalized Si nanoantenna system at 1582 cm^{-1}. Two representative spectra taken from locations 1 and 2. Scale bar is 10 μm. (b) Average of 50 SE-CARS spectra obtained from different locations. The line connecting the dots is used as a visual guide.

5.4 Density functional theory calculation of Si-bonded pyridine

GaussView 6.0.16 is used to perform the density functional theory (DFT) calculations on bulk pyridine and pyridine attached to Si atoms. For these simulations, the PBEPBE method with a tzvp basis set is utilized to optimize the chemical structure and determine its subsequent Raman activity. Our specific focus is the vibrational energy of the ring stretching vibration of pyridine in the 1570-1600 cm^{-1} range. In pure pyridine, the DFT simulation predicts that the ring stretching mode peaks at 1577 cm^{-1}. To gain insight in the Raman spectrum of pyridine bound to silicon, we have explored several structures. In all structures where there is a bond between the nitrogen atom of pyridine and a silicon atom, we observed a blue shift of the ring stretching vibration. A representative structure is shown in Figure 5.6, which is based on 13 silicon atoms arranged in a diamond lattice structure, using Si-H bonds for terminal and corner atoms. In this structure, the nitrogen atom is bonded to a silicon atom that has three Si nearest neighbors. The distance between Si atoms is 2.4 Å and the Si-N bond length is 1.9 Å. In this model structure, a blue-shift of the dominant peak is observed, from 1577 cm^{-1} to 1607 cm^{-1}, as shown in Figure 5.7. This corroborates our SE-CARS experiments on pyridine-functionalized Si nanoparticles, where we observe a blue-shift of the SE-CARS signal from the CARS signal relative to pure pyridine in all of our measurements.

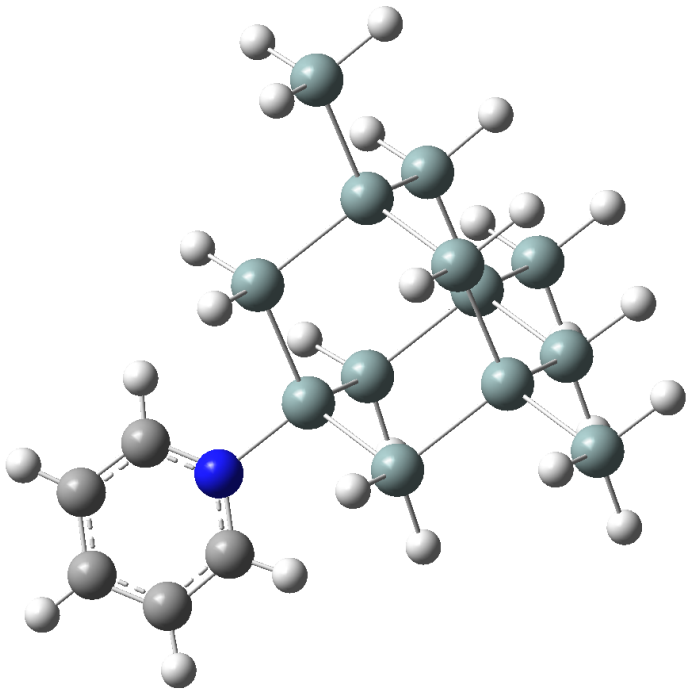

Figure 5.6: Configuration of tetrahedral Si lattice attached to a pyridine molecule via an Si-N bond

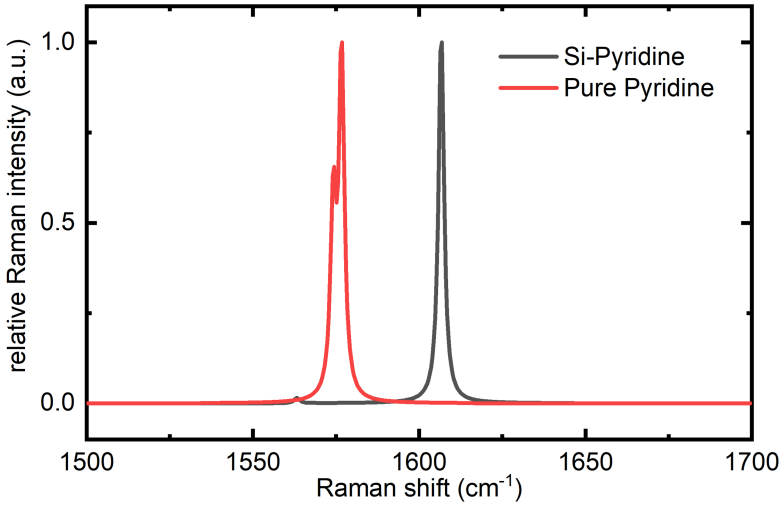

Figure 5.7: Calculated normalized Raman spectra of pure pyridine (red line) and pyridine attached to a Si atom (black line)

5.5 Thermal stability of dielectric and metal nanoantenna

Figure 5.8a shows an FEM calculation (using COMSOL Multiphysics) of electromagnetic heating comparing the Si-dimer nanoantenna with a gold-based one. Both systems are immersed in water. The calculation demonstrates that under the exact same conditions and for the same geometrical dimension, heating of the Au antenna is ∼13 times higher (37.1 K) compared to heating of the Si (2.89 K) antenna. This simulated result is mirrored in experimental findings as well. We acquire SE-CARS images from ensembles of either Au or Si antenna systems for 291 seconds with 1.12 seconds per frame (4.27 μs/pixel). The incident power levels for both pump and Stokes beams were 2 mW at the sample plane for the Si antenna and 500 μW for Au antenna. While signal from the Au nano-dumbbell system decays rapidly and loses ∼60% signal within 120 seconds (Figure 5.8,top), the signal from the Si nanoantenna system remains robust with no noticeable decay in signal even after the end of the time series (Figure 5.8,bottom). The numerical calculation and experimental observation of signal strength over time strongly supports our hypothesis that Si-based nonplasmonic nanoantennas can provide a new way to perform surface-enhanced coherent Raman scattering measurements with improved stability, reliability and reproducibility.

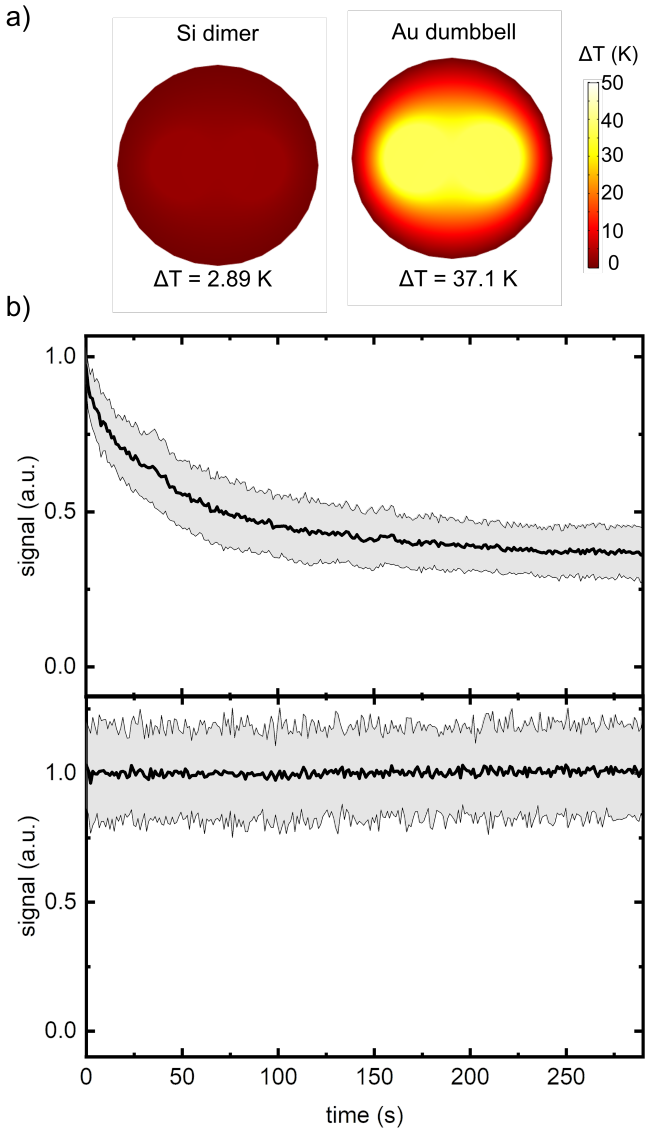

Figure 5.8: Thermal response of Si and Au nanoantenna systems. (a) FEM calculation of steady-state temperature of Si-dimer and Au nano-dumbbell antennas under 1 mW, 885 nm cw illumination. (b) Time evolution of experimental signal strength over 291 seconds for Au dumbbell (top) and Si-particle cluster (bottom) nanoantenna at their respective molecular resonance (1600 cm^{-1} for Au dumbbell and 1588 cm^{-1} for Si antenna system). The data represents averaged signal from 100 individual locations for each system.

5.6 Discussion

In this work, we present the first experimental demonstration of surface-enhanced coherent Raman scattering of molecules with dielectric nanoantennas. Our recent work [222], where we introduced metal-dielectric heterojunctions to improve thermal stability of the SE-CARS signal, motivated us to explore the use of non-metallic nanoantennas for SE-CARS measurements. The results discussed herein shows that it is possible to move beyond lossy and thermally unstable metallic systems and use all-dielectric nanoantennas for surface-enhanced coherent Raman scattering experiments instead.

We have used spatially and temporally overlapped pump and Stokes beams in a laser-scanning microscope for the SE-CARS experiments. We successfully obtain stable and reproducible coherent Raman signal from our target molecule. In most of our measurements, we observe a persistent FWM background accompanying the molecular signal, due to the strong $\chi^{(3)}$ response of Si. The non-luminescent nature of the dielectric Si nanoparticles results in a much lower luminescent background compared to metal-based SE-CARS systems. The fields inside the dielectric dimer junctions are rather modest ($\beta \sim 14$) compared to what can be achieved using metallic nanoantennas. However, the overall CARS enhancement is substantial ($\sim 10^9$) due the $\sim \beta^8$ dependence of the SE-CARS signal. Unlike previous SE-CARS antenna systems where morphological distortion of the structure due to photo-induced heating [141, 121] or intense TPEL background [222] limits the allowable illumination dosage, this work enables us to apply higher field intensities to enhance the molecular signal even further. The increased incident intensity can compensate for the lower values of β, generating comparable signals as previously observed with metal-based antenna systems.

Compared to SERS measurements, which scale as β^4, the SE-CARS approach benefits from a much larger overall enhancement effect, which makes dielectric antenna systems especially

attractive for nonlinear Raman measurements. In this context, we note that we have performed regular SERS micro-spectroscopy measurements on the same Si-particle clusters. Using 532 nm or 785 nm excitation light of up to 10 mW, focused on a single cluster of pyridine-coated Si-particles, we have observed no vibrational SERS signatures of pyridine with integration times up to 10 s. We surmise, therefore, that the use of dielectric antennas may have a larger impact on the SE-CARS field compared to their impact on SERS applications.

We have chosen Si as our antenna material because of its high refractive index in the visible and near-infrared frequencies. As a result, Si based nanoantennas can efficiently capture and confine incident optical fields to nanoscopic regions. Furthermore, Si suffers less from the ohmic losses and adverse thermal effects that are intrinsic to metallic nanoantennas. This favorable thermal response is due to the higher specific heat of Si (5x higher compared to Au [68]). The improved thermal stability is evidenced in experiments as well. In metallic systems, blinking-type behavior of the signal and the decay of signal over a short period of time is common. However, when we use dielectric antennas, such behavior is not observed.

While this work provides a solution to a longstanding limitation of traditional surface-enhanced CRS sensors, there are steps that can be taken to improve it even further. Fabricating dielectric nanostructures with tailored electric and magnetic properties can make the nanoantenna more efficient and improve the reliability and repeatability of the signal. In addition, immobilized periodic enhancement structures can be employed for high throughput biomolecular screening purposes, an application where SE-CARS can provide much faster signal acquisition than possible with SERS based screening systems. Finally, red-shifting the pump and Stokes beams can reduce optical absorption to even lower levels. The lower absorption can help with the thermal response of the material, as well as reduce the electronic background.

5.7 Conclusion

We have presented an experimental demonstration of surface-enhanced coherent anti-Stokes Raman scattering (SE-CARS) of molecules with a dielectric Si nanoantenna. We have found that the thermal stability of the SE-CARS signal from such dielectric antennas is significantly better compared to corresponding signals from Au nano-dumbell antennas. This work shows that the inclusion of a dielectric nanoantenna can overcome the longstanding limitation of traditional metallic SE-CARS systems where unfavorable thermal properties adversely affect the stability and reproducibility of the measurements.

Chapter 6

Summary and outlook

Nonlinear nanophotonics is a relatively young and promising research field. Metallic nanostructures that have been used as optical antennas for amplifying nonlinear light-matter interaction are based on relatively straightforward concepts, yet their impact has been significant in uncovering the exquisite properties of materials. These nonlinear plasmonic systems take advantage of coherent oscillations of conduction electrons near nanostructured metal surfaces. The oscillations give rise to surface plasmon polaritons, which are surface bound propagating electromagnetic waves, and localized surface plasmons whose resonances have a strong dependence on the morphology of the antenna. A significant portion of the work in the field of nonlinear nanophotonics has focused on frequency conversion applications such as second harmonic generation and third harmonic generation. Applications in molecular spectroscopy such as coherent Raman scattering and surface-enhanced fluorescence measurements have been somewhat limited compared to their linear analogues. Nevertheless, significant advances have been made in the field over the last decade and highly sensitive surface-enhanced nonlinear optical spectroscopy and microscopy systems have been developed.

The majority of surface-enhanced nonlinear optical sensors reported in literature so far rely on LSPR-based optical nanoantennas for capturing and confining incident electromagnetic fields to enhance light-matter interaction. However, these LSPR-based nanoantennas suffer from ohmic losses and subsequent adverse thermal effects that are inherent to metallic systems. These effects become particularly concerning in ultrafast nonlinear optical processes where the photothermal heating induces irreversible damage to the antenna, affecting the stability and reproducibility of the signal. However, the ability of these antennas to produce remarkably enhanced near-fields has motivated researchers in the field to use these systems at the expense of significantly reduced stability of the sensor. In this dissertation, we take a different approach to building novel nonlinear nanophotonic chemical sensors that are not as susceptible to thermal effects as LSPR-based sensors and use a systematic route to move towards metal-free nanoantennas for enhancing light-matter interaction.

The first system presented in this dissertation reports a two-photon absorption based novel optical sensor. Through successful interrogation of SPP-enhanced third-order optical response of planar gold films, a novel optical imaging/sensing strategy has been developed that enables label-free detection of biomolecular interactions on a single-nanoparticle level. Individual binding events appear as confined, bright spots against a dark background. The mechanism of signal generation is discussed and the proposed mechanism is verified with experiments. The well-behaved point-spread function, the ability to recognize nanoscopic binding events and the overall facile implementation of the detection scheme demonstrate its promise by overcoming the inherent limitations (non-ideal PSF, bright background) present in traditional SPRM technique.

The second nonlinear nanophotonic chemical sensor reported in this dissertation probes the vibrational response of molecules through surface enhanced coherent anti-Stokes Raman scattering. The system consists of a reimagined experimental particle-on-a-film geometry in order to provide improved stability of the antenna junction and generation of the SE-CARS

signal in a reliable and repeatable manner. In this study, controllable and repeatable wide-field surface-enhanced CARS (SECARS) measurements are performed at metal film-metal particle and metal film-dielectric particle nanojunctions. SE-CARS signal at metal-metal junctions are obtained using the lowest average power densities to date. For the first time, reproducible SECARS measurements at metal-dielectric heterojunctions are demonstrated, opening the possibility of all-dielectric SE-CARS sensors not constrained by lossy and fragile metallic antenna systems.

The third and final nonlinear nanophotonic sensor discussed in this dissertation presents the first experimental demonstration of SE-CARS of molecules without any involvement of surface plasmons. Silicon is chosen here due to its favorable optical and thermal properties in the visible and NIR regimes. This silicon based dielectric nanoantenna system does not suffer from the ohmic losses and subsequent detrimental thermal effects that are unavoidable in metal-based nanoantennas. This antenna configuration produces robust SE-CARS signal from the target molecule with exceptionally stable signal strength with significantly reduced background.

In summary, this dissertation discusses the development of chemical sensors that are able to produce stable and reproducible signal based on surface-enhanced third-order nonlinear optical effects. With a vision to overcome the inherent limitations posed by traditional LSPR-based optical nanoantennas for spectroscopy, this work takes a methodical approach in redesigning nanoantennas that are easy to fabricate and produce robust signal.

Bibliography

[1] Denis G Baranov, Dmitry A Zuev, Sergey I Lepeshov, Oleg V Kotov, Alexander E Krasnok, Andrey B Evlyukhin, and Boris N Chichkov. All-dielectric nanophotonics: the quest for better materials and fabrication techniques. *Optica*, 4(7):814–825, 2017.

[2] Reuben M Bakker, Dmitry Permyakov, Ye Feng Yu, Dmitry Markovich, Ramón Paniagua-Domínguez, Leonard Gonzaga, Anton Samusev, Yuri Kivshar, Boris Luk'yanchuk, and Arseniy I Kuznetsov. Magnetic and electric hotspots with silicon nanodimers. *Nano Letters*, 15(3):2137–2142, 2015.

[3] Elisabet Xifré-Pérez, R Fenollosa, and F Meseguer. Low order modes in microcavities based on silicon colloids. *Optics Express*, 19(4):3455–3463, 2011.

[4] Martín Caldarola, Pablo Albella, Emiliano Cortés, Mohsen Rahmani, Tyler Roschuk, Gustavo Grinblat, Rupert F Oulton, Andrea V Bragas, and Stefan A Maier. Non-plasmonic nanoantennas for surface enhanced spectroscopies with ultra-low heat conversion. *Nature communications*, 6(1):1–8, 2015.

[5] Pablo Albella, Rodrigo Alcaraz de la Osa, Fernando Moreno, and Stefan A Maier. Electric and magnetic field enhancement with ultralow heat radiation dielectric nanoantennas: considerations for surface-enhanced spectroscopies. *Acs Photonics*, 1(6):524–529, 2014.

[6] Kevin T Crampton, Alexander Fast, Eric O Potma, and V Ara Apkarian. Junction plasmon driven population inversion of molecular vibrations: a picosecond surface-enhanced raman spectroscopy study. *Nano letters*, 18(9):5791–5796, 2018.

[7] Emily L Keller and Renee R Frontiera. Ultrafast nanoscale raman thermometry proves heating is not a primary mechanism for plasmon-driven photocatalysis. *ACS nano*, 12(6):5848–5855, 2018.

[8] Ivano Alessandri and John R Lombardi. Enhanced raman scattering with dielectrics. *Chemical reviews*, 116(24):14921–14981, 2016.

[9] TH Mairnan. Stimulated optical radiation in ruby. *Nature*, 4736:493–494, 1960.

[10] Robert W Boyd. *Nonlinear optics*. Elsevier, 2003.

[11] Stefan Alexander Maier. *Plasmonics: fundamentals and applications*. Springer Science & Business Media, 2007.

[12] Mario Bertolotti, Concita Sibilia, and Angela M Guzman. *Evanescent waves in optics: an introduction to plasmonics*, volume 206. Springer, 2017.

[13] Yong Chen and Hai Ming. Review of surface plasmon resonance and localized surface plasmon resonance sensor. *Photonic Sensors*, 2(1):37–49, 2012.

[14] Martti Kauranen and Anatoly V Zayats. Nonlinear plasmonics. *Nature photonics*, 6(11):737, 2012.

[15] Lukas Novotny and Bert Hecht. *Principles of nano-optics*. Cambridge university press, 2012.

[16] Judith Langer, Dorleta Jimenez de Aberasturi, Javier Aizpurua, Ramon A Alvarez-Puebla, Baptiste Auguié, Jeremy J Baumberg, Guillermo C Bazan, Steven EJ Bell, Anja Boisen, Alexandre G Brolo, et al. Present and future of surface-enhanced raman scattering. *ACS nano*, 14(1):28–117, 2019.

[17] Pablo Albella, M Ameen Poyli, Mikolaj K Schmidt, Stefan A Maier, Fernando Moreno, Juan José Sáenz, and Javier Aizpurua. Low-loss electric and magnetic field-enhanced spectroscopy with subwavelength silicon dimers. *The Journal of Physical Chemistry C*, 117(26):13573–13584, 2013.

[18] Katrin Kneipp, Yang Wang, Harald Kneipp, Lev T Perelman, Irving Itzkan, Ramachandra R Dasari, and Michael S Feld. Single molecule detection using surface-enhanced raman scattering (sers). *Physical review letters*, 78(9):1667, 1997.

[19] Chang Chen, Yi Li, Sarp Kerman, Pieter Neutens, Kherim Willems, Sven Cornelissen, Liesbet Lagae, Tim Stakenborg, and Pol Van Dorpe. High spatial resolution nanoslit sers for single-molecule nucleobase sensing. *Nature Communications*, 9:1733, 2018.

[20] Alexander Fast and Eric Olaf Potma. Coherent raman scattering with plasmonic antennas. *Nanophotonics*, 8(6):991–1021, 2019.

[21] Lukas Novotny and Bert Hecht. *Principles of nano-optics*. Cambridge university press, 2012.

[22] Robert Karlsson. Spr for molecular interaction analysis: a review of emerging application areas. *Journal of Molecular Recognition*, 17(3):151–161, 2004.

[23] Ignacy Gryczynski, Joanna Malicka, Zygmunt Gryczynski, and Joseph R Lakowicz. Surface plasmon-coupled emission with gold films. *The Journal of Physical Chemistry B*, 108(33):12568–12574, 2004.

[24] Alexander Fast, John P Kenison, Christopher D Syme, and Eric O Potma. Surface-enhanced coherent anti-stokes raman imaging of lipids. *Applied optics*, 55(22):5994–6000, 2016.

[25] John P Kenison, Alexander Fast, Facheng Guo, Alexander LeBon, Wei Jiang, and Eric O Potma. Imaging properties of surface-enhanced coherent anti-stokes raman scattering microscopy on thin gold films. *JOSA B*, 34(10):2104–2114, 2017.

[26] Evangelina Pensa, Emiliano Cortes, Gaston Corthey, Pilar Carro, Carolina Vericat, Mariano H Fonticelli, Guillermo Benitez, Aldo A Rubert, and Roberto C Salvarezza. The chemistry of the sulfur–gold interface: in search of a unified model. *Accounts of chemical research*, 45(8):1183–1192, 2012.

[27] Thomas Bürgi. Properties of the gold–sulphur interface: from self-assembled monolayers to clusters. *Nanoscale*, 7(38):15553–15567, 2015.

[28] Matthew J. Linman and Quan Jason Cheng. *Surface Plasmon Resonance: New Biointerface Designs and High-Throughput Affinity Screening*. Springer Berlin Heidelberg, Berlin, Heidelberg, 2009.

[29] K-F Giebel, Clemens Bechinger, Stephan Herminghaus, M Riedel, Paul Leiderer, Ulrich Weiland, and Martin Bastmeyer. Imaging of cell/substrate contacts of living cells with surface plasmon resonance microscopy. *Biophysical journal*, 76(1):509–516, 1999.

[30] Bo Huang, Fang Yu, and Richard N Zare. Surface plasmon resonance imaging using a high numerical aperture microscope objective. *Analytical chemistry*, 79(7):2979–2983, 2007.

[31] Bryce P Nelson, Timothy E Grimsrud, Mark R Liles, Robert M Goodman, and Robert M Corn. Surface plasmon resonance imaging measurements of dna and rna hybridization adsorption onto dna microarrays. *Analytical chemistry*, 73(1):1–7, 2001.

[32] Claire E Jordan and Robert M Corn. Surface plasmon resonance imaging measurements of electrostatic biopolymer adsorption onto chemically modified gold surfaces. *Analytical chemistry*, 69(7):1449–1456, 1997.

[33] W. Wang, Y. Z. Yang, S. P. Wang, V. J. Nagaraj, Q. Liu, J. Wu, and N. J. Tao. Label-free measuring and mapping of binding kinetics of membrane proteins in single living cells. *Nature Chemistry*, 4(10):846–853, 2012.

[34] K. Syal, R. Iriya, Y. Yang, H. Yu, S. Wang, S. E. Haydel, H. Y. Chen, and N. Tao. Antimicrobial susceptibility test with plasmonic imaging and tracking of single bacterial motions on nanometer scale. *ACS Nano*, 10(1):845–52, 2016.

[35] S. P. Wang, X. N. Shan, U. Patel, X. P. Huang, J. Lu, J. H. Li, and N. J. Tao. Label-free imaging, detection, and mass measurement of single viruses by surface plasmon resonance. *Proceedings of the National Academy of Sciences of the United States of America*, 107(37):16028–16032, 2010.

[36] Yuting Yang, Guangxia Shen, Hui Wang, Hongxia Li, Ting Zhang, Nongjian Tao, Xianting Ding, and Hui Yu. Interferometric plasmonic imaging and detection of single exosomes. *Proceedings of the National Academy of Sciences*, 115(41):10275–10280, 2018.

[37] A. R. Halpern, J. B. Wood, Y. Wang, and R. M. Corn. Single-nanoparticle near-infrared surface plasmon resonance microscopy for real-time measurements of dna hybridization adsorption. *ACS Nano*, 8(1):1022–30, 2014.

[38] H. Yu, X. N. Shan, S. P. Wang, H. Y. Chen, and N. J. Tao. Plasmonic imaging and detection of single dna molecules. *ACS Nano*, 8(4):3427–3433, 2014.

[39] A. M. Maley, G. J. Lu, M. G. Shapiro, and R. M. Corn. Characterizing single polymeric and protein nanoparticles with surface plasmon resonance imaging measurements. *ACS Nano*, 11(7):7447–7456, 2017.

[40] Shuo-Hui Cao, Wei-Peng Cai, Qian Liu, and Yao-Qun Li. Surface plasmon–coupled emission: what can directional fluorescence bring to the analytical sciences? *Annual Review of Analytical Chemistry*, 5:317–336, 2012.

[41] Joanna Malicka, Ignacy Gryczynski, Zygmunt Gryczynski, and Joseph R Lakowicz. Dna hybridization using surface plasmon-coupled emission. *Analytical chemistry*, 75(23):6629–6633, 2003.

[42] Derek S Smith, Yordan Kostov, and Govind Rao. Spce-based sensors: Ultrafast oxygen sensing using surface plasmon-coupled emission from ruthenium probes. *Sensors and Actuators B: Chemical*, 127(2):432–440, 2007.

[43] Evgenia Matveeva, Zygmunt Gryczynski, Ignacy Gryczynski, and Joseph R Lakowicz. Immunoassays based on directional surface plasmon-coupled emission. *Journal of immunological methods*, 286(1-2):133–140, 2004.

[44] Jun Dong, Zhenglong Zhang, Hairong Zheng, and Mentao Sun. Recent progress on plasmon-enhanced fluorescence. *Nanophotonics*, 4(1):472–490, 2015.

[45] Nam-Jung Kim, Jayeong Kim, Jun-Beom Park, Hyemin Kim, Gyu-Chul Yi, and Seokhyun Yoon. Direct observation of quantum tunnelling charge transfers between molecules and semiconductors for sers. *Nanoscale*, 11(1):45–49, 2019.

[46] Shuming Nie and Steven R Emory. Probing single molecules and single nanoparticles by surface-enhanced raman scattering. *science*, 275(5303):1102–1106, 1997.

[47] Braulio García-Cámara, Francisco González, and Fernando Moreno. Linear polarization degree for detecting magnetic properties of small particles. *Optics letters*, 35(23):4084–4086, 2010.

[48] Raquel Gomez-Medina, Braulio Garcia-Camara, Irene Suárez-Lacalle, Francisco González, Fernando Moreno, Manuel Nieto-Vesperinas, and Juan José Sáenz. Electric and magnetic dipolar response of germanium nanospheres: interference effects, scattering anisotropy, and optical forces. *Journal of Nanophotonics*, 5(1):053512, 2011.

[49] Craig F Bohren and Donald R Huffman. *Absorption and scattering of light by small particles*. John Wiley & Sons, 2008.

[50] Barbara J Messinger, K Ulrich Von Raben, Richard K Chang, and Peter W Barber. Local fields at the surface of noble-metal microspheres. *Physical Review B*, 24(2):649, 1981.

[51] Shinji Hayashi and Takayuki Okamoto. Plasmonics: visit the past to know the future. *Journal of Physics D: Applied Physics*, 45(43):433001, 2012.

[52] Michael Galperin and Abraham Nitzan. Current-induced light emission and light-induced current in molecular-tunneling junctions. *Physical review letters*, 95(20):206802, 2005.

[53] Michael Galperin and Abraham Nitzan. Optical properties of current carrying molecular wires. *The Journal of chemical physics*, 124(23):234709, 2006.

[54] John R Lombardi and Ronald L Birke. Theory of surface-enhanced raman scattering in semiconductors. *The Journal of Physical Chemistry C*, 118(20):11120–11130, 2014.

[55] Seth M Morton and Lasse Jensen. Understanding the molecule- surface chemical coupling in sers. *Journal of the American Chemical Society*, 131(11):4090–4098, 2009.

[56] Andreas C Albrecht. "forbidden"character in allowed electronic transitions. *The Journal of Chemical Physics*, 33(1):156–169, 1960.

[57] Andreas C Albrecht. Vibronic calculations in benzene. *The Journal of Chemical Physics*, 33(1):169–178, 1960.

[58] Andreas C. Albrecht. On the theory of raman intensities. *The Journal of Chemical Physics*, 34(5):1476–1484, 1961.

[59] DV Murphy and SRJ Brueck. Enhanced raman scattering from silicon microstructures. *Optics letters*, 8(9):494–496, 1983.

[60] Saleem H Zaidi, An-Shyang Chu, and SRJ Brueck. Optical properties of nanoscale, one-dimensional silicon grating structures. *Journal of applied physics*, 80(12):6997–7008, 1996.

[61] FM Liu, B Ren, JH Wu, JW Yan, XF Xue, BW Mao, and ZQ Tian. Enhanced-raman scattering from silicon nanoparticle substrates. *Chemical physics letters*, 382(5-6):502–507, 2003.

[62] Linyou Cao, Bahram Nabet, and Jonathan E Spanier. Enhanced raman scattering from individual semiconductor nanocones and nanowires. *Physical review letters*, 96(15):157402, 2006.

[63] M Khorasaninejad, J Walia, and SS Saini. Enhanced first-order raman scattering from arrays of vertical silicon nanowires. *Nanotechnology*, 23(27):275706, 2012.

[64] M Khorasaninejad, N Dhindsa, J Walia, S Patchett, and SS Saini. Highly enhanced raman scattering from coupled vertical silicon nanowire arrays. *Applied Physics Letters*, 101(17):173114, 2012.

[65] Sabrina M Wells, Igor A Merkulov, Ivan I Kravchenko, Nickolay V Lavrik, and Michael J Sepaniak. Silicon nanopillars for field-enhanced surface spectroscopy. *ACS nano*, 6(4):2948–2959, 2012.

[66] Xiaotian Wang, Wensheng Shi, Guangwei She, and Lixuan Mu. Using si and ge nanostructures as substrates for surface-enhanced raman scattering based on photoinduced charge transfer mechanism. *Journal of the American Chemical Society*, 133(41):16518–16523, 2011.

[67] I Rodriguez, Lei Shi, Xiaotang Lu, BA Korgel, RA Alvarez-Puebla, and F Meseguer. Silicon nanoparticles as raman scattering enhancers. *Nanoscale*, 6(11):5666–5670, 2014.

[68] Robert H Perry, Don W Green, and JO Maloney. Perry's chemical engineers' handbook (ed.). *Seventh, International edition*, 1997.

[69] Libin Yang, Xin Jiang, Weidong Ruan, Bing Zhao, Weiqing Xu, and John R Lombardi. Observation of enhanced raman scattering for molecules adsorbed on tio2 nanoparticles: charge-transfer contribution. *The Journal of Physical Chemistry C*, 112(50):20095–20098, 2008.

[70] Libin Yang, Xiaoyu Qin, Xin Jiang, Mengdi Gong, Di Yin, Yingjiu Zhang, and Bing Zhao. Sers investigation of ciprofloxacin drug molecules on tio 2 nanoparticles. *Physical Chemistry Chemical Physics*, 17(27):17809–17815, 2015.

[71] Anthony Musumeci, David Gosztola, Tara Schiller, Nada M Dimitrijevic, Vladimiro Mujica, Darren Martin, and Tijana Rajh. Sers of semiconducting nanoparticles (tio2 hybrid composites). *Journal of the American Chemical Society*, 131(17):6040–6041, 2009.

[72] Daniel Finkelstein-Shapiro, Pilarisetty Tarakeshwar, Tijana Rajh, and Vladimiro Mujica. Photoinduced kinetics of sers in bioinorganic hybrid systems. a case study: Dopamine- tio2. *The Journal of Physical Chemistry B*, 114(45):14642–14645, 2010.

[73] Pilarisetty Tarakeshwar, Daniel Finkelstein-Shapiro, Tijana Rajh, and Vladimiro Mujica. Quantum confinement effects on the surface enhanced raman spectra of hybrid systems molecule-tio2 nanoparticles. *International Journal of Quantum Chemistry*, 111(7-8):1659–1670, 2011.

[74] Danilo Bersani, PP Lottici, and Xing-Zhao Ding. Phonon confinement effects in the raman scattering by tio 2 nanocrystals. *Applied Physics Letters*, 72(1):73–75, 1998.

[75] Xiangxin Xue, Wei Ji, Zhu Mao, Huijuan Mao, Yue Wang, Xu Wang, Weidong Ruan, Bing Zhao, and John R Lombardi. Raman investigation of nanosized tio2: effect of crystallite size and quantum confinement. *The Journal of Physical Chemistry C*, 116(15):8792–8797, 2012.

[76] Dmitry Maznichenko, Krishnan Venkatakrishnan, and Bo Tan. Stimulating multiple sers mechanisms by a nanofibrous three-dimensional network structure of titanium dioxide (tio2). *The Journal of Physical Chemistry C*, 117(1):578–583, 2013.

[77] Xiao Xia Han, Christopher Köhler, Jacek Kozuch, Uwe Kuhlmann, Lars Paasche, Arumugam Sivanesan, Inez M Weidinger, and Peter Hildebrandt. Potential-dependent surface-enhanced resonance raman spectroscopy at nanostructured tio2: A case study on cytochrome b5. *Small*, 9(24):4175–4181, 2013.

[78] Ivano Alessandri, Elisa Biavardi, Alessandra Gianoncelli, Paolo Bergese, and Enrico Dalcanale. Cavitands endow all-dielectric beads with selectivity for plasmon-free enhanced raman detection of n ε-methylated lysine. *ACS Applied Materials & Interfaces*, 8(24):14944–14951, 2016.

[79] Ivano Alessandri and LE Depero. All-oxide raman-active traps for light and matter: probing redox homeostasis model reactions in aqueous environment. *Small*, 10(7):1294–1298, 2014.

[80] Dianyu Qi, Liujia Lu, Lingzhi Wang, and Jinlong Zhang. Improved sers sensitivity on plasmon-free tio2 photonic microarray by enhancing light-matter coupling. *Journal of the American Chemical Society*, 136(28):9886–9889, 2014.

[81] Ivano Alessandri, Marcello Zucca, Matteo Ferroni, Elza Bontempi, and Laura E Depero. Tailoring the pore size and architecture of ceo2/tio2 core/shell inverse opals by atomic layer deposition. *Small*, 5(3):336–340, 2009.

[82] Yanfei Wang, Weidong Ruan, Junhu Zhang, Bai Yang, Weiqing Xu, Bing Zhao, and John R Lombardi. Direct observation of surface-enhanced raman scattering in zno nanocrystals. *Journal of Raman Spectroscopy: An International Journal for Original Work in all Aspects of Raman Spectroscopy, Including Higher Order Processes, and also Brillouin and Rayleigh Scattering*, 40(8):1072–1077, 2009.

[83] Kwan Kim, Kyung Lock Kim, and Kuan Soo Shin. Raman spectral characteristics of 4-aminobenzenethiol adsorbed on zno nanorod arrays. *Physical Chemistry Chemical Physics*, 15(23):9288–9294, 2013.

[84] Szetsen Lee, Jr-Wei Peng, and Chih-Sheng Liu. Photoluminescence and sers investigation of plasma treated zno nanorods. *Applied surface science*, 285:748–754, 2013.

[85] Qian Liu, Li Jiang, and Lin Guo. Precursor-directed self-assembly of porous zno nanosheets as high-performance surface-enhanced raman scattering substrate. *Small*, 10(1):48–51, 2014.

[86] Hae-Young Shin, Ee-Le Shim, Young-Jin Choi, Jong-Hyurk Park, and Seokhyun Yoon. Giant enhancement of the raman response due to one-dimensional zno nanostructures. *Nanoscale*, 6(24):14622–14626, 2014.

[87] Kenan Zhang, Yun Zhang, Tianning Zhang, Wenjing Dong, Tiaoxing Wei, Yan Sun, Xin Chen, Guozhen Shen, and Ning Dai. Vertically coupled zno nanorods on mos2 monolayers with enhanced raman and photoluminescence emission. *Nano Research*, 8(3):743–750, 2015.

[88] A Kudelski, W Grochala, M Janik-Czachor, J Bukowska, A Szummer, and M Dolata. Surface-enhanced raman scattering (sers) at copper (i) oxide. *Journal of Raman spectroscopy*, 29(5):431–435, 1998.

[89] Yanfei Wang, Hailong Hu, Shengyu Jing, Yunxin Wang, Zhihua Sun, Bing Zhao, Chun Zhao, and John R Lombardi. Enhanced raman scattering as a probe for 4-mercaptopyridine surface-modified copper oxide nanocrystals. *Analytical sciences*, 23(7):787–791, 2007.

[90] Chao Qiu, Li Zhang, Hui Wang, and Chaoyang Jiang. Surface-enhanced raman scattering on hierarchical porous cuprous oxide nanostructures in nanoshell and thin-film geometries. *The journal of physical chemistry letters*, 3(5):651–657, 2012.

[91] Ruey-Chi Wang and Hsin-Ying Lin. Efficient surface enhanced raman scattering from cu2o porous nanowires transformed from cuo nanowires by plasma treatments. *Materials Chemistry and Physics*, 136(2-3):661–665, 2012.

[92] Li Jiang, Tingting You, Penggang Yin, Yang Shang, Dongfeng Zhang, Lin Guo, and Shihe Yang. Surface-enhanced raman scattering spectra of adsorbates on cu 2 o nanospheres: charge-transfer and electromagnetic enhancement. *Nanoscale*, 5(7):2784–2789, 2013.

[93] Zhijie Shi, Tao Wang, Haiyang Lin, Xiuhua Wang, Juanjuan Ding, and Mingwang Shao. Excellent surface-enhanced raman scattering (sers) based on agfeo 2 semiconductor nanoparticles. *Nanoscale*, 5(20):10029–10033, 2013.

[94] Ping Zhang, Yinsheng Wang, Tianjing He, Baozhong Zhang, Xiuyan Wang, Houwen Xin, and Fan-chen Liu. Sers of pyridine, 1, 4-dioxane and 1-ethyl-3-methyl-2-thiacyanine iodide adsorbed on α-fe2o3 colloids. *Chemical physics letters*, 153(2-3):215–222, 1988.

[95] Xiaoqi Fu, Fengli Bei, Xin Wang, Xujie Yang, and Lude Lu. Two-dimensional monolayers of single-crystalline α-fe2o3 nanospheres: preparation, characterization and sers effect. *Materials Letters*, 63(2):185–187, 2009.

[96] Namhey Lee, P James Schuck, Peter S Nico, and Benjamin Gilbert. Surface enhanced raman spectroscopy of organic molecules on magnetite (fe3o4) nanoparticles. *The journal of physical chemistry letters*, 6(6):970–974, 2015.

[97] Li Jiang, Penggang Yin, Tingting You, Hua Wang, Xiufeng Lang, Lin Guo, and Shihe Yang. Highly reproducible surface-enhanced raman spectra on semiconductor sno2 octahedral nanoparticles. *ChemPhysChem*, 13(17):3932–3936, 2012.

[98] J Pan, M Li, YY Luo, H Wu, L Zhong, Q Wang, and GH Li. Synthesis and sers activity of v2o5 nanoparticles. *Applied Surface Science*, 333:34–38, 2015.

[99] Kanishka Biswas, SV Bhat, and CNR Rao. Surface-enhanced raman spectra of azaaromatics on nanocrystals of metallic reo3. *The Journal of Physical Chemistry C*, 111(15):5689–5693, 2007.

[100] Shan Cong, Yinyin Yuan, Zhigang Chen, Junyu Hou, Mei Yang, Yanli Su, Yongyi Zhang, Liang Li, Qingwen Li, Fengxia Geng, et al. Noble metal-comparable sers enhancement from semiconducting metal oxides by making oxygen vacancies. *Nature communications*, 6(1):1–7, 2015.

[101] Mark S Anderson. Nonplasmonic surface enhanced raman spectroscopy using silica microspheres. *Applied Physics Letters*, 97(13):131116, 2010.

[102] VR Dantham, PB Bisht, and CKR Namboodiri. Enhancement of raman scattering by two orders of magnitude using photonic nanojet of a microsphere. *Journal of Applied Physics*, 109(10):103103, 2011.

[103] Davide Carboni, Barbara Lasio, Danilo Loche, Maria F Casula, Alberto Mariani, Luca Malfatti, and Plinio Innocenzi. Introducing ti-gers: Raman scattering enhancement in graphene-mesoporous titania films. *The Journal of Physical Chemistry Letters*, 6(16):3149–3154, 2015.

[104] Lili Zhang, Zhiwei Bao, Xinxin Yu, Peng Dai, Jin Zhu, Mingzai Wu, Guang Li, Xiansong Liu, Zhaoqi Sun, and Changle Chen. Rational design of α-fe2o3/reduced graphene oxide composites: rapid detection and effective removal of organic pollutants. *ACS Applied Materials & Interfaces*, 8(10):6431–6438, 2016.

[105] Bocheng Qiu, Mingyang Xing, Qiuying Yi, and Jinlong Zhang. Chiral carbonaceous nanotubes modified with titania nanocrystals: Plasmon-free and recyclable sers sensitivity. *Angewandte Chemie International Edition*, 54(36):10643–10647, 2015.

[106] Gururaj V Naik, Vladimir M Shalaev, and Alexandra Boltasseva. Alternative plasmonic materials: beyond gold and silver. *Advanced Materials*, 25(24):3264–3294, 2013.

[107] Junhong Zhao, Jian Lin, Hengyong Wei, Xiuhua Li, Wenjun Zhang, Guannan Zhao, Jinglong Bu, and Ying Chen. Surface enhanced raman scattering substrates based on titanium nitride nanorods. *Optical Materials*, 47:219–224, 2015.

[108] Xiaoqi Fu, Yi Pan, Xin Wang, and John R Lombardi. Quantum confinement effects on charge-transfer between pbs quantum dots and 4-mercaptopyridine. *The Journal of chemical physics*, 134(2):024707, 2011.

[109] Syed K Islam, Mohammad A Sohel, and John R Lombardi. Coupled exciton and charge-transfer resonances in the raman enhancement of phonon modes of cdse quantum dots (qds). *The Journal of Physical Chemistry C*, 118(33):19415–19421, 2014.

[110] Jian-An Huang, Ying-Qi Zhao, Xue-Jin Zhang, Lin-Bao Luo, Yan-Kuan Liu, Juan Antonio Zapien, Charles Surya, and Shuit-Tong Lee. Enhanced raman scattering from vertical silicon nanowires array. *Applied Physics Letters*, 98(18):183108, 2011.

[111] Pavel A Dmitriev, Denis G Baranov, Valentin A Milichko, Sergey V Makarov, Ivan S Mukhin, Anton K Samusev, Alexander E Krasnok, Pavel A Belov, and Yuri S Kivshar. Resonant raman scattering from silicon nanoparticles enhanced by magnetic response. *Nanoscale*, 8(18):9721–9726, 2016.

[112] Nicolò Bontempi, Marco Salmistraro, Matteo Ferroni, Laura E Depero, and Ivano Alessandri. Probing the spatial extension of light trapping-induced enhanced raman scattering in high-density si nanowire arrays. *Nanotechnology*, 25(46):465705, 2014.

[113] Ji-Xin Cheng and Xiaoliang Sunney Xie. *Coherent Raman scattering microscopy*. CRC press, 2016.

[114] HJ Simon, DE Mitchell, and JG Watson. Optical second-harmonic generation with surface plasmons in silver films. *Physical Review Letters*, 33(26):1531, 1974.

[115] CK Chen, A Re B de Castro, and YR Shen. Surface-enhanced second-harmonic generation. *Physical Review Letters*, 46(2):145, 1981.

[116] Markus Lippitz, Meindert A van Dijk, and Michel Orrit. Third-harmonic generation from single gold nanoparticles. *Nano letters*, 5(4):799–802, 2005.

[117] Martin Mesch, Bernd Metzger, Mario Hentschel, and Harald Giessen. Nonlinear plasmonic sensing. *Nano letters*, 16(5):3155–3159, 2016.

[118] M. R. Beversluis, A. Bouhelier, and L. Novotny. Continuum generation from single gold nanostructures through near-field mediated intraband transitions. *Physical Review B*, 68(11):115433, 2003.

[119] Alexandre Bouhelier, Michael R Beversluis, and Lukas Novotny. Characterization of nanoplasmonic structures by locally excited photoluminescence. *Applied physics letters*, 83(24):5041–5043, 2003.

[120] Stefano Palomba, Hayk Harutyunyan, Jan Renger, Romain Quidant, Niek F van Hulst, and Lukas Novotny. Nonlinear plasmonics at planar metal surfaces. *Philosophical Transactions of the Royal Society A: Mathematical, Physical and Engineering Sciences*, 369(1950):3497–3509, 2011.

[121] Steven Yampolsky, Dmitry A Fishman, Shirshendu Dey, Eero Hulkko, Mayukh Banik, Eric O Potma, and Vartkess A Apkarian. Seeing a single molecule vibrate through time-resolved coherent anti-stokes raman scattering. *Nature Photonics*, 8(8):650, 2014.

[122] Alan Campion and Patanjali Kambhampati. Surface-enhanced raman scattering. *Chemical society reviews*, 27(4):241–250, 1998.

[123] CK Chen, ARB De Castro, YR Shen, and F DeMartini. Surface coherent anti-stokes raman spectroscopy. *Physical Review Letters*, 43(13):946, 1979.

[124] Andreas Zumbusch, Gary R. Holtom, and X. Sunney Xie. Three-dimensional vibrational imaging by coherent anti-stokes raman scattering. *Physical Review Letters*, 82(20):4142–4145, 1999.

[125] Ji-Xin Cheng, Lewis D Book, and X Sunney Xie. Polarization coherent anti-stokes raman scattering microscopy. *Optics letters*, 26(17):1341–1343, 2001.

[126] Conor L Evans, Eric O Potma, and X Sunney Xie. Coherent anti-stokes raman scattering spectral interferometry: determination of the real and imaginary components of nonlinear susceptibility χ (3) for vibrational microscopy. *Optics letters*, 29(24):2923–2925, 2004.

[127] Eric O Potma, Conor L Evans, and X Sunney Xie. Heterodyne coherent anti-stokes raman scattering (cars) imaging. *Optics letters*, 31(2):241–243, 2006.

[128] Xia Hua, Dmitri V Voronine, Charles W Ballmann, Alexander M Sinyukov, Alexei V Sokolov, and Marlan O Scully. Nature of surface-enhanced coherent raman scattering. *Physical Review A*, 89(4):043841, 2014.

[129] V Namboodiri, M Namboodiri, GI Cava Diaz, M Oppermann, G Flachenecker, and A Materny. Surface-enhanced femtosecond cars spectroscopy (se-cars) on pyridine. *Vibrational Spectroscopy*, 56(1):9–12, 2011.

[130] Christian Steuwe, Clemens F Kaminski, Jeremy J Baumberg, and Sumeet Mahajan. Surface enhanced coherent anti-stokes raman scattering on nanostructured gold surfaces. *Nano letters*, 11(12):5339–5343, 2011.

[131] Yu Zhang, Yu-Rong Zhen, Oara Neumann, Jared K Day, Peter Nordlander, and Naomi J Halas. Coherent anti-stokes raman scattering with single-molecule sensitivity using a plasmonic fano resonance. *Nature communications*, 5:4424, 2014.

[132] Cheng Zong, Ran Cheng, Fukai Chen, Peng Lin, Meng Zhang, Zhicong Chen, Chuan Li, Chen Yang, and Ji-Xin Cheng. Wide-field surface-enhanced coherent anti-stokes raman scattering microscopy. *ACS Photonics*, 9(3):1042–1049, 2022.

[133] Xiaoguang Li, Di Xiao, and Zhenyu Zhang. Landau damping of quantum plasmons in metal nanostructures. *New Journal of Physics*, 15(2):023011, 2013.

[134] Mark L Brongersma, Naomi J Halas, and Peter Nordlander. Plasmon-induced hot carrier science and technology. *Nature nanotechnology*, 10(1):25–34, 2015.

[135] S Dey, M Banik, E Hulkko, K Rodriguez, VA Apkarian, M Galperin, and A Nitzan. Observation and analysis of fano-like lineshapes in the raman spectra of molecules adsorbed at metal interfaces. *Physical Review B*, 93(3):035411, 2016.

[136] HE Elsayed-Ali, T Juhasz, GO Smith, and WE Bron. Femtosecond thermoreflectivity and thermotransmissivity of polycrystalline and single-crystalline gold films. *Physical Review B*, 43(5):4488, 1991.

[137] C-K Sun, F Vallée, L Acioli, EP Ippen, and JG Fujimoto. Femtosecond investigation of electron thermalization in gold. *Physical Review B*, 48(16):12365, 1993.

[138] Emily L Keller, Nathaniel C Brandt, Alyssa A Cassabaum, and Renee R Frontiera. Ultrafast surface-enhanced raman spectroscopy. *Analyst*, 140(15):4922–4931, 2015.

[139] Emily L Keller, Hyunho Kang, Christy L Haynes, and Renee R Frontiera. Effect of silica supports on plasmonic heating of molecular adsorbates as measured by ultrafast surface-enhanced raman thermometry. *ACS applied materials & interfaces*, 10(47):40577–40584, 2018.

[140] LV Keldysh et al. Ionization in the field of a strong electromagnetic wave. *Sov. Phys. JETP*, 20(5):1307–1314, 1965.

[141] Kevin T Crampton, Aram Zeytunyan, Alexander S Fast, Faezeh T Ladani, Alba Alfonso-Garcia, Mayukh Banik, Steven Yampolsky, Dmitry A Fishman, Eric O Potma, and V Ara Apkarian. Ultrafast coherent raman scattering at plasmonic nanojunctions. *The Journal of Physical Chemistry C*, 120(37):20943–20953, 2016.

[142] Bernard Valeur and Berberan-Santos Mario N. *Molecular Fluorescence: Principles and Applications*. Wiley-VCH, 2012.

[143] C.D. Geddes and J.R. Lakowicz. *Advanced Concepts in Fluorescence Sensing: Part A: Small Molecule Sensing*. Topics in Fluorescence Spectroscopy. Springer US, 2007.

[144] Richard B Thompson. *Fluorescence Sensors and Biosensors*. CRC Press, 2019.

[145] Joseph R. Lakowicz. *Principles of Fluorescence Spectroscopy*. Springer‘, 2010.

[146] Thorsten Liebermann and Wolfgang Knoll. Surface-plasmon field-enhanced fluorescence spectroscopy. *Colloids and Surfaces A: Physicochemical and Engineering Aspects*, 171(1-3):115–130, Oct 2000.

[147] K. Schmitt, B. Schirmer, C. Hoffmann, A. Brandenburg, and P. Meyrueis. Interferometric biosensor based on planar optical waveguide sensor chips for label-free detection of surface bound bioreactions. *Biosensors Bioelectronics*, 22(11):2591–2597, 2007.

[148] R. G. Heideman and P. V. Lambeck. Remote opto-chemical sensing with extreme sensitivity: design, fabrication and performance of a pigtailed integrated optical phase-modulated mach-zehnder interferometer system. *Sensors and Actuators B-Chemical*, 61(1-3):100–127, 1999.

[149] P. Kukura, H. Ewers, C. Muller, A. Renn, A. Helenius, and V. Sandoghdar. High-speed nanoscopic tracking of the position and orientation of a single virus. *Nature Methods*, 6(12):923–927, 2009.

[150] J. Ortega-Arroyo and P. Kukura. Interferometric scattering microscopy (iscat): new frontiers in ultrafast and ultrasensitive optical microscopy. *Physical Chemistry Chemical Physics*, 14(45):15625–15636, 2012.

[151] J. O. Arroyo, J. Andrecka, K. M. Spillane, N. Billington, Y. Takagi, J. R. Sellers, and P. Kukura. Label-free, all-optical detection, imaging, and tracking of a single protein. *Nano Letters*, 14(4):2065–2070, 2014.

[152] K. Matsubara, S. Kawata, and S. Minami. A compact surface-plasmon resonance sensor for measurement of water in process. *Applied Spectroscopy*, 42(8):1375–1379, 1988.

[153] J. Homola. Surface plasmon resonance sensors for detection of chemical and biological species. *Chemical Reviews*, 108(2):462–493, 2008.

[154] Yu-wen Su and Wei Wang. Surface plasmon resonance sensing: from purified biomolecules to intact cells. *Analytical and Bioanalytical Chemistry*, 410(17):3943–3951, Jul 2018.

[155] C. Boozer, G. Kim, S. Cong, H. Guan, and T. Londergan. Looking towards label-free biomolecular interaction analysis in a high-throughput format: a review of new surface plasmon resonance technologies. *Curr Opin Biotechnol*, 17(4):400–5, 2006.

[156] J. R. Mejia-Salazar and Jr. Oliveira, O. N. Plasmonic biosensing. *Chem Rev*, 118(20):10617–10625, 2018.

[157] Yingyan Jiang and Wei Wang. Point spread function of objective-based surface plasmon resonance microscopy. *Analytical Chemistry*, 90(15):9650–9656, 2018.

[158] Lauri Viitala, Adam M. Maley, H. W. Millie Fung, Robert M. Corn, Tapani Viitala, and Lasse Murtomäki. Surface plasmon resonance imaging microscopy of liposomes and liposome-encapsulated gold nanoparticles. *The Journal of Physical Chemistry C*, 120(45):25958–25966, 2016.

[159] H. Yu, X. N. Shan, S. P. Wang, and N. J. Tao. Achieving high spatial resolution surface plasmon resonance microscopy with image reconstruction. *Analytical Chemistry*, 89(5):2704–2707, 2017.

[160] J. P. Kenison, A. Fast, B. M. Matthews, R. M. Corn, and E. O. Potma. Particle sensing with confined optical field enhanced fluorescence emission (cofefe). *Optics Express*, 26(10):12959–12969, 2018.

[161] A. Mooradian. Photoluminescence of metals. *Phys. Rev. Lett.*, 22:185–187, Feb 1969.

[162] G. T. Boyd, Z. H. Yu, and Y. R. Shen. Photoinduced luminescence from the noble metals and its enhancement on roughened surfaces. *Phys. Rev. B*, 33:7923–7936, Jun 1986.

[163] S. J. Hurst, A. K. Lytton-Jean, and C. A. Mirkin. Maximizing dna loading on a range of gold nanoparticle sizes. *Anal Chem*, 78(24):8313–8, 2006.

[164] F. Hache, D. Ricard, C. Flytzanis, and U. Kreibig. The optical kerr effect in small metal particles and metal colloids: The case of gold. *Applied Physics A*, 47(4):347–357, Dec 1988.

[165] Yu Akimov and S. Sun. Spacer-controlled emission of randomly oriented fluorophores enhanced with surface plasmon-polaritons. *Phys. Chem. Chem. Phys.*, 19:8706–8714, 2017.

[166] Kohei Imura, Tetsuhiko Nagahara, and Hiromi Okamoto. Near-field two-photon-induced photoluminescence from single gold nanorods and imaging of plasmon modes. *The Journal of Physical Chemistry B*, 109(27):13214–13220, 2005.

[167] H. M. Kim, C. X. Xiang, A. G. Guell, R. M. Penner, and E. O. Potma. Tunable two-photon excited luminescence in single gold nanowires fabricated by lithographically patterned nanowire electrodeposition. *Journal of Physical Chemistry C*, 112(33):12721–12727, 2008.

[168] K. I. Mortensen, L. S. Churchman, J. A. Spudich, and H. Flyvbjerg. Optimized localization analysis for single-molecule tracking and super-resolution microscopy. *Nature Methods*, 7:377–381, 2010.

[169] Lothar Schermelleh, Rainer Heintzmann, and Heinrich Leonhardt. A guide to super-resolution fluorescence microscopy. *The Journal of Cell Biology*, 190(2):165–175, 2010.

[170] Eric Betzig, George H. Patterson, Rachid Sougrat, O. Wolf Lindwasser, Scott Olenych, Juan S. Bonifacino, Michael W. Davidson, Jennifer Lippincott-Schwartz, and Harald F. Hess. Imaging intracellular fluorescent proteins at nanometer resolution. *Science*, 313(5793):1642–1645, 2006.

[171] Samuel T. Hess, Thanu P.K. Girirajan, and Michael D. Mason. Ultra-high resolution imaging by fluorescence photoactivation localization microscopy. *Biophysical Journal*, 91(11):4258 – 4272, 2006.

[172] Michael Rust, Mark Bates, and Xiaowei Zhuang. Sub-diffraction-limit imaging by stochastic optical reconstruction microscopy (storm). *Nature Methods*, 3:793–796, 2006.

[173] N. Gustafsson, S. Culley, G. Ashdown, D. M. Owen, P. M. Pereira, and R. Henriques. Fast live-cell conventional fluorophore nanoscopy with imagej through super-resolution radial fluctuations. *Nature Communications*, 7, 2016.

[174] Daniel Podbiel, Philip Kahl, Andreas Makris, Bettina Frank, Simon Sindermann, Timothy J. Davis, Harald Giessen, Michael Horn-von Hoegen, and Frank-J. Meyer zu Heringdorf. Imaging the nonlinear plasmoemission dynamics of electrons from strong plasmonic fields. *Nano Letters*, 17(11):6569–6574, 2017.

[175] Marcel Reutzel, Andi Li, and Hrvoje Petek. Coherent two-dimensional multiphoton photoelectron spectroscopy of metal surfaces. *Phys. Rev. X*, 9:011044, Mar 2019.

[176] Richard L McCreery. *Raman spectroscopy for chemical analysis*, volume 225. John Wiley & Sons, 2005.

[177] Cheng Zong, Ranjith Premasiri, Haonan Lin, Yimin Huang, Chi Zhang, Chen Yang, Bin Ren, Lawrence D Ziegler, and Ji-Xin Cheng. Plasmon-enhanced stimulated raman scattering microscopy with single-molecule detection sensitivity. *arXiv preprint arXiv:1903.05167*, 2019.

[178] M. Fleischmann, P.J. Hendra, and A.J. McQuillan. Raman spectra of pyridine adsorbed at a silver electrode. *Chemical Physics Letters*, 26(2):163 – 166, 1974.

[179] David L. Jeanmaire and Richard P. Van Duyne. Surface raman spectroelectrochemistry: Part i. heterocyclic, aromatic, and aliphatic amines adsorbed on the anodized silver electrode. *Journal of Electroanalytical Chemistry and Interfacial Electrochemistry*, 84(1):1 – 20, 1977.

[180] Martin Moskovits. Surface-enhanced spectroscopy. *Rev. Mod. Phys.*, 57:783–826, 1985.

[181] Katherine A Willets and Richard P Van Duyne. Localized surface plasmon resonance spectroscopy and sensing. *Annu. Rev. Phys. Chem.*, 58:267–297, 2007.

[182] Renhe Zhang, Yao Zhang, ZC Dong, S Jiang, C Zhang, LG Chen, L Zhang, Y Liao, J Aizpurua, Y ea Luo, et al. Chemical mapping of a single molecule by plasmon-enhanced raman scattering. *Nature*, 498(7452):82–86, 2013.

[183] Eric C Le Ru and Pablo G Etchegoin. Single-molecule surface-enhanced raman spectroscopy. *Annual review of physical chemistry*, 63:65–87, 2012.

[184] Jon A. Dieringer, Robert B. Lettan, Karl A. Scheidt, and Richard P. Van Duyne. A frequency domain existence proof of single-molecule surface-enhanced raman spectroscopy. *Journal of the American Chemical Society*, 129(51):16249–16256, 2007.

[185] Katrin Kneipp, Harald Kneipp, V. Bhaskaran Kartha, Ramasamy Manoharan, Geurt Deinum, Irving Itzkan, Ramachandra R. Dasari, and Michael S. Feld. Detection and identification of a single dna base molecule using surface-enhanced raman scattering (sers). *Phys. Rev. E*, 57:R6281–R6284, Jun 1998.

[186] PD Maker and RW Terhune. Study of optical effects due to an induced polarization third order in the electric field strength. *Physical Review*, 137(3A):A801, 1965.

[187] Conor L Evans and X Sunney Xie. Coherent anti-stokes raman scattering microscopy: chemical imaging for biology and medicine. *Annu. Rev. Anal. Chem.*, 1:883–909, 2008.

[188] Ji-Xin Cheng and XS Xie. Coherent anti-stokes raman scattering microscopy: instrumentation, theory, and application. *J. Phys. Chem. B*, 108:827–840, 2004.

[189] Meng Cui, Brandon R Bachler, and Jennifer P Ogilvie. Comparing coherent and spontaneous raman scattering under biological imaging conditions. *Optics letters*, 34(6):773–775, 2009.

[190] Andreas Zumbusch, Gary R Holtom, and X Sunney Xie. Three-dimensional vibrational imaging by coherent anti-stokes raman scattering. *Physical review letters*, 82(20):4142, 1999.

[191] T. Ideguchi, S. Holzner, B. Bernhardt, G. Guelachvili, N. Picqué, and T. W. Hänsch. Coherent raman spectro-imaging with laser frequency combs. *Nature*, 502:355–358, 2013.

[192] Risako Kameyama, Shigekazu Takizawa, Kotaro Hiramatsu, and Keisuke Goda. Dual-comb coherent raman spectroscopy with near 100% duty cycle. *ACS Photonics*, 8(4):975–981, 2021.

[193] Chi Zhang, Kai-Chih Huang, Bartek Rajwa, Junjie Li, Shiqi Yang, Haonan Lin, Chien sheng Liao, Gregory Eakins, Shihuan Kuang, Valery Patsekin, J. Paul Robinson, and Ji-Xin Cheng. Stimulated raman scattering flow cytometry for label-free single-particle analysis. *Optica*, 4(1):103–109, Jan 2017.

[194] C. K. Chen, A. R. B. de Castro, Y. R. Shen, and F. DeMartini. Surface coherent anti-stokes raman spectroscopy. *Phys. Rev. Lett.*, 43:946–949, Sep 1979.

[195] Tae-Woong Koo, Selena Chan, and Andrew A Berlin. Single-molecule detection of biomolecules by surface-enhanced coherent anti-stokes raman scattering. *Optics letters*, 30(9):1024–1026, 2005.

[196] Rogier HM Groeneveld, Rudolf Sprik, and Ad Lagendijk. Femtosecond spectroscopy of electron-electron and electron-phonon energy relaxation in ag and au. *Physical Review B*, 51(17):11433, 1995.

[197] Alexandre Bouhelier, Renaud Bachelot, Gilles Lerondel, Sergei Kostcheev, Pascal Royer, and GP Wiederrecht. Surface plasmon characteristics of tunable photoluminescence in single gold nanorods. *Physical review letters*, 95(26):267405, 2005.

[198] Alessandro Alabastri, Andrea Toma, Mario Malerba, Francesco De Angelis, and Remo Proietti Zaccaria. High temperature nanoplasmonics: the key role of nonlinear effects. *ACS Photonics*, 2(1):115–120, 2015.

[199] Gaëtan Lévêque and Olivier JF Martin. Optical interactions in a plasmonic particle coupled to a metallic film. *Optics express*, 14(21):9971–9981, 2006.

[200] P Nordlander and F Le. Plasmonic structure and electromagnetic field enhancements in the metallic nanoparticle-film system. *Applied Physics B*, 84(1):35–41, 2006.

[201] Felix Benz, Rohit Chikkaraddy, Andrew Salmon, Hamid Ohadi, Bart De Nijs, Jan Mertens, Cloudy Carnegie, Richard W Bowman, and Jeremy J Baumberg. Sers of individual nanoparticles on a mirror: size does matter, but so does shape. *The journal of physical chemistry letters*, 7(12):2264–2269, 2016.

[202] Nicolò Bontempi, Irene Vassalini, Stefano Danesi, Matteo Ferroni, Maurizio Donarelli, Paolo Colombi, and Ivano Alessandri. Non-plasmonic sers with silicon: is it really safe? new insights into the optothermal properties of core/shell microbeads. *The journal of physical chemistry letters*, 9(9):2127–2132, 2018.

[203] Jeremy J Baumberg, Javier Aizpurua, Maiken H Mikkelsen, and David R Smith. Extreme nanophotonics from ultrathin metallic gaps. *Nature materials*, 18(7):668–678, 2019.

[204] D Palik Edward and IJHOOCOS Palik. Handbook of optical constants of solids, 1985.

[205] Shamsul Abedin, John Kenison, Christian Vargas, and Eric Olaf Potma. Sensing biomolecular interactions by the luminescence of a planar gold film. *Analytical Chemistry*, 91(24):15883–15889, 2019.

[206] John Y Gui, Donald A Stern, Douglas G Frank, Frank Lu, Donald C Zapien, and Arthur T Hubbard. Adsorption and surface structural chemistry of thiophenol, benzyl mercaptan, and alkyl mercaptans. comparative studies at silver (111) and platinum (111) electrodes by means of auger spectroscopy, electron energy loss spectroscopy, low energy electron diffraction and electrochemistry. *Langmuir*, 7(5):955–963, 1991.

[207] Adam D McFarland, Matthew A Young, Jon A Dieringer, and Richard P Van Duyne. Wavelength-scanned surface-enhanced raman excitation spectroscopy. *The Journal of Physical Chemistry B*, 109(22):11279–11285, 2005.

[208] Li-Jun Wan, Mimi Terashima, Hiroyuki Noda, and Masatoshi Osawa. Molecular orientation and ordered structure of benzenethiol adsorbed on gold (111). *The Journal of Physical Chemistry B*, 104(15):3563–3569, 2000.

[209] Martin Fleischmann, Patrick J Hendra, and A James McQuillan. Raman spectra of pyridine adsorbed at a silver electrode. *Chemical physics letters*, 26(2):163–166, 1974.

[210] Pardeep Kumar, Hikaru Kuramochi, Satoshi Takeuchi, and Tahei Tahara. Time-domain observation of surface-enhanced coherent raman scattering with 105–106 enhancement. *The Journal of Physical Chemistry Letters*, 11(15):6305–6311, 2020.

[211] Viktor I Fabelinsky, Dimitrii N Kozlov, Sergey N Orlov, Yury N Polivanov, Ivan A Shcherbakov, Valery V Smirnov, Konstantin A Vereschagin, Grigory M Arzumanyan, Kahramon Z Mamatkulov, Konstantin N Afanasiev, et al. Surface-enhanced micro-cars mapping of a nanostructured cerium dioxide/aluminum film surface with gold nanoparticle-bound organic molecules. *Journal of Raman Spectroscopy*, 49(7):1145–1154, 2018.

[212] Norihiko Hayazawa, Taro Ichimura, Mamoru Hashimoto, Yasushi Inouye, and Satoshi Kawata. Amplification of coherent anti-stokes raman scattering by a metallic nanostructure for a high resolution vibration microscopy. *Journal of applied physics*, 95(5):2676–2681, 2004.

[213] Taro Ichimura, Norihiko Hayazawa, Mamoru Hashimoto, Yasushi Inouye, and Satoshi Kawata. Tip-enhanced coherent anti-stokes raman scattering for vibrational nanoimaging. *Physical review letters*, 92(22):220801, 2004.

[214] E.J. Liang, A. Weippert, J.-M. Funk, A. Materny, and W. Kiefer. Experimental observation of surface-enhanced coherent anti-stokes raman scattering. *Chemical Physics Letters*, 227(1):115 – 120, 1994.

[215] D. V. Voronine, A. M. Sinyokov, X. Hua, K. Wang, P. K. Jha, E. Munusamy, S. E. Wheeler, G. Welch, A. Sokolov, and M. O. Scully. Time-resolved surface-enhanced coherent sensing of nanoscale molecular complexes. *Sci. Rep.*, 2:891, Nov 2012.

[216] Christopher J Addison, Stanislav O Konorov, Alexandre G Brolo, Michael W Blades, and Robin FB Turner. Tuning gold nanoparticle self-assembly for optimum coherent anti-stokes raman scattering and second harmonic generation response. *The Journal of Physical Chemistry C*, 113(9):3586–3592, 2009.

[217] Zuyin Zhang and Guofeng Song. High enhancement factor of au nano triangular prism structure for surface enhanced coherent anti-stokes raman scattering. *Journal of Semiconductors*, 38(2):022001, 2017.

[218] Cheng Zong, Yurun Xie, Meng Zhang, Yimin Huang, Chen Yang, and Ji-Xin Cheng. Plasmon-enhanced coherent anti-stokes raman scattering vs plasmon-enhanced stimulated raman scattering: Comparison of line shape and enhancement factor. *The Journal of Chemical Physics*, 154(3):034201, 2021.

[219] Renee R Frontiera, Anne-Isabelle Henry, Natalie L Gruenke, and Richard P Van Duyne. Surface-enhanced femtosecond stimulated raman spectroscopy. *The journal of physical chemistry letters*, 2(10):1199–1203, 2011.

[220] Sebastian Schlucker, Mohammad Salehi, Gero Bergner, Max Schutz, Philipp Strobel, Alexander Marx, Iver Petersen, Benjamin Dietzek, and Jurgen Popp. Immuno-surface-enhanced coherent anti-stokes raman scattering microscopy: immunohistochemistry with target-specific metallic nanoprobes and nonlinear raman microscopy. *Analytical chemistry*, 83(18):7081–7085, 2011.

[221] AI Barreda, JM Saiz, F González, F Moreno, and P Albella. Recent advances in high refractive index dielectric nanoantennas: Basics and applications. *AIP Advances*, 9(4):040701, 2019.

[222] Shamsul Abedin, Khokan Roy, Xin Jin, Hui Xia, S. R. J. Brueck, and Eric O. Potma. Surface-enhanced coherent anti-stokes raman scattering of molecules near metaldielectric nanojunctions. *Journal of Physical Chemistry C*, 2022.

[223] E. Benassi and H. Fan. Quantitative characterisation of the ring normal modes. pyridine as a study case. *Spectrochimica Acta Part A: Molecular and Biomolecular Spectroscopy*, 246:119026, 2021.